AFRL-RY-WP-TR-2013-0239

THEORY OF NEAR-FIELD SCANNING WITH A PROBE ARRAY

Kristopher T. Kim and Bradley A. Kramer

Antennas & Electromagnetics Technology Branch
Multispectral Sensing & Detection Division

John A. Schindler and Hans Steyskal

Arcon Corporation

JANUARY 2014
Final Report

Approved for public release; distribution unlimited.

See additional restrictions described on inside pages

STINFO COPY

AIR FORCE RESEARCH LABORATORY
SENSORS DIRECTORATE
WRIGHT-PATTERSON AIR FORCE BASE, OH 45433-7320
AIR FORCE MATERIEL COMMAND
UNITED STATES AIR FORCE

NOTICE AND SIGNATURE PAGE

Using Government drawings, specifications, or other data included in this document for any purpose other than Government procurement does not in any way obligate the U.S. Government. The fact that the Government formulated or supplied the drawings, specifications, or other data does not license the holder or any other person or corporation; or convey any rights or permission to manufacture, use, or sell any patented invention that may relate to them.

This report was cleared for public release by the USAF 88th Air Base Wing (88 ABW) Public Affairs Office and is available to the general public, including foreign nationals. Copies may be obtained from the Defense Technical Information Center (DTIC) (http://www.dtic.mil).

AFRL-RY-WP-TR-2013-0239 HAS BEEN REVIEWED AND IS APPROVED FOR PUBLICATION IN ACCORDANCE WITH ASSIGNED DISTRIBUTION STATEMENT.

//SIGNED//

KRISTOPHER T. KIM, Program Manager
Antenna & Electromagnetic Technology Branch
Multispectral Sensing & Detection Division

//SIGNED//

TONY C. KIM, Chief
Antenna & Electromagnetic Technology Branch
Multispectral Sensing & Detection Division

//SIGNED//

TRACY W. JOHNSTON, Division Chief
Multispectral Sensing & Detection Division
Sensors Directorate

This report is published in the interest of scientific and technical information exchange, and its publication does not constitute the Government's approval or disapproval of its ideas or findings.

*Disseminated copies will show "//signature//" stamped or typed above the signature blocks.

REPORT DOCUMENTATION PAGE

Form Approved
OMB No. 0704-0188

The public reporting burden for this collection of information is estimated to average 1 hour per response, including the time for reviewing instructions, searching existing data sources, gathering and maintaining the data needed, and completing and reviewing the collection of information. Send comments regarding this burden estimate or any other aspect of this collection of information, including suggestions for reducing this burden, to Department of Defense, Washington Headquarters Services, Directorate for Information Operations and Reports (0704-0188), 1215 Jefferson Davis Highway, Suite 1204, Arlington, VA 22202-4302. Respondents should be aware that notwithstanding any other provision of law, no person shall be subject to any penalty for failing to comply with a collection of information if it does not display a currently valid OMB control number. **PLEASE DO NOT RETURN YOUR FORM TO THE ABOVE ADDRESS**.

1. REPORT DATE *(DD-MM-YY)*	2. REPORT TYPE	3. DATES COVERED *(From - To)*
January 2014	Final	15 March 2010 – 30 September 2013

4. TITLE AND SUBTITLE
THEORY OF NEAR-FIELD SCANNING WITH A PROBE ARRAY

5a. CONTRACT NUMBER
IN-HOUSE

5b. GRANT NUMBER

5c. PROGRAM ELEMENT NUMBER
61102F

6. AUTHOR(S)
Kristopher T. Kim and Bradley A. Kramer (AFRL/RYMH)
John A. Schindler and Hans Steyskal (Arcon Corporation)

5d. PROJECT NUMBER
3002

5e. TASK NUMBER
11RY0COR

5f. WORK UNIT NUMBER
Y04N

7. PERFORMING ORGANIZATION NAME(S) AND ADDRESS(ES)

Multispectral Sensing & Detection Division, Antennas & Electromagnetics Technology Branch (AFRL/RYMH)
Sensors Directorate, Air Force Research Laboratory
Wright-Patterson Air Force Base, OH 45433-7320
Air Force Materiel Command, United States Air Force

Arcon Corporation
260 Bear Hill Road
Suite 200
Waltham, MA 02451

8. PERFORMING ORGANIZATION REPORT NUMBER
AFRL-RY-WP-TR-2013-0239

9. SPONSORING/MONITORING AGENCY NAME(S) AND ADDRESS(ES)

Air Force Research Laboratory
Sensors Directorate
Wright-Patterson Air Force Base, OH 45433-7320
Air Force Materiel Command
United States Air Force

Air Force Office of Scientific Research (AFOSR)
875 N. Randolph Street
Suite. 325, Room 3112
Arlington, VA 22203-1768

10. SPONSORING/MONITORING AGENCY ACRONYM(S)
AFRL/RYMH

11. SPONSORING/MONITORING AGENCY REPORT NUMBER(S)
AFRL-RY-WP-TR-2013-0239

12. DISTRIBUTION/AVAILABILITY STATEMENT
Approved for public release; distribution unlimited.

13. SUPPLEMENTARY NOTES
PAO Case Number: 88ABW-2013-5483, cleared 29 December 2013. Report contains color.

14. ABSTRACT

In near-field scanning, as the electrical size of a device under test increases, it becomes increasingly time-consuming to collect all the required near-field samples using a single probe. Thus, it becomes desirable to use an array of probes to collect the near-field samples simultaneously to decrease the measurement time. We consider some of the electromagnetic issues associated with performing near-field measurement using an array of probes for antenna and bistatic radar cross section (RCS) applications.

15. SUBJECT TERMS
electromagnetic near-field measurement, antenna measurement, bistatic RCS measurement

16. SECURITY CLASSIFICATION OF:			17. LIMITATION OF ABSTRACT:	18. NUMBER OF PAGES	19a. NAME OF RESPONSIBLE PERSON (Monitor)
a. REPORT	b. ABSTRACT	c. THIS PAGE			Kristopher T. Kim
Unclassified	Unclassified	Unclassified	SAR	84	19b. TELEPHONE NUMBER *(Include Area Code)* N/A

Table of Contents

Section **Page**

List of Figures ii
List of Tables…… iv
1.0 Introduction..... 1
2.0 Suppression of Multiple Scattering between a DUT and a Probe Array. 6
2.1 Introduction……... 6
2.2 Antenna Scattering Matrix.……...6
2.3 Effects of Loading on a Dipole Probe…… 8
2.4 Multiple Scattering Formulation……..…..…….....9
2.5 Multiple Scattering Reduction.…….. 12
2.6 Summary…….…….....14
3.0 Performance of Modulated Scatterer Array ……..……..... 17
3.1 Introduction ……...……17
3.2 Modulated Probe Array Model……. 19
3.3 Modulated Scatterer Performance……..……...…… 26
3.3.1 Single Probe Performance……..26
3.3.2 Probe Array Performance…….. 31
3.4 Summary and Conclusions…… 45
4.0 Preliminary Investigation of Using a Circular Arc Array for Bistatic Near-Field RCS Measurement…….47
4.1 Introduction……47
4.2 Basic Assumptions for the Model……. 47
4.3 Generating the Plane Wave Illumination……..……..... 47
4.4 Measuring the Scattered Near Field ……..……50
4.5 An Example: Circular Probe Array and Cylinder Target…….. 54
4.5.1 Array Pattern Synthesis for Plane Wave Target Illumination……... 54
4.5.2 Array Excitation Perturbations due to Mutual Coupling…….. 59
4.5.3 The Array in Receive Mode…….. 59
4.6 Conclusion……..…….. 62
4.7 Appendix A: Mutual Coupling Compensation in Antenna Arrays…….. 63
4.8 Appendix B: The Mutual Impedance Z^{a}_{nm} for Two Side-by-Side Dipoles …… 65
4.9 Appendix C: The Mutual Impedance Z^{t}_{nm} due to Reflection in a Circular Cylinder…… 65
4.10 Appendix D: GO Reflection in a Circular Cylinder……. 67
4.11 Appendix E: Analysis of a Tentative Bistatic Near-Field RCS Measurement Geometry…. 69
5.0 References……..75
List of Acronyms, Abbreviations, and Symbols……77

Approved for public release; distribution unlimited.

List of Figures

Figure **Page**

1. NF-Sample Acquisition Using a Spherical Multi-Probe Scanner for Antenna Measurement.... 2
2. NF-Sample Acquisition Using a Cylindrical Multi-Probe Scanner for Bistatic RCS Measurement..... 2
3. NF Sample Acquisition Time vs. Antenna/Target Size Target 3
4. Maximum RMS Error in Plane Wave Illumination over a 20λ Target Zone for Various Array Geometries 7
5. Comparison of the FF Scattering Patterns from an Impedance-Loaded Dipole Probe with a Broadside Illumination..... 9
6. Comparison of the FF Scattering Patterns from Three Loaded Dipoles Probes..... 12
7. Three Loaded Dipoles with h=0.0475 λ, d=0.5 λ, a=0.001 13
8. Planar Scanning of a 1 λ Radius PEC Sphere..... 15
9. Comparison of the FF with the Mie Solution: the Probes are Assumed to be Shorted 16
10. Comparison of the FF with the Mie Solution: the Probes are Assumed to be Loaded..... 16
11. Signal Flow Graph Representation of the Dominant Contributions to the Measured Voltage When Probe Array Element One Is Excited and the Other Elements Are Loaded with Large Impedances 23
12. Signal Flow Graph Representation Showing Each Dominant Contribution to the Measured Voltage When Probe Array Element One Is Excited..... 24
13. Signal Flow Graph Representation of the Dominant Contributions to the Measured Voltage When Probe Array Element Two Is Excited..... 25
14. Signal Flow Graph Representation Showing Each Dominant Contribution to the Measured Voltage When Probe Array Element Two Is Excited..... 25
15. Flat Plate and Measurement Array 27
16. Single Modulated Scatterer Probe in the Presence of a Flat Plate and the Measurement Probe.28
17. Magnitude of the Relative In-Situ Measurement Voltage Transfer Function as a Function of the Load Admittance at the Modulated Scatterer Probe 29
18. Phase of the Relative In-Situ Measurement Voltage Transfer Function as a Function of the Load Admittance at the Modulated Scatterer Probe 29
19. Errors in Relative Magnitude and Phase of the Measurement Voltage Transfer Function for a Single Probe Located in Probe Array Position One..... 30
20. Errors in Relative Magnitude and Phase of the Measurement Voltage Transfer Function for a Single Probe Located in Probe Array Position Three..... 30
21. Errors in Relative Magnitude and Phase of the Measurement Voltage Transfer Function for a Single Probe Located in Probe Array Position Five 31
22. Magnitude and Phase Error of Calibration of Probe Array Element One (Nearest to Plate) with Open Circuit Loading at Other Elements 35
23. Magnitude and Phase Error of Calibration of Probe Array Element Three with Open Circuit Loading at Other Elements 36
24. Magnitude and Phase Error of Calibration of Probe Array Element Five (Farthest from Plate) with Open Circuit Loading at Other Elements 36
25. Magnitude and Phase Error of Calibration of Probe Array Element One (Nearest to Plate)

Approved for public release; distribution unlimited.

with Impedance Loading at Other Elements....38
26. Magnitude and Phase Error of Calibration of Probe Array Element Three with Impedance Loading at Other Elements....39
27. Magnitude and Phase Error of Calibration of Probe Array Element Five (Farthest from Plate) with Impedance Loading at Other Elements....40
28. Magnitude of the Calibration Error of Probe Array Element One (Nearest to Plate) with Impedance Loading at Other Elements....42
29. Magnitude of the Calibration Error of Probe Array Element Three with Impedance Loading at Other Elements....43
30. Magnitude of the Calibration Error of Probe Array Element Five (Farthest from the Plate) with Impedance Loading at Other Elements....44
31. Near-Field RCS Measurement Set-up Where the Circular Array Generates a Plane Wave Illumination over the Target Zone on Transmit and Records the Scattered Near-Field on Receive....48
32. Relative Illumination Error over a Target Zone of d=20 λ, When Illuminated by an 11-Element Array from a Distance r=800λ....50
33. Current Im at Element *m* Induces an Open-Circuit Voltage Vnm at Element *n*....52
34. Circular Arc Array with Dipole Elements and RCS Target, an Infinite Circular Cylinder....54
35. (a) Relative Illumination Error over a 20λ Diameter Target Region by an Array with N=8 Elements, Arc Angle Φ=15˚, Radius r = 40. (b) Normalized Array Excitation for the 8-Element Array....55
36. (a) Relative Illumination Error over a 20λ Diameter Target Region by an Array with N=15 Elements, Arc Angle Φ=30˚, Radius r = 40λ (b) Normalized Array Excitation for the 15-Element Array....56
37. (a) Relative Illumination Error Over a 20λ Diameter Target Region by an Array with N=29 Elements, Arc Angle Φ=60˚, Radius r = 40λ. (b) Normalized Array Excitation for the 29-Element Array....57
38. (a) Coupling-Perturbed Array Excitation (Full Line) and Ideal Array Excitation (Dashed Line) for an Array with N=15 Elements, Arc Angle Φ=30˚, Radius r = 40λ (b) Relative Illumination Error over the 20λ Diameter Target Zone....60
39. Scattering from a Cylinder: (a) Coupling-Perturbed Received Signal $\mathbf{v}^{at}$ with Target and the Received Signal $\mathbf{v}^{a}$ without Target (b) Signal Difference $\Delta\mathbf{v}$ with and without Target....61
40. The Target Scattering Signal $\mathbf{v}^{t}$....61
41. Comparison of the Scattered Field as Obtained by Array Measurement and the Scattered Field According to GO....62
42. Direct and Parasitic Excitation Mechanisms Contributing to the Total Array Radiation....63
43. The Receive Array....64
44. Reflection of Ray Tube at the Target Cylinder....66
45. The Radius of Curvature....67
46. Derivation of the Incident Angle θ....68
47. Illustrating the Incidence Angle θ Corresponding to a Ray Reflected to Point (r,φ)....69
48. Near-Field Bistatic RCS Measurement Set-up with r=7.5 m and a=1.8 m....70
49. Error Resulting from Different Weighting of the Target Zone Vs. the null sector: a) Relative Error Over Target Zone, b) Error Over Null Sector, c) Radiation Intensity in the Plane of the Array and the Target Zone....74

Approved for public release; distribution unlimited.

List of Tables

Table **Page**

1. Summary of the Magnitude of Calibration Error with Impedance Loading for Free Space Calibration.....37
2. Summary of the Magnitude of Calibration Error with Impedance Loading for In-Situ Calibration.....41
3. Target Illumination Error vs. Element Density in the Illuminating Array 49
4. Maximum RMS Error in Plane Wave Illumination Over a 20λ Target Zone for Various Array Geometries 58
5. Results at f = 0.5 GHz for Three Arrays of Arcs Φ of 15˚, 30˚, and 60˚, with *N*=2, *N*=3 and *N*=6 Elements, Respectively 71
6. Results at f = 2.0 GHz for Three Arrays of Arcs Φ of 15˚, 30˚, and 60˚, with *N*=6, *N*=12 and *N*=24 Elements, Respectively 72
7. Results at f = 10.0 GHz for Three Arrays of Arcs Φ of 15˚, 30˚, and 60˚, with *N*=30, *N*=60 and *N*=120 Elements, Respectively 72

Approved for public release; distribution unlimited.

1 Introduction

The antenna pattern and bistatic radar cross section (RCS) are the far-field (FF) properties associated with an antenna and a target, respectively. Therefore, they are often measured in outdoor test ranges that are expansive enough to accommodate the minimum FF distance, $2L^2/\lambda$, where L is the linear dimension of the device under test (DUT) and λ the wavelength. As an example, the minimum FF distance for a DUT with $L = 5\ m$ at 10 GHz ($\lambda = 3\ cm$) is about $1,670\ m$. With urban and suburban sprawl taking place many parts of the country, it is becoming increasingly difficult to find a large parcel of land that is free of RF interference and located near where antenna and RCS research and development activities are taking place.

Antenna FF patterns can also be measured inside an anechoic chamber using a compact-range reflector, which acts as a spatial filter to receive/transmit a plane-wave component propagating in a particular direction. The principal advantage of indoor measurement is that measurements are not subject to external RF interferences and environmental conditions. As a result, measurements are, in general, highly repeatable and accurate. Furthermore, once built and furnished, an anechoic chamber is less expensive to operate and maintain than an outdoor range. One significant disadvantage of indoor antenna measurement using a compact-range reflector is that the compact-range reflector's quiet-zone size sets a hard limit on the size of the largest antenna that can be measured. As a result, large antennas and phased-array systems are generally not measured using a compact-range reflector. In order to deal with the FF-distance issue, the antenna research community has developed near-field (NF) measurement techniques [1] [2]. Radiated fields are measured in the vicinity of an antenna using a small probe so as not to greatly disturb the current distribution on a DUT. The collected NF samples are then processed to produce FF patterns. The processing, known as the NF-to-FF transformation [1][2], is exact and rigorous in that, if error-free NF samples are collected over a closed scan surface, it is capable of producing the exact FF of an antenna, regardless of its excitation and radiation mechanisms. Since only NF samples are required, measurement can be performed inside an anechoic chamber. Antennas are nowadays routinely measured using the NF techniques.

Recently, the Sensors Directorate of the Air Force Research Laboratory has successfully applied the probe-corrected cylindrical NF scanning technique to target bistatic RCS measurement [3], demonstrating that the fully polarimetric bistatic RCS of a target can be determined inside a secure anechoic chamber using the combination of a compact range reflector (to provide the necessary plane wave illumination) and a NF scanning system. NF samples are almost always collected using a single-probe NF scanning system. A single probe mechanically scans around a DUT over a planar, cylindrical, or spherical surface to collect NF samples. Since the radiated/scattered field of a finite-size DUT is spatially band-limited, NF samples must be collected at a spatial sampling rate that is commensurate with the frequency and the DUT size. As the DUT's electrical size increases, so does the required spatial Nyquist-sampling rate. Since the NF-sample acquisition time is, to first order, proportional to the square of the spatial-sampling rate, it can be time-consuming for a single probe to collect all the required NF samples of an electrically large DUT. One way of reducing the NF acquisition time is to use an array of multiple probes and simultaneously collect the required NF samples at multiple scan positions [4].

Figures 1 and 2 show how a multi-probe system can be used for antenna (including phased-array antennas) measurement in spherical NF scanning and for target bistatic RCS measurement in cylindrical NF scanning, respectively. Unlike antenna measurement, target bistatic RCS measurement requires a plane-wave illumination, which can be provided, for example, by a compact-range reflector [4][3] .

Shown in Figure 3 is the estimated NF-sample acquisition time versus target size for bistatic RCS applications [4]. For a Tomahawk-class cruise missile ($L \approx 6.25\ m$) at 10 GHz, the estimated time is about 100 hours for each illumination direction when a compact-range reflector is used as a plane-wave illuminator and a single probe is used. If the NF samples are collected using a one-dimensional probe array,

Approved for public release; distribution is unlimited.

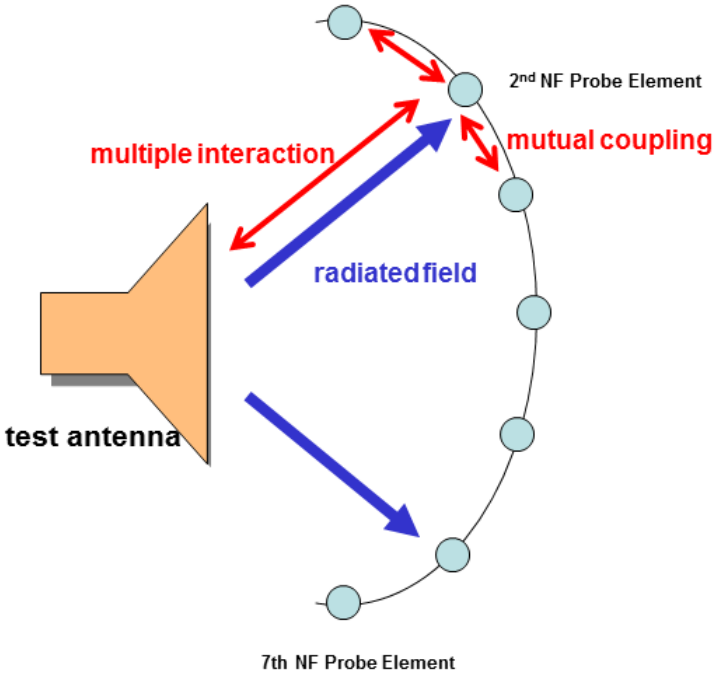

Figure 1: NF-Sample Acquisition Using a Spherical Multi-Probe Scanner for Antenna Measurement

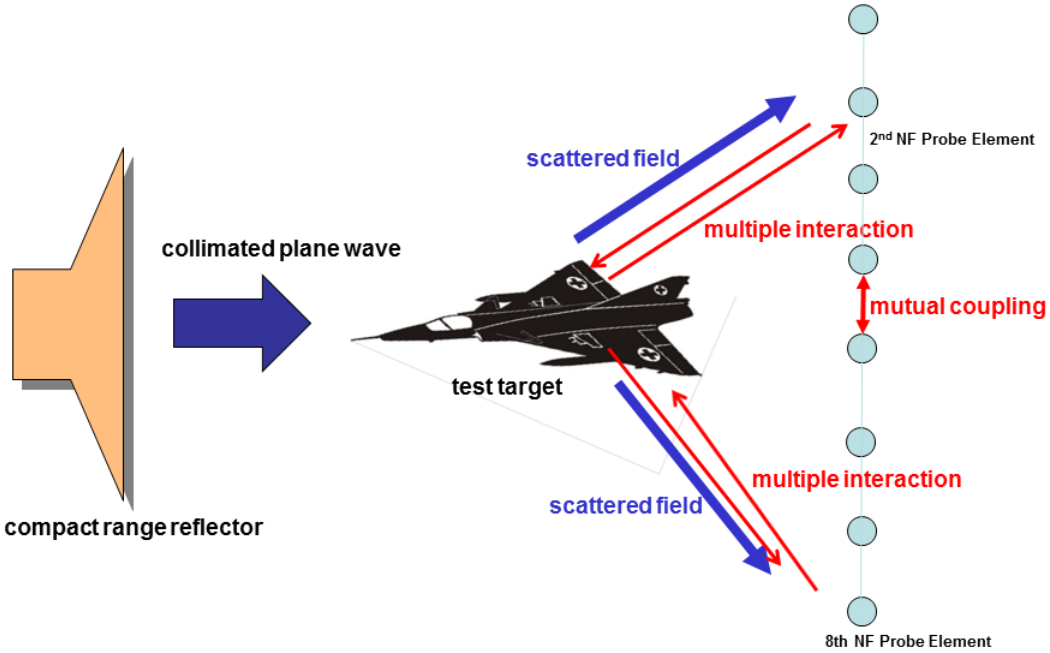

Figure 2: NF-Sample Acquisition Using a Cylindrical Multi-Probe Scanner for Bistatic RCS Measurement

Approved for public release; distribution is unlimited.

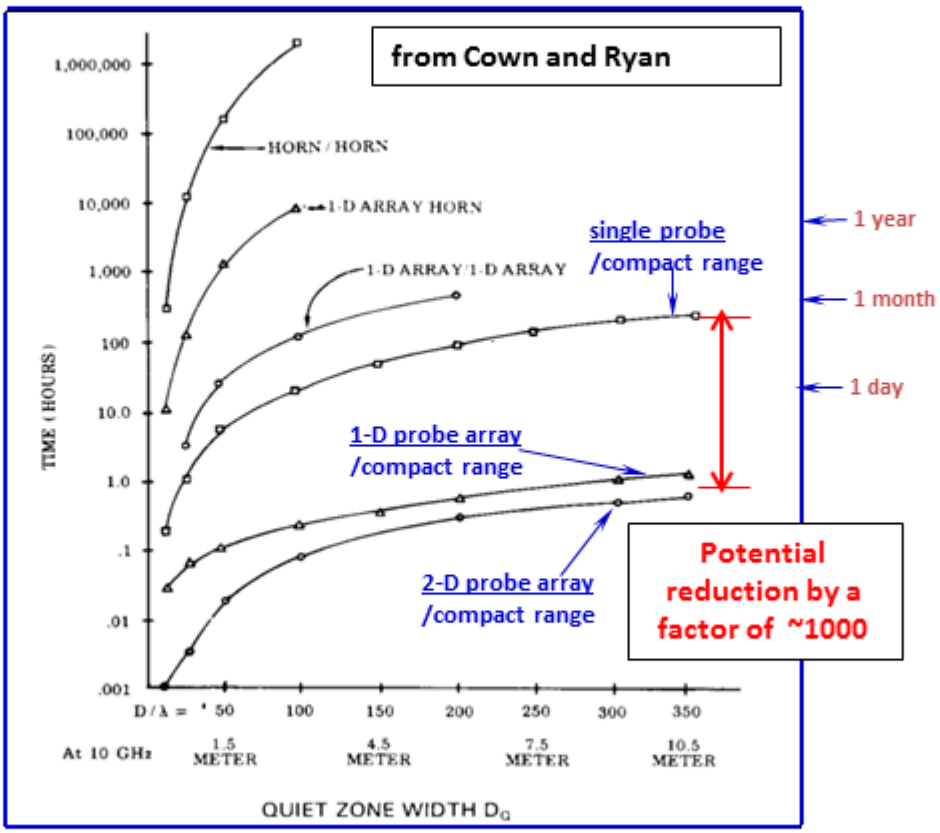

Figure 3: NF Sample Acquisition Time vs. Antenna/Target Size, Adopted from [4]

the estimated time drops to approximately 30 minutes, expediting the sample acquisition by a factor of 200. In the extreme case shown in the figure, the use of a single probe was estimated to take about 300 hours for a DUT with $L = 10.5m$, while the use of a two-dimensional probe array cuts this down to less than 20 minutes–a nearly 1000-fold reduction. Since the publication of [4], a number of commercial NF scanner manufacturers began producing high-performance NF scanning systems for the commercial and defense markets. Some of these single-probe systems can now achieve high scan speeds with low probe-position errors. However, with a continuing need to characterize electrically large antennas and phased-array systems and with a growing interest in bistatic RCS, it has become even more important to develop rapid NF-collection techniques.

The design and fabrication of a modern high-performance NF scanner is a fairly complex endeavor requiring expertise from many, disparate engineering disciplines, such as electromagnetics, civil, control, mechanical, and structural engineering. A multi-probe NF scanner comes with an additional set of challenges. One of the principal electromagnetic challenges is to reduce or control the multiple scattering (MS) between a DUT and a probe array and the mutual coupling (MC) between the probes in the array. When a single probe is used, the MS between a DUT and the probe is often small and ignored. Indeed, in most practical situations, fairly accurate FF can be determined without explicitly considering a probe's scattering characteristics. However, when a probe array is used, the total size of the measurement aperture increases significantly, which in turn increases the MS between the probe array and a DUT. The MS alters the current distribution on the DUT from that induced by the primary incident plane wave from a compact-range reflector in bistatic RCS measurement or by a feed or generator in antenna measurement. Therefore, the MS may degrade the accuracy of the collected NF samples. Similarly, the MC between the probes in the array alters their receiving characteristics. As a result, the received signal at each probe in the array is not the same as that obtained by mechanically scanning a single probe. If uncorrected, the MC leads to incorrect FF radiation/scattering patterns. Because of the MS between the probe and the DUT, the MC between the probes in the array also depends on the orientation of the array with respect to the

Approved for public release; distribution is unlimited.

DUT and is likely to change as the array orientation with respect to the DUT changes [5]. Thus, MC compensation in the presence of a strong MS can be complicated and time-consuming. Thus, an effective MS-reduction technique may simplify the MC compensation [5], underscoring the importance of reducing the MS.

A limited number of commercial off-the-shelf spherical multi-probe scanners are presently available, primarily for testing cellphone and vehicular antennas, which have low gains and high sidelobes by military standards. These systems, however, do not compensate MS and MC effects [6]. The manufacturer has attempted to reduce the MC effects between the probes by placing them apart, as wide as 2.50^o in one model. (The probes are also partially embedded in radar absorbing material.) The manufacturer similarly has attempted to reduce the MS effects between the array and a DUT by setting the scan radius at a relative large distance from the DUT. In spherical NF scanning, the angular sampling interval must be less than $\pi/\text{INT}(kL/2 + 10)$, where $k = 2\pi/\lambda$ is the wavenumber and INT represents the integer function [2]. AFRL's OneRY Indoor Range can presently accommodate a DUT as large as $L = 12' \approx 3.6m$ (determined by the compact-range dish's quiet-zone size) and frequency as high as 40 GHz. For a DUT with $L = 3.6m$ at 40 GHz, the Nyquist angular interval is approximately 0.425^o. If the available angular spacing between the probes is greater than the Nyquist interval, it is necessary for bistatic RCS measurement to rotate the entire probe array relative to a DUT in order to collect all the required NF samples, which negates some of the advantages offered by a multi-probe system. (Rotating the DUT relative to the probe array, which can be done far more easily easily, will not work for bistatic RCS measurement. After the rotation, the DUT will be in a different angular position relative to the incident field and thus will have a different current distribution.) Thus, it is important to devise an effective MC mitigation technique that is applicable to high-density probe arrays in order to preserve the inherent advantages of multi-probe NF scanning. Likewise, it is also important to formulate an effective MS-mitigation technique that is applicable to a scan radius that is more commensurate with the DUT size, since the scan radius requirement determines not only the maximum DUT size but also ultimately the size of an anechoic chamber.

We have recently examined a number of MS-reduction approaches. We investigated the possibility of employing an active loading technique on single-mode dipole probes to cancel the induced current that gives rise to the MS effects. Using the classical network theory, we also showed the importance of a careful in-situ calibration of the probe array in the presence of a DUT [5]. We, in addition, examined the possibility of designing low-backscatter, open-waveguide probes and dipole probe arrays to reduce the MS for possible use in cylindrical NF scanning [8].

The remainder of this report consists of three sections. Each section deals with a different aspect of the electromagnetic issues associated with NF scanning with a probe array and has its own introduction, main body and summary. Thus, each chapter can be read independently. In Section 2, we investigate an alternative approach to reducing the MS effects. Harrington [7] and others have shown that it is possible to reduce the total scattered energy of an object by impedance-loading it. In order to examine the efficacy of the impedance-loading technique, we cast the complicated MS between a probe array and a DUT and the MC between the probes as a classical multiple-scattering problem [9]. We formulate the problem using the Foldy-Lax self-consistent multiple-scattering formalism [10] and the T matrix [11]. A critical input to this computational approach is the antenna-scattering matrix [15] of a probe, which succinctly describes how the probe absorbs, receives, transmits, and scatters electromagnetic energy. We discuss how the antenna-scattering matrix can be determined from a method-of-moments impedance matrix for an arbitrarily loaded probe. Using the multiple-scattering approach, we explicitly show that an array of short-circuited dipole probes produces MS effects that are strong enough to perturb the induced current distribution whose FF deviates noticeably from the ideal one. This underscores the importance of reducing the MS between a probe array and a DUT. We then show that, when each probe of the array is reactively loaded, the MS is reduced significantly and the resulting current distribution produces the correct FF. It is well known that an antenna that scatters less energy also absorbs less energy [16][17], leading to a low signal-to-noise ratio. We suggest a possible way to overcome the low SNR problem.

Approved for public release; distribution is unlimited.

In Section 3, we consider for bistatic RCS applications the performance of a probe array employing a time varying load impedance at one probe element to improve the efficiency of measuring the amplitude and phase of the NF scattered by a target. The time varying field scattered by the probe array is observed at a remote measurement probe [18]. Accurate measurements require characterization of the interaction between (1) probe array elements, (2) array elements and the target being measured, and (3) array elements and the remote measurement probe in terms of the self and mutual impedances. The measured voltage is the linear superposition of the plane wave/target induced voltages at all array terminals. A signal flow graph representation shows how the coupling between array elements introduces these superposition errors and demonstrates that open circuit conditions eliminates the errors. We examine errors in measurement that occur when free space impedances are used in lieu of in-situ impedances. With in-situ calibration, the measurement error decreases monotonically with decrease in the probe array terminal currents. The accuracy of the measurements is limited significantly when the free space impedances are used, no matter how small the currents at the other terminals are constrained. It is important to determine the limits in measurement accuracy associated with the use of free space mutual impedances, especially for probe array elements near the target. Should this accuracy be unsatisfactory, the feasibility of providing in-situ calibration of the modulated scattering probe array must be considered, a process that will degrade measurement efficiency and accuracy.

The use of a compact-range reflector to provide a plane-wave incident field for bistatic RCS applications has a drawback when one attempts to measure bistatic RCS at small bistatic angles. This occurs because one cannot place a probe between the compact-range reflector and a target without destroying the plane-wave nature of the incident field. To overcome this limitation, in Section 4 we explore an approach, where an array of antenna elements is used to simultaneously illuminate the target and measure the scattered NF. In this preliminary study we consider a single circular-arc array with simultaneous transmit and receive modes. The array and the target lie in the same plane, i.e., we consider a quasi two-dimensional case. Assuming single-mode elements in the array, we analyze the perturbations in the transmitted and in the received signals caused by the mutual coupling in the array and by the array-target interaction, and develop techniques to correct these perturbations. The techniques are based on the mutual-impedance matrix which is obtained from the measured scattering matrix of the array. A detailed example of an array with dipole elements and a target in the form of a conducting infinite cylinder is included. A useful feature is that a modest-size circular array can generate an approximately planar wave at a considerably closer distance than the minimum FF distance $2L^2/\lambda$. However, a potential measurement problem is that the MC in the array greatly dominates the desired target signal and thus a robust MC-compensation technique is required.

Approved for public release; distribution is unlimited.

2 Suppression of Multiple Scattering between a DUT and a Probe Array

2.1 Introduction

In this section, we investigate the feasibility of reducing the multiple scattering (MS) between a DUT and a multi-probe NF scanning array. The MS, if not controlled, can perturb the current distribution on a DUT that may deviate significantly from the ideal distribution induced by a primary excitation source. The perturbed current distribution then produces NF samples that diverge from the ideal ones, leading to errors in the reconstructed far fields (FFs).

One way of reducing the MS is to separate a DUT and a NF probe array as apart as possible. As noted in the previous section, this may negate some of the advantages offered by the NF approach. In addition, wider separation also requires a larger NF scanning structure, which may in turn require a higher structural rigidity of the scanning system. A potential way of reducing MS, without increasing scan radii/distances, is to reactively load the probes, making them scatter less energy [16] which leads to reduced MS effects. However, reactive loading also makes probes absorbs less energy, leading to a lower signal-to-noise ratio (SNR) at each probe. Because of this reason, the reactive loading technique is not generally used in radar antennas. The electromagnetic environment in which a radar system operates produces target returns that may decorrelate in a small fraction of a second. However, the electromagnetic environment in a well designed and maintained anechoic chamber stays stable for a long period of time. As a result, it may be possible to coherently integrate received signals to boost the SNR at each impedance-loaded probe. Thus, as long as the coherent-integration time is shorter than the time for the probe of a traditional single-probe system to traverse the length of the probe array, a multi-probe system with impedance-loaded probes may offer a greater data-collection efficiency.

In order to examine the efficacy of the reactive-loading approach, we cast as a multiple-scattering problem the complicated electromagnetic processes taking place between a DUT and the elements of an array. A number of computational techniques can be used to solve the resulting multiple-scattering problem. In this report we choose to use the multiple-scattering technique of Peterson and Ström [9] that is based on the Lax-Foldy self-consistent multiple-scattering formalism [10] and the T matrix [11]. This approach is ideal for investigating MS and MC effects involving electrically small- to moderate-size probes. Its chief advantage is that the number of unknowns, which ultimately determines the overall computational cost, is often lower than those associated with more popular numerical approaches [12], such as the method of moments. Furthermore, with this approach it is less cumbersome to separate the MS and MC contributions from the total fields, making it correspondingly less troublesome to assess the extent of multiple-interaction effects. In order to take advantage of the formalism [9] for the multiple-scattering problem at hand, it is necessary to generalize the T matrix [11]. The T-matrix was originally developed for a pure scattering object. A probe, unlike a pure scattering object, has a port since it is necessary to collect the NF radiated/scattered by a DUT. Thus, it is necessary to introduce a probe's absorbing, receiving, and transmitting properties in addition to its scattering properties in order to satisfy energy conservation. This can be done by using R. Dicke's antenna scattering matrix formalism [15]. In the traditional NF scanning with a single probe, the MS between a DUT and the probe is usually deemed small and thus ignored. As a result, only the probe's absorbing, and transmitting/receiving properties are required to perform probe correction and its scattering properties need not be characterized. However, in order to assess the MS and MC effects for a multi-probe NF system, one needs to characterize not only the probes' receiving and transmitting properties, which are related through reciprocity for most probes [2], but also their scattering properties.

2.2 Antenna Scattering Matrix

Approved for public release; distribution is unlimited.

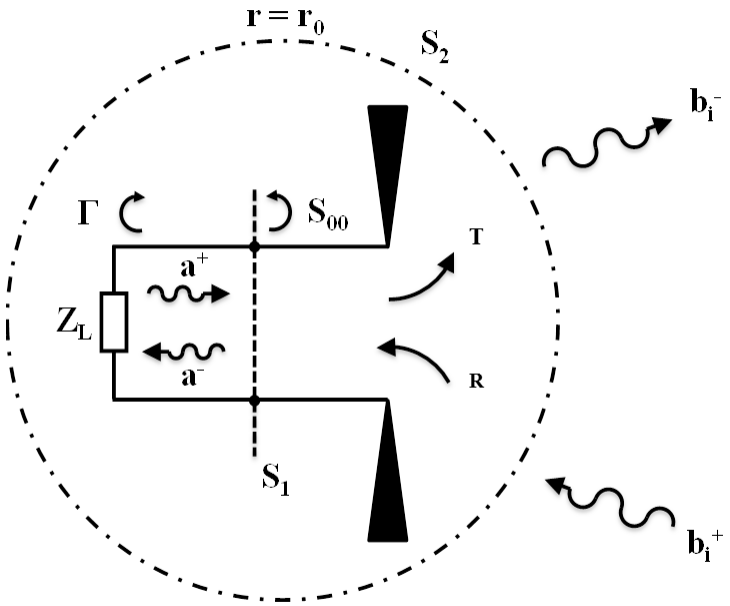

Figure 4: The Antenna Matrix Representation of a Generic, Linear, Lossless Antenna

In this subsection, we review Dicke's antenna-scattering matrix [15], that completely characterizes a probe's absorbing, receiving, transmitting, and scattering properties. Consider Figure (4) which shows the antenna-scattering matrix [15] description of a generic, linear, lossless antenna with a single port. In the figure, the surface S_1 represents the transition surface from a transmission line to the antenna, while the surface S_2 represents the spherical surface of radius, r_0, the minimum radius of the antenna. When the antenna is in its receiving mode, it is excited by an incoming wave whose spherical-wave expansion coefficients are denoted by $\mathbf{b}^{(+)}$. Part of the incident energy is received by the antenna as determined by its receiving coefficients, $\mathbf{R}$, and the rest is scattered by the antenna as determined by its scattering matrix, $\mathbf{S}$. The received energy travels through the transmission line with voltage, $a^{(-)}$, to the load, Z_L, and part of it is then reflected due to impedance mismatch as represented by the load reflection coefficient, $\Gamma(Z_L)$. This reflected energy then gets transmitted (re-radiated) from the antenna, as determined by its transmitting coefficients, $\mathbf{T}$. In the figure, $\mathbf{b}^{(-)}$ represents the spherical-wave expansion coefficients of the total outgoing field, which is the vector sum of the scattered and re-radiated fields. The remainder of the received energy is absorbed by the load to produce the received voltage.

The total antenna-scattering matrix, $\hat{\mathbf{S}}$, expresses the linear relationship between the incoming and outgoing spherical wave expansion coefficients and the voltage values inside the transmission line in terms of the antenna properties, $\mathbf{R}$, $\mathbf{T}$, $\mathbf{S}$, and the antenna reflection coefficient, S_{00}.

$$\begin{bmatrix} a^{(-)} \\ \mathbf{b}^{(-)} \end{bmatrix} = \begin{bmatrix} S_{00} & \mathbf{R}^t \\ \mathbf{T} & \mathbf{S} \end{bmatrix} \begin{bmatrix} a^{(+)} \\ \mathbf{b}^{(+)} \end{bmatrix} \equiv \left[\hat{\mathbf{S}}\right] \begin{bmatrix} a^{(+)} \\ \mathbf{b}^{(+)} \end{bmatrix}, \tag{1}$$

where the superscript, t, denotes transpose. The voltage $a^{(-)}$ contains information about the radiated/scattered NF sampled at a particular scan location and is a critical input to the NF-to-FF transformation. The expansion coefficients $\mathbf{b}^{(-)}$ of the total outgoing field determines the extent of MS and MC effects, both of which must be reduced.

For a probe with electrical size, kr_o, $\mathbf{R}$ and $\mathbf{T}$ are column vectors of length $2P$, where $P = L(L+2)$ and $L = INT(kr_o) + l_o$ with l_o being a small integer. $\mathbf{S}$ is a square matrix of dimension $2P$. Since a probe is not electrically large, $\hat{\mathbf{S}}$ is a moderate-size square matrix.

Approved for public release; distribution is unlimited.

Following [2], and using the source-scattering-matrix formulation [19], $a^{(-)}$ and $\mathbf{b}^{(-)}$ may be expressed in terms of the components of the total scattering matrix, $\hat{\mathbf{S}}$.

$$a^{(-)}(Z_L) = \frac{1}{1-\Gamma(Z_L)S_{00}}\mathbf{R}^{\mathbf{T}}\mathbf{a}^{(+)} \equiv \left[\hat{\mathbf{R}}(Z_L)\right]\mathbf{a}^{(+)} \quad (2)$$

$$\mathbf{b}^{(-)}(Z_L) = \left[\frac{\Gamma(Z_L)}{1-\Gamma(Z_L)S_{00}}\mathbf{T}\otimes\mathbf{R}^{\mathbf{T}}+\mathbf{S}\right]\mathbf{a}^{(+)} \equiv [\boldsymbol{\tau}(Z_L)]\,\mathbf{b}^{(+)}, \quad (3)$$

where $\otimes$ denotes the outer product operation involving two vectors and we emphasized the dependence of $a^{(-)}$, $\mathbf{b}^{(-)}$ and Γ on Z_L.

$\mathbf{R}$ and $\mathbf{T}$, which are in general related through reciprocity, are required input parameters for probe correction [2]. They can easily be measured in an anechoic chamber or computed using a numerical method. However, the scattering matrix, $\mathbf{S}$, requires complex (I&Q) bistatic scattering data at many incident and scattering angles over 4π steradian with the angular sampling rate commensurate with the electrical size of the probe. For a simple probe such as the dipole probe, we may determine $\hat{\mathbf{S}}$ using a computational technique. In our recent research, we have shown that the "effective T-matrix," $\boldsymbol{\tau}(Z_L)$, which relates the incoming field to the total outgoing field, can accurately be determined directly from the method-of-moment impedance matrix based on the electric field integral equation (EFIE) and the Rao-Wilton-Glisson basis function [12]. We have also applied a similar technique to the EFIE with the thin-wire reduced kernel and the one-dimensional roof-top basis function to extract $\boldsymbol{\tau}(Z_L)$ for an arbitrarily loaded linear dipole probe [20]. The "effective" receiving coefficients, $\hat{\mathbf{R}}(Z_L)$, can also be determined using a computational technique. However, unlike $\boldsymbol{\tau}(Z_L)$, its numerical determination does not require an extraction technique.

2.3 Effects of Loading on a Dipole Probe

As shown by earlier work [7], and predicted by (3), it is possible to modify the total outgoing field of a probe using the impedance loading technique, thereby altering its scattering characteristics. An electrically small dipole probe is particularly well suited for this purpose, as it is a predominantly single-mode antenna in that the shape of its FF pattern is largely independent of the load impedance. In addition, cross dipoles are believed to be used as probes in commercial multi-probe NF arrays. Shown in Figure 5 is the dependence of the FF bistatic scattering patterns of a dipole on the load impedance. The dipole is 0.475 λ long and 0.002 λ thick. As evident from the figure, all the patterns are approximately of the same shape, an important property of a single-mode antenna. Plotted in blue and green are the FF patterns when the dipole probe is short- and open-circuited, respectively. The open-circuit curve is about 22 dB lower than the short-circuit curve. Compared with these two curves are the reactively loaded patterns, all of which are lower than the open-circuit curve by about 5 dB. We have also validated the results shown in Figure 5 using the NEC-4 code [21].

One important disadvantage of the impedance-loading technique for reducing MS and MC effects is that it may also reduce the absorbed voltage, $a^{(-)}$, thereby resulting in a low signal-to-noise ratio (SNR). Similarly, the receiving efficiency of a dipole probe decreases as its electrical size decreases, which may also result in a low SNR at the lower end of a frequency band. There are a couple of ways to deal with this low SNR issue. One obvious way is to increase the transmit power of the antenna under test for antenna measurement or of the compact-range reflector for bistatic RCS measurement. If this is not possible or fails to provide an acceptable SNR, one may employ the coherent-integration technique. The idea is that the random noise components tend to cancel out while the signal components add up coherently, thereby producing higher SNRs. In radar applications, the number of times received signals can be coherently integrated is generally limited by the decorrelation time of a target signal, thereby limiting the extent of the SNR boost. However, the anechoic chamber RF environment is expected to remain stable long enough to allow an adequate number of signal samples to be coherently integrated to produce an acceptable SNR at each scan point. Thus, multi-probe scanning with an array with N probes would be advantageous over

Approved for public release; distribution is unlimited.

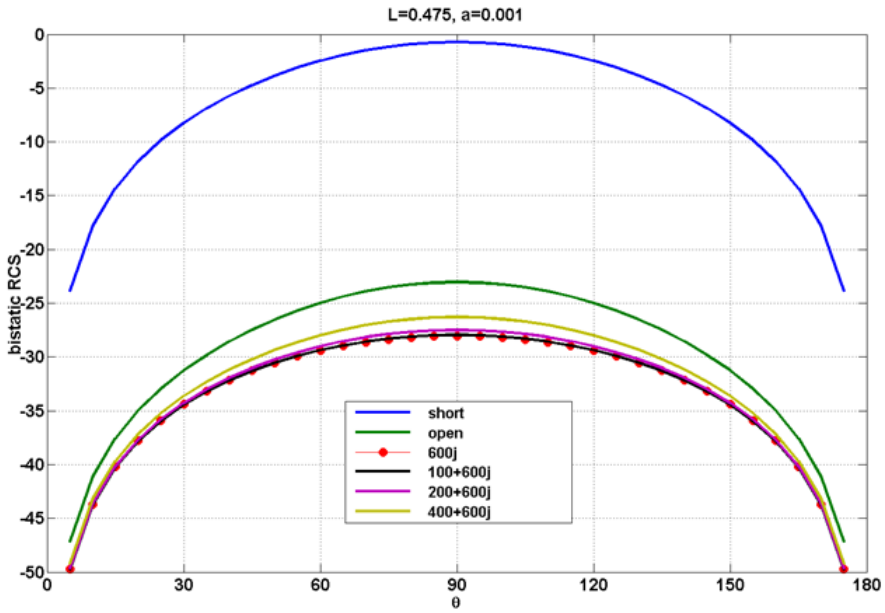

Figure 5: Comparison of the FF Scattering Patterns from an Impedance-Loaded Dipole Probe with a Broadside Illumination

single-probe scanning if the coherent-integration time is shorter than the time for the single probe to mechanically traverse the N scan points.

2.4 Multiple-Scattering Formulation

In this subsection, we describe a computational formalism to account for all the multiple scattering (MS) between a DUT and an array as well as the mutual coupling (MC) between the probe elements for the purpose of examining the efficacy of the impedance loading approach in reducing MI and MC effects. We assume that the interaction between the DUT and a scanner structure, which is often covered with radar absorbing material (RAM), is negligible. Furthermore, the MC effects are computed using the free-space Green function. We also ignore the MS between a positioner and the DUT as well as the MS between the former and the probe array. Since positioners are usually covered with RAM, they are not expected to produce strong MS. Thus, the only MS we are considering is the one between the DUT and the probe array.

We present a formulation for an arbitrary DUT for bistatic RCS applications [3]. Thus, we will use the terms "DUT" and "target" interchangeably. A similar formulation can also be constructed for NF scanning for antenna applications but not presented in this report. Our objective is to express the coefficients, $\hat{a}_i^{(-)}(Z_L)$ and $\hat{\mathbf{b}}_i^{(-)}(Z_L)$, of the ith probe element with $i = 1,\ ...,\ N$, in the combined presence of the other $N-1$ probe elements and of the DUT. Due to MS and MC, they will deviate from their isolated, free-space counterparts, (3), that can be determined using the extraction techniques discussed above [12] [14]. In the presence of the probe array, the T matrix of the DUT, $\hat{\mathbf{T}}_{tg}$, will also deviate from the corresponding isolated, free-space counterpart, $\mathbf{T}_{tg}$. Using the multiple-scattering formalism, we wish to express $\hat{a}_i^{(-)}(Z_L)$, $\hat{\mathbf{b}}_i^{(-)}(Z_L)$ and $\hat{\mathbf{T}}_{tg}$ in terms of their isolated counterparts, $a_j^{(-)}(Z_L)$, $\mathbf{b}_j^{(-)}(Z_L)$ and $\mathbf{T}_{tg}$ (with $1 \leq i, j \leq N$) for a given scan configuration.

As before, we assume that a DUT, located at the origin, is illuminated by an incident field from a compact-range reflector as shown in Figure 2. We further assume that the spatial distribution of the incident field is sufficiently localized so that it has a negligible amount of energy outside the quiet zone. (This is not strictly true, especially in the forward-scattering region. In reality, the electric field captured

Approved for public release; distribution is unlimited.

by a probe, even though located well outside the quiet zone contains not only desired scattered NF but also a spillover incident field from the compact-range transmitter. [3] discusses a first-order technique for excising the spillover field from the total field.)

Let $\bar{r}_i$ represent the location of the ith probe and $\tau(\bar{r} - \bar{r}')$ the translation matrix (TM) of the transverse vector spherical multipole fields (TVSMF) [23] [24] [25]. The TM acts as a propagator that determines the strength of the interaction between a TVSMF at $\mathbf{r}$ with another TVSMF at $\mathbf{r}'$. We assume that the probes in the array are identical and denote their free-space antenna scattering matrix by $\hat{\mathbf{S}}$. We let $\mathbf{T}_{tg}$ represent the T matrix of the target in isolation (i.e., no NF array present). Then, in the absence of the probe array the scattered field, $\mathbf{E}_{sc}(\mathbf{r})$, is related to the plane-wave incident field produced by a compact-range reflector, $\mathbf{E}_{inc}(\mathbf{r})$ via $\mathbf{T}_{tg}$,

$$\mathbf{b}_{tg}^{(-)} = \mathbf{T}_{tg}\mathbf{b}_{tg}^{(+)}, \tag{4}$$

where $\mathbf{b}_{tg}^{(+)}$ and $\mathbf{b}_{tg}^{(-)}$ represent column vectors containing the spherical-wave expansion coefficients of $\mathbf{E}_{inc}(\mathbf{r})$ and $\mathbf{E}_{sc}(\mathbf{r})$, respectively. In the presence of the probe array, the total incident field, $\hat{\mathbf{E}}_{inc}(\mathbf{r})$, on the target is the sum of the plane-wave incident field from the compact-range reflector and the fields scattered indirectly by the N probes. Thus,

$$\hat{\mathbf{E}}_{inc}(\mathbf{r}) = \mathbf{E}_{inc}(\mathbf{r}) + \sum_{i=1}^{N} \mathbf{E}_{sc}^{i}(\mathbf{r} - \mathbf{r}_i), \tag{5}$$

where $\mathbf{E}_{sc}^{i}(\mathbf{r} - \mathbf{r}_i)$ represents the scattered field from the ith probe. Thus, the outgoing expansion coefficients, $\mathbf{b}_{tg}^{(-)}$, of the target in the presence of the array can be expressed as,

$$\hat{\mathbf{b}}_{tg}^{(-)} = \mathbf{b}_{tg}^{(-)} + \sum_{i=1}^{N} \mathbf{T}_{tg}\tau(-\mathbf{r}_i)\hat{\mathbf{b}}_{i}^{(-)} \tag{6}$$

where $\tau(-\mathbf{r}_i)$ represents the TM of the TVSMF and $\hat{b}_i^{(-)}$ the expansion coefficients of the outgoing field of the ith probe in the presence of the target. The total incident field on the nth probe is the sum of the scattered field from the target and the fields scattered indirectly by the other $(N-1)$ probes in the array. Thus,

$$\hat{\mathbf{b}}_{n}^{(+)} = \tau(\mathbf{r}_n)\hat{\mathbf{b}}_{tg}^{(-)} + \sum_{i=1, i\neq n}^{N} \tau(\mathbf{r}_n - \mathbf{r}_i)\hat{\mathbf{b}}_{i}^{(-)}, \qquad n = 1,\ ...,\ N. \tag{7}$$

We may express (4) – (7) in matrix form.

$$\hat{\mathbf{b}}_{tg}^{(+)} = \mathbf{b}_{tg}^{(+)} + \tau_{\ominus}\hat{\mathbf{b}}_{ar}^{(-)} \tag{8}$$

$$\hat{\mathbf{b}}_{tg}^{(-)} = \mathbf{b}_{tg}^{(-)} + \mathbf{T}_{tg}\tau_{\ominus}\hat{\mathbf{b}}_{ar}^{(-)} \tag{9}$$

and

$$\hat{\mathbf{b}}_{ar}^{(+)} = \tau_{\oplus}\hat{\mathbf{b}}_{tg}^{(-)} + \tau_{ar}\hat{\mathbf{b}}_{ar}^{(-)}, \tag{10}$$

Approved for public release; distribution is unlimited.

where

$$\begin{aligned}
\hat{\mathbf{b}}_{ar}^{(+)} &\equiv \left[\hat{\mathbf{b}}_1^{(+)}, \hat{\mathbf{b}}_2^{(+)},\ ...,\ \hat{\mathbf{b}}_N^{(+)}\right]^t, \\
\hat{\mathbf{b}}_{ar}^{(-)} &\equiv \left[\hat{\mathbf{b}}_1^{(-)}, \hat{\mathbf{b}}_2^{(-)},\ ...,\ \hat{\mathbf{b}}_N^{(-)}\right]^t, \\
\tau_{ar} &\equiv \begin{bmatrix} \overline{\overline{0}} & \tau(\mathbf{r}_{12}) & \cdots & \tau(\mathbf{r}_{1N}) \\ \tau(\mathbf{r}_{21}) & \overline{\overline{0}} & \cdots & \tau(\mathbf{r}_{2N}) \\ \cdots & \cdots & \cdots & \cdots \\ \tau(\mathbf{r}_{N1}) & \tau(\mathbf{r}_{N2}) & \cdots & \overline{\overline{0}} \end{bmatrix}, \\
\tau_{\oplus} &= \left[\tau(\mathbf{r}_1),\ \tau(\mathbf{r}_2),\ \cdots,\ \tau(\mathbf{r}_N)\right]^t, \\
\tau_{\ominus} &= \left[\tau(-\mathbf{r}_1),\ \tau(-\mathbf{r}_2),\ \cdots,\ \tau(-\mathbf{r}_N)\right],
\end{aligned}$$

where $\mathbf{r}_{ij} \equiv \mathbf{r}_i - \mathbf{r}_j$ with $i \neq j$ and $\overline{\overline{0}}$ represents the null matrix whose elements are all 0.

The coefficients of the outgoing waveguide modes, $\mathbf{a}_{ar}^{(-)} \equiv \left[a_1^{(-)},\ a_2^{(-)},\ \cdots,\ a_N^{(-)}\right]^t$, and the expansion coefficients, $\mathbf{b}_{ar}^{(-)}$, of the outgoing spherical waves of the array may also be expressed similarly in terms of the coefficients, $\overline{a}_{ar}^{(+)} \equiv \left[a_1^{(+)},\ a_2^{(+)},\ \cdots,\ a_N^{(+)}\right]^T$, of the input waveguide modes and the incoming-wave expansion coefficients, $\overline{b}_{ar}^{(+)}$:

$$\mathbf{a}_{ar}^{(-)} = \mathbf{\Gamma}_{ar}\mathbf{a}_{ar}^{(+)} + \mathbf{R}_{ar}\mathbf{b}_{ar}^{(+)}, \tag{11}$$

and

$$\mathbf{b}_{ar}^{(-)} = \mathbf{T}_{ar}\overline{a}_{ar} + \mathbf{S}_{ar}\mathbf{b}_{ar}^{(+)}. \tag{12}$$

In the above equations, $\mathbf{\Gamma}_{ar}$ is the $N \times N$ diagonal matrix whose diagonal elements are S_{00}; $\mathbf{R}_{ar}^t$ and $\mathbf{T}_{ar}$ are the block-diagonal matrices of size $2NL(L+1) \times N$ whose block entries are $\mathbf{R}^t$ and $\mathbf{T}$, respectively; and $\mathbf{S}_{ar}$ is the block-diagonal matrix of size $2NL(L+1) \times 2NL(L+1)$ whose block entries are $\mathbf{S}$.

Recognizing that $\tau(\mathbf{r}_n)\hat{\mathbf{b}}_{tg}^{(-)}$ represents the field incident on the nth probe resulting from the primary target scattering, we demand the *total scattering matrix*, $\hat{\mathbf{S}}_{ar}$, of the probe array be of the following form:

$$\begin{bmatrix} \mathbf{a}_{ar}^{(-)} \\ \mathbf{b}_{ar}^{(-)} \end{bmatrix} \equiv \hat{\mathbf{S}}_{ar} \begin{bmatrix} \mathbf{a}_{ar}^{(+)} \\ \tau_{\oplus}\mathbf{b}_{tg}^{(-)} \end{bmatrix} \equiv \begin{bmatrix} \hat{\mathbf{\Gamma}}_{ar}\hat{\mathbf{R}}_{ar} \\ \hat{\mathbf{T}}_{ar}\hat{\mathbf{S}}_{ar} \end{bmatrix} \begin{bmatrix} \mathbf{a}_{ar}^{(+)} \\ \tau_{\oplus}\mathbf{b}_{tg}^{(-)} \end{bmatrix}. \tag{13}$$

We want to express $\hat{\mathbf{\Gamma}}_{ar}$, $\hat{\mathbf{R}}_{ar}$, $\hat{\mathbf{T}}_{ar}$, and $\hat{\mathbf{S}}_{ar}$ in terms of their free-space counterparts as well as the scattering properties of the target. Substituting (8), (9) and (10) into (11) and (12), we obtain

$$\mathbf{a}_{ar}^{(-)} = \mathbf{\Gamma}_{ar}\mathbf{a}_{ar}^{(+)} + \mathbf{R}_{ar}\tau_{\oplus}\mathbf{b}_{tg}^{(-)} + \mathbf{R}_{ar}\tau_{\oplus}\mathbf{T}_{tg}\tau_{\ominus}\mathbf{b}_{ar}^{(-)} + \mathbf{R}_{ar}\tau_{ar}\mathbf{b}_{ar}^{(-)}, \tag{14}$$

and

$$\mathbf{b}_{ar}^{(-)} = \mathbf{T}_{ar}\mathbf{a}_{ar}^{(+)} + \mathbf{S}_{ar}\tau_{\oplus}\mathbf{b}_{tg}^{(-)} + \mathbf{S}_{ar}\overline{\overline{\tau}}_{\oplus}\mathbf{T}_{tg}\tau_{\ominus}\mathbf{b}_{ar}^{(-)} + \mathbf{S}_{ar}\tau_{ar}\overline{b}_{ar}^{(-)}. \tag{15}$$

Solving (15) for $\mathbf{b}_{ar}^{(-)}$,

$$\mathbf{b}_{ar}^{(-)} = \left[\mathbf{I} - \mathbf{S}_{ar}\left(\tau_{\oplus}\mathbf{T}_{tg}\tau_{\ominus} + \tau_{ar}\right)\right]^{-1}\left[\mathbf{T}_{ar}\mathbf{a}_{ar}^{(+)} + \mathbf{S}_{ar}\tau_{\oplus}\mathbf{b}_{tg}^{(-)}\right] \tag{16}$$

Upon Substituting (16) into (14) yields,

$$\mathbf{b}_{ar}^{(-)} = \mathbf{\Gamma}_{ar}\mathbf{a}_{ar}^{(+)} + \mathbf{R}_{ar}\tau_{\oplus}\overline{b}_{tg}^{(-)} + \mathbf{R}_{ar}\left[\tau_{\oplus}\mathbf{T}_{tg}\tau_{\ominus} + \tau_{ar}\right]\left[\mathbf{I} - \mathbf{S}_{ar}\left(\tau_{\oplus}\mathbf{T}_{tg}\tau_{\ominus} + \tau_{ar}\right)\right]^{-1}\left[\mathbf{T}_{ar}\overline{a}_{ar} + \mathbf{S}_{ar}\tau_{\oplus}\overline{b}_{tg}^{(-)}\right]. \tag{17}$$

Approved for public release; distribution is unlimited.

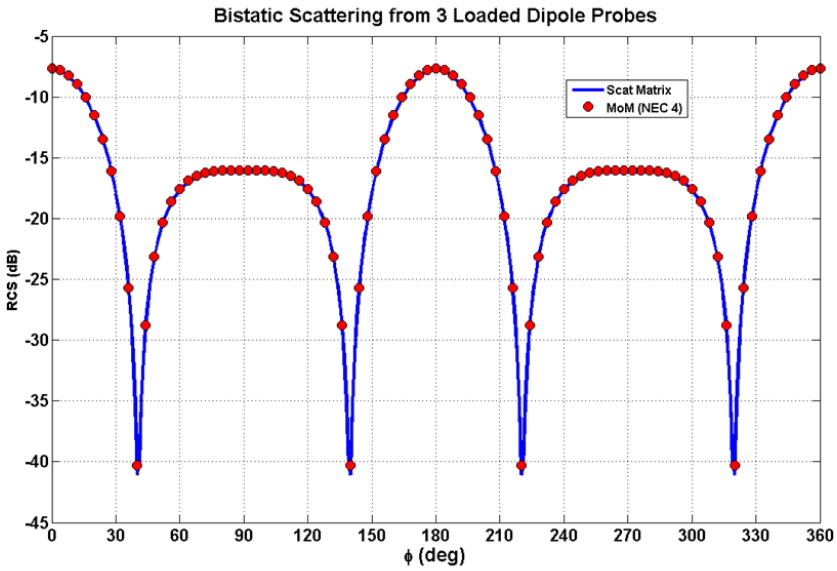

Figure 6: Comparison of the FF Scattering Patterns from Three Loaded Dipoles

Comparison of (17) and (16) with (13) yields

$$\hat{\mathbf{\Gamma}}_{ar} = \mathbf{\Gamma}_{ar} + \mathbf{R}_{ar}\left[\mathbf{T}_{ar}\mathbf{a}_{ar}^{(+)} + \mathbf{S}_{ar}\tau_{\oplus}\mathbf{b}_{tg}^{(-)}\right]\left[\mathbf{I} - \mathbf{S}_{ar}\left(\tau_{\oplus}\mathbf{T}_{tg}\tau_{\ominus} + \tau_{ar}\right)\right]^{-1}\mathbf{T}_{ar} \quad (18)$$

$$\hat{\mathbf{R}}_{ar} = \mathbf{R}_{ar} + \mathbf{R}_{ar}\left[\mathbf{T}_{ar}\mathbf{a}_{ar}^{(+)} + \mathbf{S}_{ar}\tau_{\oplus}\bar{b}_{tg}^{(-)}\right]\left[\mathbf{I} - \mathbf{S}_{ar}\left(\tau_{\oplus}\mathbf{T}_{tg}\tau_{\ominus} + \tau_{ar}\right)\right]^{-1}\mathbf{S}_{ar} \quad (19)$$

$$\hat{\mathbf{T}}_{ar} = \left[\mathbf{I} - \mathbf{S}_{ar}\left(\tau_{\oplus}\mathbf{T}_{tg}\tau_{\ominus} + \tau_{ar}\right)\right]^{-1}\mathbf{T}_{ar} \quad (20)$$

$$\hat{\mathbf{S}}_{ar} = \left[\mathbf{I} - \mathbf{S}_{ar}\left(\tau_{\oplus}\mathbf{T}_{tg}\tau_{\ominus} + \tau_{ar}\right)\right]^{-1}\mathbf{S}_{ar} \quad (21)$$

We note that similar results were obtained in [28] for the case of an isolated array (i.e., no target present). We also note that in the absence of the target $\tau_{\oplus}\mathbf{T}_{tg}\tau_{\ominus} = 0$, and (13) – (21) reduce to the corresponding relations presented in [28]. We may regard the equations discussed above as an extension to the case where the incident plane wave scatters off from a target and the resulting scattered field sets off multiple scattering between the target and the array.

Shown in Figure 6 is the comparison of the FF pattern computed using the formalism presented above with the NEC-4 [21] result for the scattering from three loaded dipoles shown in Figure 7. The dipole antenna scattering matrix was computed using the extraction technique discussed in [14]. The agreement between the two curves is excellent.

2.5 Multiple Scattering Reduction

In this subsection, we compute the extent of the multiple scattering between a DUT and a probe array using the formulation developed above. We consider a bistatic application with a PEC sphere as a DUT since its reference FF solution and $\mathbf{T}_{tg}$ can readily be computed using the Mie series. Consider the planar near-field scanning scenario shown in Figure 8. A vertically polarized plane wave propagating in the y direction is scattered by a 1λ sphere and the scattered field is collected at $(x, y, z) = (0.5i\lambda, 7.5\lambda, 0.5k\lambda)$ with $i = -20, ..., 20$ and $k = -20, ..., 20$. Thus a total of 1681 NF samples are collected on a $20\lambda \times 20\lambda$ planar scan surface. Also shown in the figure is a vertical linear probe array with 41 probe elements that

Approved for public release; distribution is unlimited.

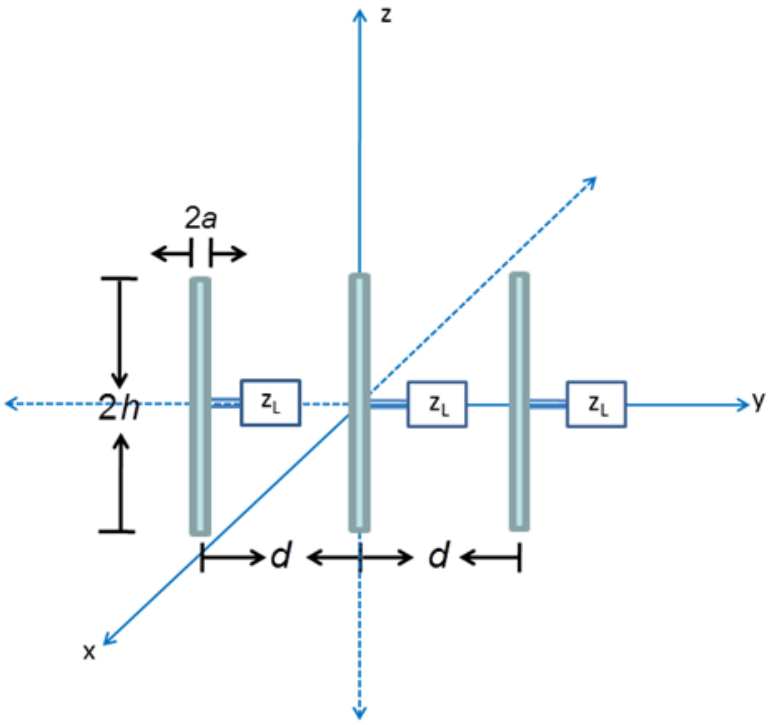

Figure 7: Three Loaded Dipoles with $h = 0.475\lambda$, $d = 0.5\lambda$, $a = 0.001\lambda$

Approved for public release; distribution is unlimited.

are separated by 0.5λ. The dipole probes are 0.475λ long and have a 0.001λ radius. The array simultaneously collects the scattered fields at all the vertical scan positions, $z_k = k0.5\lambda, k = -20, ..., 20$ at a given x_i, and then mechanically moves to the next location, x_{i+1} and collects the NF samples at all z_k at once. The process is repeated until the array covers all the x_i positions. The MS between the sphere and the array is expected to be the strongest when the distance between the array and the sphere is minimum. In addition, the the sphere is expected to scatter most strongly in the forward direction. Therefore, we expect the strongest MS when the array is at $x_i = 0$.

We solve the multiple-scattering equations presented above for the case when the array is located at $x_i = 0$ to examine the extent of the maximum MS. First, we assume that the 41 probes in the array are all short circuited. We determine the antenna-scattering matrix for the short-circuited probe, and we solve the multiple-scattering equations with the antenna-scattering matrix as an input. Compared with the Mie solution in Figure 9 is the FF computed from the sphere's outgoing expansion coefficients, $\hat{\mathbf{b}}_{tg}^{(-)}$, in the presence of the array whose 41 probe elements are all assumed to be short circuited. As evident from the figure, the MS has perturbed the induced current strongly enough to produce a FF that deviates noticeably from the Mie solution. This underscores the need to reduce the MS effects.

In order to reduce the MS effects, we reactively load the 41 probe elements in the array. Again, we determine the antenna-scattering matrix for the loaded probe. Using it as an input, we solve the multiple-scattering equations for the outgoing expansion coefficients, $\hat{\mathbf{b}}_{tg}^{(-)}$, of the sphere in the presence of the loaded probe array. Compared with the Mie series in Figure 9 is the FF generated using the computed $\hat{\mathbf{b}}_{tg}^{(-)}$. As evident from the figure, the FF generated using the $\hat{\mathbf{b}}_{tg}^{(-)}$ agrees well with the Mie solution, indicating that the MS effects are now much reduced. This demonstrates the theoretical feasibility of impedance loading approaches in reducing MS effects.

2.6 Summary

The antenna pattern and bistatic target RCS are both FF properties associated with an antenna and a target. NF techniques allow these quantities to be determined from field samples collected near a DUT. However, as the electrical size of a DUT increases, so is the required Nyquist NF spatial sampling rate. Since the NF sample collection time is, to first order, proportional to the square of the sampling rate, it can be time consuming for a single probe to collect all the required NF samples. One way of reducing the NF collection time is to use an array of probes [4], and simultaneously sample the NF over a portion of a scan surface. In NF scanning with a single probe, the MS between a DUT and the probe is small and thus ignored. However, in NF scanning with a multi-probe array, the total size of the measurement aperture increases significantly. As a result, there could be strong MS between a DUT and the probe array. The MS perturbs the current distribution induced on a DUT from that induced by a primary source and produces errors in the reconstructed FF. In addition, there could be MC between the probes in the array. If uncompensated, the MC also produces errors in the FF. Furthermore, it has been shown that when the MS is strong, the MC changes as the orientation of the probe array varies with respect to the DUT [5], requiring a complicated MC-compensation technique. Thus, an effective MS-reduction technique may lead to a less complicated MC-compensation technique.

It is well known that impedance loading changes the scattering characteristics of an object [7]. We have explicitly shown in Figure 5 that it is possible to reduce the total scattered energy of an isolated dipole by reactively loading it, and thereby correspondingly reducing its MS effects. In order to investigate the extent of MS reduction achievable by the impedance loading approach in NF scanning, we have cast the MS between a DUT and a probe array and the MC between the probes as a multiple-scattering problem using the formalism of [9]. A key input to this formalism is the antenna-scattering matrix of a probe, which accounts for its absorption, radiation, transmission, and scattering characteristics. We have extracted its value for a loaded dipole, and used it as an input to the multiple-scattering problem for planar NF scanning for a bistatic RCS application, as depicted in Figure 8. Our numerical results have shown that

Approved for public release; distribution is unlimited.

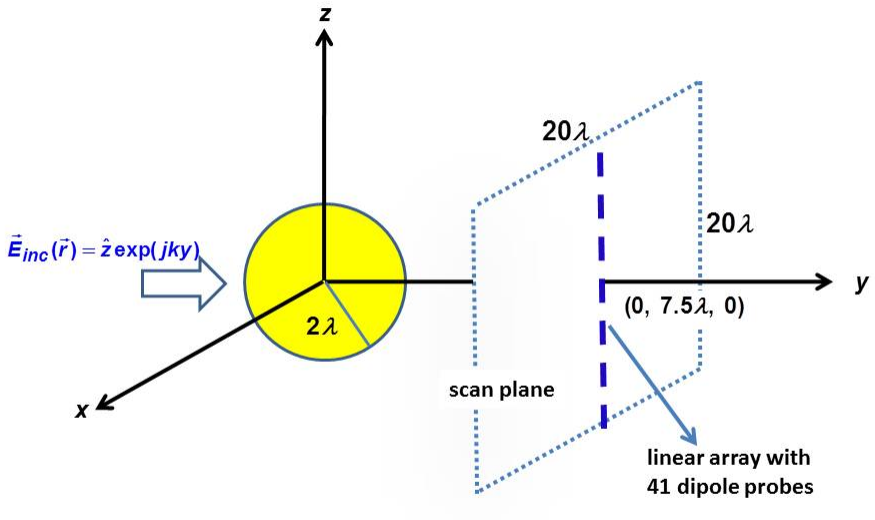

Figure 8: Planar Scanning of a 1λ Radius PEC Sphere

when all the probes in the array were assumed to be short-circuited, the MS-generated perturbation of the induced current on the sphere was strong enough to produce large errors in the FF. However, when the probes in the array were reactively loaded, the current perturbation was small enough and the computed FF agreed well with the Mie reference solution. Thus, we have shown that it is theoretically possible to reduce the MS between a DUT and a probe array using the impedance loading technique.

It is well known that a probe that scatters less energy also absorbs less energy [16][17], leading to a correspondingly low SNR. We have suggested that it may be possible to boost the SNR to an acceptable level by using the coherent integration technique by taking advantage of the fact that the electromagnetic environment in an anechoic chamber remains stable for a long period of time. Thus, NF scanning with a probe array may offer a higher NF sampling efficiency than the traditional single-probe NF scanning when the coherent integration time is less than the time for the single probe to mechanically transverse the length of the array.

Approved for public release; distribution is unlimited.

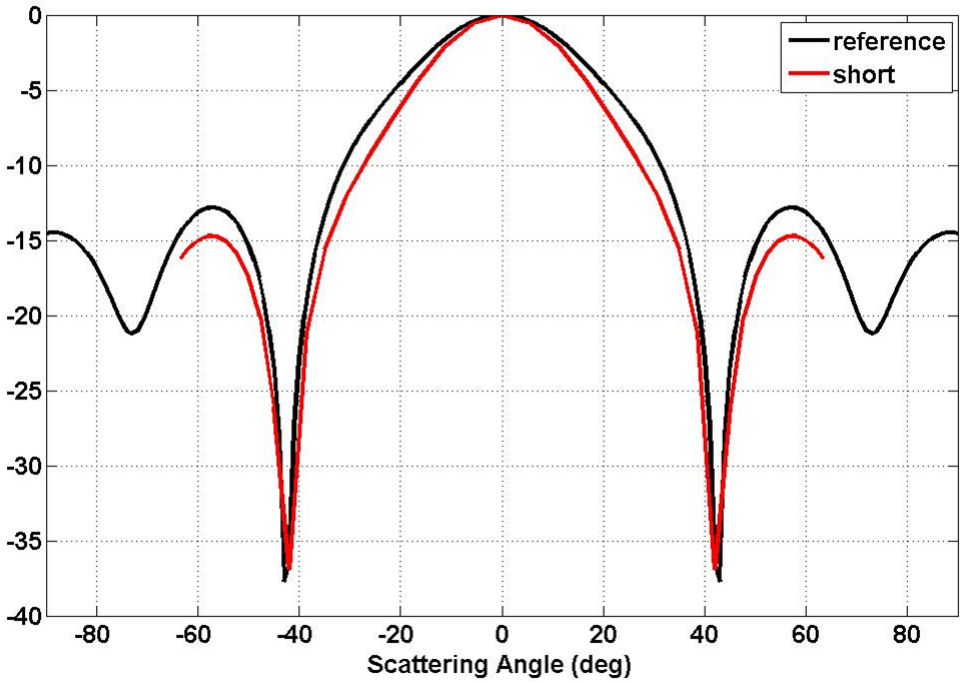

Figure 9: Comparison of the FF with the Mie Solution: the Probes are Assumed to be Shorted

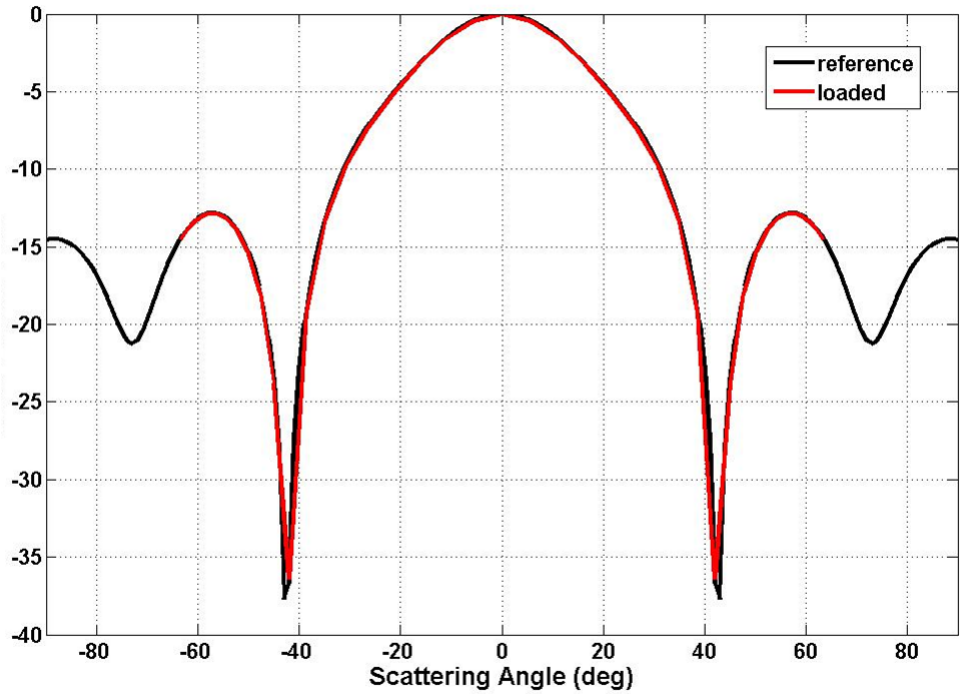

Figure 10: Comparison of the FF with the Mie Solution: the Probes Are Assumes to be Loaded

Approved for public release; distribution is unlimited.

3 Performance of Modulated Scatterer Array

3.1 Introduction

We have studied an approach to reduce the time required for near field scattering measurements by using an array of near field probes to replace the single probe that is conventionally used [5][29]. Coupling between the larger probe array and the scattering body introduces errors in the near field measurements by perturbing the plane wave induced currents on the body. Also, mutual coupling between the probe array elements in the presence of the scattering body may change the near field measured at each probe array element from that measured by an isolated probe.

Using an impedance model to describe the interactions between the elements of the probe array and the scattering body, we developed expressions for the measured voltages at each of the transmission line feeds to the probe array elements in terms of (1) the open circuit voltages induced by the plane wave excited body at each probe array element and (2) the in-situ mutual impedances of the probe array [5][29]. These in-situ mutual impedances are measured at the array ports with the scattering target present. The expressions showed linear relations between the measured voltages and the open circuit voltages as would be expected by the superposition principle. These equations can be inverted to yield the open circuit, plane wave induced voltages at each probe array element. We also described a separate set of vector network analyzer measurements to yield the in-situ mutual impedances that are required to invert the measurement equations.

In theory, minimizing the probe array-target interactions requires measurement of the in-situ mutual impedances of the probe array. In general these measurements would be required for each location and orientation of the probe array with respect to the scattering target. However, repeated in-situ impedance measurements will slow the overall measurement process and degrade the promised measurement efficiency of the probe array. In a second study [29] we evaluated the feasibility of using the free space mutual impedances of the array in place of the in-situ impedances to derive the open circuit voltages and minimize the array-target interactions. The free space impedances would be measured only once, thereby increasing the efficiency of the overall measurement process. To assess the requirement for measurements of in-situ mutual impedances, we considered a probe array with strong interaction between the target and the array. Specifically we considered a surrogate flat plate with a five element dipole probe array located near the plate and in the direction of the specular, plane wave induced scattering from the plate. We investigated the perturbations on the plane wave induced currents on the plate due to the presence of the loaded, five element dipole probe array. Numerical results using NEC4 indicated that active loading of the probe array is required to minimize the perturbations in the target currents. However, we found in this case that there is little advantage to using in-situ mutual impedances in determining the active loads.

However, this is not the complete story. The coupling between the array and the target under test can introduce errors in the measured voltages at the probe array elements. These errors are due to (a) the assumption that there is no target-array coupling in interpreting the measurements, (b) calibration of the probe array in free space where there is no interaction with the target and (c) failure to achieve adequate current cancellation in the probe array elements during measurements of the open circuit voltages at the array elements. To address these additional sources of error, we provided a probe array compensation theory based on the Lorentz reciprocity theorem [29]. The theory permits expression of the open circuit probe array voltages in terms of (a) the required surface integral involving the near fields scattered by the target and the near fields radiated by the probe array with no target-array interaction and (b) correction voltages due to the presence of the array elements and the target-array interactions. The correction voltages are of two types. One type is due to perturbations in the target scattered field because of the presence of the probe array. This correction voltage is unknown and not available for compensation of the measured voltage at the probe array. Another type of correction voltage is associated with plane wave induced currents on the probe array when located in free space. These correction voltages can be developed as part of the probe array calibration and measurements of the incident plane wave. A numerical study of

Approved for public release; distribution is unlimited.

the surrogate flat plate-probe array configuration indicated that (a) corrections to the measured probe array voltages due to perturbations in the scattered field from the presence of the probe array are small, even when cancellation of the probe array currents is determined using the free space mutual impedances of the array, and (b) corrections due to the presence of the other elements of the probe array can be important but the corrections can be determined in terms of the free space current distributions on the array as part of the array calibration process.

In addition, errors in the probe array voltage measurements are introduced by the use of realizable sources in the probe array during calibration and realizable loads during scattering measurements. When the array is calibrated in free space and used to cancel the array currents during near field measurements, errors in the open circuit voltages as large as -12.5 dB were observed for the plate-array problem analyzed here. These measurement errors are most significant for the array elements that are close to the target under test. Experimental errors in achieving probe array current cancellation cause errors in the voltage measurements as well. In fact, these errors are increased due to calibration of the probe array in free space by as much as 13 dB for the plate-array problem considered here.

These conclusions are potentially significant since they seem to indicate that free space mutual impedances of the probe array are sufficient for the simultaneous measurement of near scattered field samples with small error so long as elements of the array are not too close to the target under test. The effective use of free space mutual impedances obviates the need for in-situ impedance measurements at each location and orientation of the probe array with respect to the scattering body which would slow the overall measurement process. It would seem that a hybrid measurement process should be considered. For probe array locations and orientations with respect to the target when there is likely to be large coupling, in-situ mutual impedances would be required, slowing the measurement process. When little coupling is anticipated, the free space mutual impedances of the array can be used, thereby speeding the measurement process.

In this paper we turn to an analysis of the modulated scatterer (MS) technique applied to a probe array. In the modulated scatterer technique [18], the amplitude and phase of an electromagnetic field component are measured by placing a small, polarization sensitive probe at the field position. The field scattered by the probe is modulated by changing the load impedance of the probe. The modulated signal, dependent on the required field sample, is coherently detected at a remote location to minimize the interaction of the detector with the target to be measured. The low frequency modulation signal is fed to the probe via communications lines that minimize the perturbation of the field components to be measured. The lines might be optical fibers or high resistance wires.

Here we consider a probe array where the active loads of the array are modulated for purposes of measuring the open circuit voltages excited in the array elements by the target scattered field. Within the context of our earlier studies, changing the load on one element of the probe array will have the secondary effects of (1) changing the currents on the scattering body and (2) changing the open circuit conditions on the other elements of the probe array due to the in-situ coupling between the array elements. Also, as we shall see, the field scattered by the probe array consists of a linear superposition of open circuit voltages on the probe array elements and not just the open circuit voltage of the modulated element. This is due to the mutual coupling between the elements of the probe array. Thus, application of the modulated scatterer technique to a probe array introduces errors in the measurements of the fields scattered by the target due to mutual coupling between elements of the probe array. The objective of this study is to quantify the additional field errors due to the modulated scatterer technique as a function of the modulated signal strength and the effects of the array-target coupling.

In the next section we develop expressions for the modulated signal at the measurement probe using an active, in-situ mutual impedance model for the array and measurement probe. This model was developed previously [5].

3.2 Modulated Probe Array Model

In this section we model the modulated signal at the measurement probe using an active, in-situ mutual impedance representation relating the currents and voltages at the terminals of probe array elements and the measurement probe. The measurement probe is remotely located with the primary function of observing the modulated signals created by changing the load impedances or sources at the terminals of the probe array elements. The in-situ mutual impedances are required since we wish to limit current perturbations on the scattering body and the in-situ impedances characterize the interaction between the array and the scattering body. The representation is active to include the open circuit voltages induced at each probe array terminal by the plane wave excitation and target scattering. The linear in-situ impedance relationships between the open circuit voltages at the terminals of the probe array elements, E_i^p, $i = 1, 2, 3$, and the open circuit voltage at the measurement probe, E^m, are given by [5]

$$\begin{bmatrix} E_1^p \\ E_2^p \\ E_3^p \\ E^m \end{bmatrix} = \begin{bmatrix} E_1^{p_o} \\ E_2^{p_o} \\ E_3^{p_o} \\ E^{m_o} \end{bmatrix} + \begin{bmatrix} \widetilde{Z}_{1,1} & \widetilde{Z}_{1,2} & \widetilde{Z}_{1,3} & \widetilde{Z}_{1,m} \\ \widetilde{Z}_{2,1} & \widetilde{Z}_{2,2} & \widetilde{Z}_{2,3} & \widetilde{Z}_{2,m} \\ \widetilde{Z}_{3,1} & \widetilde{Z}_{3,2} & \widetilde{Z}_{3,3} & \widetilde{Z}_{3,m} \\ \widetilde{Z}_{m,1} & \widetilde{Z}_{m,2} & \widetilde{Z}_{m,3} & \widetilde{Z}_{m,m} \end{bmatrix} \begin{bmatrix} I_1 \\ I_2 \\ I_3 \\ I_m \end{bmatrix}. \tag{22}$$

In this analysis, we consider a three element probe array. The extension of the analysis to larger arrays will be obvious. In equation (22), $E_i^{p_o}$, $i = 1, 2, 3$, represent the open circuit voltages induced at each probe array terminal due to the plane wave excitation of the array and the scattering from the target. In like manner, E^{m_o} represents the open circuit voltage introduced in the measurement probe by the plane wave, the target scattering and the scattering by the probe array. Also, I_i, $i = 1, 2, 3$ and I_m represent the currents entering the probe array and measurement probe terminals, respectively. The in-situ mutual impedances, $\widetilde{Z}_{i,j}$ relate the open circuit voltages at terminal i induced by the current at terminal j with the other terminals open circuited, observed with the scattering target present and no plane wave excitation.

Applying a Thévenin equivalent source to each probe array terminal and a load Z_m at the measurement probe gives

$$\begin{bmatrix} E_1^{Th} - Z_1^{Th} I_1 \\ E_2^{Th} - Z_2^{Th} I_2 \\ E_3^{Th} - Z_3^{Th} I_3 \\ E^m \end{bmatrix} = \begin{bmatrix} E_1^{p_o} \\ E_2^{p_o} \\ E_3^{p_o} \\ E^{m_o} \end{bmatrix} + \begin{bmatrix} \widetilde{Z}_{1,1} & \widetilde{Z}_{1,2} & \widetilde{Z}_{1,3} & \widetilde{Z}_{1,m} \\ \widetilde{Z}_{2,1} & \widetilde{Z}_{2,2} & \widetilde{Z}_{2,3} & \widetilde{Z}_{2,m} \\ \widetilde{Z}_{3,1} & \widetilde{Z}_{3,2} & \widetilde{Z}_{3,3} & \widetilde{Z}_{3,m} \\ \widetilde{Z}_{m,1} & \widetilde{Z}_{m,2} & \widetilde{Z}_{m,3} & \widetilde{Z}_{m,m} \end{bmatrix} \begin{bmatrix} I_1 \\ I_2 \\ I_3 \\ \frac{-E^m}{Z_m} \end{bmatrix}. \tag{23}$$

Here E_i^{Th}, $i = 1, 2, 3$ are the open circuit voltages of the Thévenin sources and Z_i^{Th}, $i = 1, 2, 3$ are the Thévenin equivalent impedances. We can rewrite Equation (23) as

$$\begin{bmatrix} E_1^{Th} - E_1^{p_o} \\ E_2^{Th} - E_2^{p_o} \\ E_3^{Th} - E_3^{p_o} \\ E^m \end{bmatrix} = \begin{bmatrix} 0 \\ 0 \\ 0 \\ E^{m_o} \end{bmatrix} + \begin{bmatrix} \widetilde{Z}_{1,1} + Z_1^{Th} & \widetilde{Z}_{1,2} & \widetilde{Z}_{1,3} & \widetilde{Z}_{1,m} \\ \widetilde{Z}_{2,1} & \widetilde{Z}_{2,2} + Z_2^{Th} & \widetilde{Z}_{2,3} & \widetilde{Z}_{2,m} \\ \widetilde{Z}_{3,1} & \widetilde{Z}_{3,2} & \widetilde{Z}_{3,3} + Z_3^{Th} & \widetilde{Z}_{3,m} \\ \widetilde{Z}_{m,1} & \widetilde{Z}_{m,2} & \widetilde{Z}_{m,3} & \widetilde{Z}_{m,m} \end{bmatrix} \begin{bmatrix} I_1 \\ I_2 \\ I_3 \\ \frac{-E^m}{Z_m} \end{bmatrix}.$$

From the last equation

$$E^m(1 + \frac{\widetilde{Z}_{m,m}}{Z_m}) = E^{m_o} + \begin{bmatrix} \widetilde{Z}_{m,1} & \widetilde{Z}_{m,2} & \widetilde{Z}_{m,3} \end{bmatrix} \begin{bmatrix} I_1 \\ I_2 \\ I_3 \end{bmatrix},$$

and solving for the probe array currents, assuming that they are principally found from the array-target interaction matrix, we find

$$\begin{bmatrix} E_1^{Th} - E_1^{p_o} \\ E_2^{Th} - E_2^{p_o} \\ E_3^{Th} - E_3^{p_o} \end{bmatrix} \equiv \begin{bmatrix} \delta E_1 \\ \delta E_2 \\ \delta E_3 \end{bmatrix} = \begin{bmatrix} \widetilde{Z}_{1,1} + Z_1^{Th} & \widetilde{Z}_{1,2} & \widetilde{Z}_{1,3} \\ \widetilde{Z}_{2,1} & \widetilde{Z}_{2,2} + Z_2^{Th} & \widetilde{Z}_{2,3} \\ \widetilde{Z}_{3,1} & \widetilde{Z}_{3,2} & \widetilde{Z}_{3,3} + Z_3^{Th} \end{bmatrix} \begin{bmatrix} I_1 \\ I_2 \\ I_3 \end{bmatrix},$$

Approved for public release; distribution is unlimited.

or

$$\left[\begin{array}{c} I_1 \\ I_2 \\ I_3 \end{array}\right] = \left[\begin{array}{ccc} \widetilde{Z}_{1,1}+Z_1^{Th} & \widetilde{Z}_{1,2} & \widetilde{Z}_{1,3} \\ \widetilde{Z}_{2,1} & \widetilde{Z}_{2,2}+Z_2^{Th} & \widetilde{Z}_{2,3} \\ \widetilde{Z}_{3,1} & \widetilde{Z}_{3,2} & \widetilde{Z}_{3,3}+Z_3^{Th} \end{array}\right]^{-1} \left[\begin{array}{c} \delta E_1 \\ \delta E_2 \\ \delta E_3 \end{array}\right].$$

It follows that

$$E^m(1+\frac{\widetilde{Z}_{m,m}}{Z_m}) = E^{m_o} + \left[\begin{array}{ccc} \widetilde{Z}_{m,1} & \widetilde{Z}_{m,2} & \widetilde{Z}_{m,3} \end{array}\right] \left[\begin{array}{ccc} \widetilde{Z}_{1,1}+Z_1^{Th} & \widetilde{Z}_{1,2} & \widetilde{Z}_{1,3} \\ \widetilde{Z}_{2,1} & \widetilde{Z}_{2,2}+Z_2^{Th} & \widetilde{Z}_{2,3} \\ \widetilde{Z}_{3,1} & \widetilde{Z}_{3,2} & \widetilde{Z}_{3,3}+Z_3^{Th} \end{array}\right]^{-1} \left[\begin{array}{c} \delta E_1 \\ \delta E_2 \\ \delta E_3 \end{array}\right]. \tag{24}$$

In general, the modulated scatterer technique using active, Thévenin equivalent loads can be implemented in either of two ways. In one approach, the Thévenin voltage, E_i^{Th}, can be selected to vary about the open circuit voltage induced in the ith probe array port. That is,

$$E_i^{Th} = E_i^{p_o} + \delta E_i,$$

with $|\delta E_i| \ll |E_i^{p_o}|$ and $\delta E_j = 0,\ j \neq i$. These conditions are required so that the currents at each probe array terminal are small, minimizing the perturbation in target currents due to scattering from the probe array. However, this approach requires a variable, active load or source at each element of the probe array that can be adaptively adjusted to cancel the open circuit voltage at each terminal. This could require a potentially large feed and control structure for the probe array which, in turn, may introduce a large perturbation in the scattered field to be measured by the array. Further, the magnitude and phase of the cancellation voltage as it approximates the induced open circuit voltage, $E_i^{p_o}$, could be transmitted from the probe array to a data recorder, obviating the need for the modulated scattering technique.

A second approach to implementing the modulated scatterer technique is to use passive Thévenin equivalent loads such that $E_i^{Th} = 0, \forall i$, with large Thévenin equivalent load impedances, Z_i^{Th}. The large load impedances are used to achieve nearly open circuit conditions at all terminals of the probe array. One load impedance is varied to achieve the modulated scattering from the probe array. This approach conforms with the conventional notion of the modulated scatterer technique and will be analyzed in the following. For this approach, Equation (24) becomes

$$E^m(1+\frac{\widetilde{Z}_{m,m}}{Z_m}) = E^{m_o} - \left[\begin{array}{ccc} \widetilde{Z}_{m,1} & \widetilde{Z}_{m,2} & \widetilde{Z}_{m,3} \end{array}\right] \left[\begin{array}{ccc} \widetilde{Z}_{1,1}+Z_1^{Th} & \widetilde{Z}_{1,2} & \widetilde{Z}_{1,3} \\ \widetilde{Z}_{2,1} & \widetilde{Z}_{2,2}+Z_2^{Th} & \widetilde{Z}_{2,3} \\ \widetilde{Z}_{3,1} & \widetilde{Z}_{3,2} & \widetilde{Z}_{3,3}+Z_3^{Th} \end{array}\right]^{-1} \left[\begin{array}{c} E_1^{p_o} \\ E_2^{p_o} \\ E_3^{p_o} \end{array}\right]. \tag{25}$$

If the load impedances are large compared to the in-situ self and mutual impedances of the probe array, then

$$\begin{aligned} E^m(1+\tfrac{\widetilde{Z}_{m,m}}{Z_m}) &\cong E^{m_o} - \left[\begin{array}{ccc} \widetilde{Z}_{m,1} & \widetilde{Z}_{m,2} & \widetilde{Z}_{m,3} \end{array}\right] \left[\begin{array}{ccc} Z_1^{Th} & 0 & 0 \\ 0 & Z_2^{Th} & 0 \\ 0 & 0 & Z_3^{Th} \end{array}\right]^{-1} \left[\begin{array}{c} E_1^{p_o} \\ E_2^{p_o} \\ E_3^{p_o} \end{array}\right] \\ &\cong E^{m_o} - \left[\begin{array}{ccc} \widetilde{Z}_{m,1} & \widetilde{Z}_{m,2} & \widetilde{Z}_{m,3} \end{array}\right] \left[\begin{array}{ccc} \frac{1}{Z_1^{Th}} & 0 & 0 \\ 0 & \frac{1}{Z_2^{Th}} & 0 \\ 0 & 0 & \frac{1}{Z_3^{Th}} \end{array}\right] \left[\begin{array}{c} E_1^{p_o} \\ E_2^{p_o} \\ E_3^{p_o} \end{array}\right] \\ &\cong E^{m_o} - \tfrac{\widetilde{Z}_{m,1}}{Z_1^{Th}} E_1^{p_o} - \tfrac{\widetilde{Z}_{m,2}}{Z_2^{Th}} E_2^{p_o} - \tfrac{\widetilde{Z}_{m,3}}{Z_3^{Th}} E_3^{p_o}. \end{aligned}$$

To this approximation, it is clear that varying any Thévenin load impedance with time introduces a time modulation of the voltage observed in the measurement dipole which is proportional to the open circuit

Approved for public release; distribution is unlimited.

voltage, $E_i^{p_o}$, induced in the probe array terminal with the time varing load. That is, if for example, $Z_2^{Th} = Z_2^{Th}(t)$ then

$$E^m(t)(1+\frac{\widetilde{Z}_{m,m}}{Z_m}) \cong E^{m_o} - \frac{\widetilde{Z}_{m,1}}{Z_1^{Th}}E_1^{p_o} - \frac{\widetilde{Z}_{m,2}}{Z_2^{Th}(t)}E_2^{p_o} - \frac{\widetilde{Z}_{m,3}}{Z_3^{Th}}E_3^{p_o}, \tag{26}$$

which yields a time varying voltage in the measurement dipole which is proportional, after calibration, to the open circuit voltage at terminal two, $E_2^{p_o}$. Here the calibration factor for impedance changes at probe terminal 2 is given by $\frac{\widetilde{Z}_{m,2}}{Z_2^{Th}(t)(1+\frac{\widetilde{Z}_{m,m}}{Z_m})}$. Note that calibration may be required at each probe array postion with respect to the target if the in-situ probe array element to measurement probe mutual impedance, $\widetilde{Z}_{m,2}$, changes with probe array position.

Equation (26) may be misleading, however. Any change in the Thévenin load impedance at one probe array terminal produces a change in the voltages and currents at the other array terminals which, in turn, introduces coupling from the other probe array terminal voltages to the measurement voltage. Further, changes in the terminal voltages and currents from their nominal open circuit conditions causes perturbations in the currents on the scattering body. Thus, it is important to minimize the changes in the Thévenin load impedance at the probe array terminal to be measured while still insuring that changes in the measurement voltage, $E^m(t)$ are (a) sufficiently large when compared to noise at the measurement probe and (b) essentially proportional to the open circuit voltage induced in the terminal by the scattering process.

To obtain a quantitative estimate of the impact of the coupling that occurs with changes in the Thévenin load impedance, we consider an approximate expansion of the matrix inverse in Equation (25) as developed in the following:

$$\begin{aligned} E^m(1+\tfrac{\widetilde{Z}_{m,m}}{Z_m}) &= E^{m_o} - \begin{bmatrix} \widetilde{Z}_{m,1} & \widetilde{Z}_{m,2} & \widetilde{Z}_{m,3} \end{bmatrix} \begin{bmatrix} \widetilde{Z}_{1,1}+Z_1^{Th} & \widetilde{Z}_{1,2} & \widetilde{Z}_{1,3} \\ \widetilde{Z}_{2,1} & \widetilde{Z}_{2,2}+Z_2^{Th} & \widetilde{Z}_{2,3} \\ \widetilde{Z}_{3,1} & \widetilde{Z}_{3,2} & \widetilde{Z}_{3,3}+Z_3^{Th} \end{bmatrix}^{-1} \begin{bmatrix} E_1^{p_o} \\ E_2^{p_o} \\ E_3^{p_o} \end{bmatrix} \\ &\cong E^{m_o} - \begin{bmatrix} \widetilde{Z}_{m,1} & \widetilde{Z}_{m,2} & \widetilde{Z}_{m,3} \end{bmatrix} \begin{bmatrix} \widetilde{Z}_{1,1}+Z_1^{Th} & \widetilde{Z}_{1,2} & \widetilde{Z}_{1,3} \\ \widetilde{Z}_{2,1} & Z_2^{Th} & \widetilde{Z}_{2,3} \\ \widetilde{Z}_{3,1} & \widetilde{Z}_{3,2} & Z_3^{Th} \end{bmatrix}^{-1} \begin{bmatrix} E_1^{p_o} \\ E_2^{p_o} \\ E_3^{p_o} \end{bmatrix} \end{aligned} \tag{27}$$

where we assume here that the terminal one impedance, Z_1^{Th} will be modulated and the load impedances at the other terminals, Z_2^{Th} and Z_3^{Th}, are large compared to the comparable internal impedances, $\widetilde{Z}_{2,2}$ and $\widetilde{Z}_{3,3}$ respectively, due to the near open circuit conditions required at these terminals. Then we can write

$$E^m(1+\frac{\widetilde{Z}_{m,m}}{Z_m}) \cong E^{m_o} - \begin{bmatrix} \widetilde{H}_{m,1} & \widetilde{H}_{m,2} & \widetilde{H}_{m,3} \end{bmatrix} \begin{bmatrix} E_1^{p_o} \\ E_2^{p_o} \\ E_3^{p_o} \end{bmatrix},$$

where $\widetilde{H}_{m,i}$, $i = 1, 2, 3$ represent the voltage transfer function between the open circuit voltage at terminal i and the voltage at the measurement probe. That is,

$$\widetilde{H}_{m,i} = -\frac{E^m(1+\frac{\widetilde{Z}_{m,m}}{Z_m}) - E^{m_o}}{E_i^{p_o}}\bigg|_{E_j^{p_o}=0,\, j\neq i},$$

and is found from expansion of the matrix product

$$\begin{bmatrix} \widetilde{Z}_{m,1} & \widetilde{Z}_{m,2} & \widetilde{Z}_{m,3} \end{bmatrix} \begin{bmatrix} \widetilde{Z}_{1,1}+Z_1^{Th} & \widetilde{Z}_{1,2} & \widetilde{Z}_{1,3} \\ \widetilde{Z}_{2,1} & Z_2^{Th} & \widetilde{Z}_{2,3} \\ \widetilde{Z}_{3,1} & \widetilde{Z}_{3,2} & Z_3^{Th} \end{bmatrix}^{-1}.$$

Approved for public release; distribution is unlimited.

Expanding this matrix product gives

$$\widetilde{H}_{m,1} = \frac{\widetilde{Z}_{m,1} - \frac{\widetilde{Z}_{2,1}\widetilde{Z}_{m,2}}{Z_2^{Th}} - \frac{\widetilde{Z}_{3,1}\widetilde{Z}_{m,3}}{Z_3^{Th}} + \frac{\widetilde{Z}_{2,1}\widetilde{Z}_{3,2}\widetilde{Z}_{m,3}+\widetilde{Z}_{3,1}\widetilde{Z}_{2,3}\widetilde{Z}_{m,2}-\widetilde{Z}_{2,3}\widetilde{Z}_{3,2}\widetilde{Z}_{m,1}}{Z_2^{Th}Z_3^{Th}}}{\widetilde{Z}_{1,1} + Z_1^{Th} - \frac{\widetilde{Z}_{2,1}\widetilde{Z}_{1,2}}{Z_2^{Th}} - \frac{\widetilde{Z}_{3,1}\widetilde{Z}_{1,3}}{Z_3^{Th}} + \frac{\widetilde{Z}_{1,2}\widetilde{Z}_{3,1}\widetilde{Z}_{2,3}+\widetilde{Z}_{2,1}\widetilde{Z}_{1,3}\widetilde{Z}_{3,2}-\widetilde{Z}_{1,1}\widetilde{Z}_{2,3}\widetilde{Z}_{3,2}-\widetilde{Z}_{2,3}\widetilde{Z}_{3,2}Z_1^{Th}}{Z_2^{Th}Z_3^{Th}}}, \tag{28}$$

$$\widetilde{H}_{m,2} = \frac{\frac{\widetilde{Z}_{1,1}\widetilde{Z}_{m,2}-\widetilde{Z}_{1,2}\widetilde{Z}_{m,1}-Z_1^{Th}\widetilde{Z}_{m,2}}{Z_2^{Th}} + \frac{(\widetilde{Z}_{1,2}\widetilde{Z}_{3,1}-Z_{3,2}Z_1^{Th}-Z_{1,1}Z_{3,2})\widetilde{Z}_{m,3}-\widetilde{Z}_{3,1}\widetilde{Z}_{1,3}\widetilde{Z}_{m,2}+\widetilde{Z}_{1,3}\widetilde{Z}_{3,2}\widetilde{Z}_{m,1}}{Z_2^{Th}Z_3^{Th}}}{\widetilde{Z}_{1,1} + Z_1^{Th} - \frac{\widetilde{Z}_{2,1}\widetilde{Z}_{1,2}}{Z_2^{Th}} - \frac{\widetilde{Z}_{3,1}\widetilde{Z}_{1,3}}{Z_3^{Th}} + \frac{\widetilde{Z}_{1,2}\widetilde{Z}_{3,1}\widetilde{Z}_{2,3}+\widetilde{Z}_{2,1}\widetilde{Z}_{1,3}\widetilde{Z}_{3,2}-\widetilde{Z}_{1,1}\widetilde{Z}_{2,3}\widetilde{Z}_{3,2}-\widetilde{Z}_{2,3}\widetilde{Z}_{3,2}Z_1^{Th}}{Z_2^{Th}Z_3^{Th}}}, \tag{29}$$

and

$$\widetilde{H}_{m,3} = \frac{\frac{\widetilde{Z}_{1,1}\widetilde{Z}_{m,3}-\widetilde{Z}_{1,3}\widetilde{Z}_{m,1}-Z_1^{Th}\widetilde{Z}_{m,3}}{Z_3^{Th}} + \frac{(\widetilde{Z}_{2,1}\widetilde{Z}_{1,3}-Z_{2,3}Z_1^{Th}-Z_{1,1}Z_{2,3})\widetilde{Z}_{m,2}-\widetilde{Z}_{2,1}\widetilde{Z}_{1,2}\widetilde{Z}_{m,3}+\widetilde{Z}_{1,2}\widetilde{Z}_{2,3}\widetilde{Z}_{m,1}}{Z_2^{Th}Z_3^{Th}}}{\widetilde{Z}_{1,1} + Z_1^{Th} - \frac{\widetilde{Z}_{2,1}\widetilde{Z}_{1,2}}{Z_2^{Th}} - \frac{\widetilde{Z}_{3,1}\widetilde{Z}_{1,3}}{Z_3^{Th}} + \frac{\widetilde{Z}_{1,2}\widetilde{Z}_{3,1}\widetilde{Z}_{2,3}+\widetilde{Z}_{2,1}\widetilde{Z}_{1,3}\widetilde{Z}_{3,2}-\widetilde{Z}_{1,1}\widetilde{Z}_{2,3}\widetilde{Z}_{3,2}-\widetilde{Z}_{2,3}\widetilde{Z}_{3,2}Z_1^{Th}}{Z_2^{Th}Z_3^{Th}}}. \tag{30}$$

In these expressions, we have highlighted the large load impedances at terminals two and three in red and the variable load impedance at terminal one in green. These highlights emphasize (a) the dependence of the measured voltage on the modulation imposed by the time variation of the Thévenin impedance at terminal one and (b) the residual measured voltage due to the large load impedances at terminals two and three. As we shall see, the load impedances at terminals two and three should be infinite, imposing open circuit conditions at these probe array terminals and minimizing the errors in the measured voltage due to mutual coupling between probe array elements. However, these load impedances may be determined from free space calibration of the probe array and thus may not be the exact loads required for open circuit condition for the in-situ array.

The first thing to observe from Equations (28), (29) and (30) is that for open circuit conditions at probe array terminals two and three we have

$$\widetilde{H}_{m,1}\Big|_{Z_2^{Th}=Z_3^{Th}=\infty} = \frac{\widetilde{Z}_{m,1}}{\widetilde{Z}_{1,1} + Z_1^{Th}},$$

and

$$\widetilde{H}_{m,2}\Big|_{Z_2^{Th}=Z_3^{Th}=\infty} = \widetilde{H}_{m,3}\Big|_{Z_2^{Th}=Z_3^{Th}=\infty} = 0.$$

As we shall see in the next section, these are the ideal results that would be achieved with an isolated probe located at the position of probe one in the probe array. Remember that the impedance parameters in the expression for $\widetilde{H}_{m,1}$ are the in-situ impedances.

To examine the impact of mutual coupling between probe array elements when the load impedances are large but not infinite, we expand the expressions for the probe array voltage transfer functions maintaining only the dominant error terms due to large but not infinite loads, Z_2^{Th} and Z_3^{Th}, as follows:

$$\widetilde{H}_{m,1} \cong \frac{\widetilde{Z}_{m,1}}{\widetilde{Z}_{1,1} + Z_1^{Th}}\left[1 + \frac{\frac{\widetilde{Z}_{2,1}\widetilde{Z}_{1,2}}{Z_2^{Th}} + \frac{\widetilde{Z}_{3,1}\widetilde{Z}_{1,3}}{Z_3^{Th}}}{\widetilde{Z}_{1,1} + Z_1^{Th}}\right] - \widetilde{Z}_{m,2}\frac{\frac{\widetilde{Z}_{2,1}}{Z_2^{Th}}}{\widetilde{Z}_{1,1} + Z_1^{Th}} - \widetilde{Z}_{m,3}\frac{\frac{\widetilde{Z}_{3,1}}{Z_3^{Th}}}{\widetilde{Z}_{1,1} + Z_1^{Th}}, \tag{31}$$

$$\widetilde{H}_{m,2} \cong \frac{\widetilde{Z}_{m,2}}{Z_2^{Th}} - \frac{\widetilde{Z}_{2,1}\widetilde{Z}_{m,1}}{Z_2^{Th}(\widetilde{Z}_{1,1} + Z_1^{Th})}, \tag{32}$$

and

Approved for public release; distribution is unlimited.

$$\widetilde{H}_{m,3} \cong \frac{\widetilde{Z}_{m,3}}{Z_3^{Th}} - \frac{\widetilde{Z}_{3,1}\widetilde{Z}_{m,1}}{Z_3^{Th}(\widetilde{Z}_{1,1} + Z_1^{Th})}. \tag{33}$$

It is interesting to interpret physically the terms in these transfer functions in terms of the mutual coupling between elements of the probe array. Consider, for example, the approximate expression for the voltage at the measurement probe when only array probe one is excited as given by

$$-\left[E^m(1 + \frac{\widetilde{Z}_{m,m}}{Z_m}) - E^{m_o}\right] \cong \widetilde{H}_{m,1}E_1^{p_o}. \tag{34}$$

Figure 11 gives a signal flow graph interpretation of the terms that contribute to the measured voltage when probe array element one is excited (Equations (31) and (34)). The flow graph nodes represent the currents at the terminals of the probe array, given by I_1, I_2 and I_3 and the voltages at the terminals, given by E_1, E_2 and E_3. The branches represent the impedances and admittances (inverse impedances) that relate the node currents and voltages.

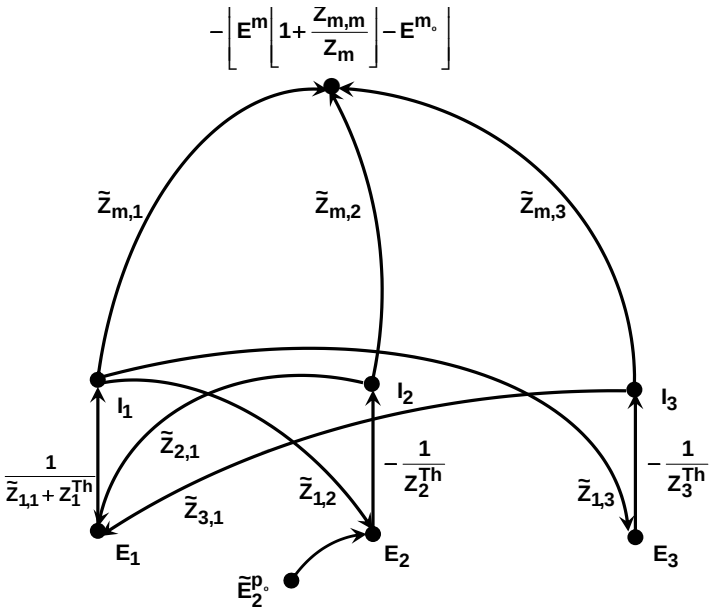

Figure 11: Signal Flow Graph Representation of the Dominant Contributions to the Measured Voltage When Probe Array Element One Is Excited and the Other Elements Are Loaded with Large Impedances

Figure 12 shows the paths in the signal flow graph that contribute to the individual terms in $\widetilde{H}_{m,1}$. To the left in red is the path that contributes the direct radiation from probe array element one due to the open circuit voltage at element one, $E_1^{p_o}$, which introduces the current at element one terminals, $E_1^{p_o}/(\widetilde{Z}_{1,1}+Z_1^{Th})$. This current through the mutual impedance between probe array element one and the measurement probe, $\widetilde{Z}_{m,1}$, contributes one term of the measurement voltage.

In the center of Figure 12, we illustrate in blue the contributions to the measured voltage due to first order mutual coupling between probe array elements. The current at probe array element one excited by the open circuit voltage $E_1^{p_o}$ couples to the voltages at elements two and three of the probe array through the

Approved for public release; distribution is unlimited.

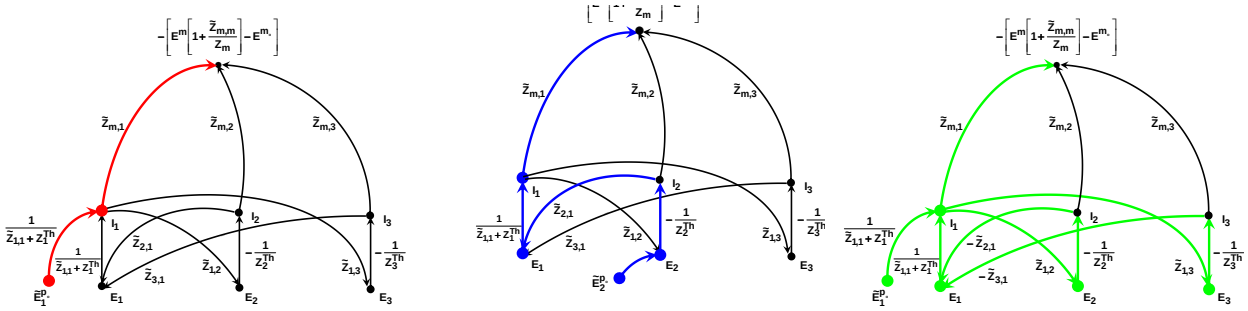

Figure 12: Signal Flow Graph Representation Showing Each Dominant Contribution to the Measured Voltage When Probe Array Element One Is Excited

mutual impedances $\widetilde{Z}_{1,2}$ and $\widetilde{Z}_{1,3}$ respectively. These voltages introduce the currents at terminals two and three through the large load impedances at these terminals, Z_2^{Th} and Z_3^{Th}, respectively. The negative signs assocated with these branch impedances account for the convention assigned to currents entering the probe array terminals. Finally, the probe array currents contribute to the measurement voltage through the mutual impedances between the probe array elements and the measurement probe, $\widetilde{Z}_{m,2}$ and $\widetilde{Z}_{m,3}$, respectively.

Finally, to the right in Figure 12 we show in green the contributions to the measured voltage due to second order mutual coupling between the elements of the probe array. Again the current at probe array element one couples to the the voltages at elements two and three of the probe array. These voltages excite the probe element currents through the large load impedances at the element terminals and these currents in turn contribute via superposition to the voltage at probe array element one. This voltage in turn excites an additional component of the current at element one which contributes to the voltage at the measurement probe.

Figure 12 shows only the dominant contributions to the measured voltage when the load impedances at terminals two and three are large. The fact that only the dominant contributions are considered results from selecting only those paths in the flow graph from excitation voltage to measured voltage that traverse only once a branch with large load impedance. Of course, the general solution requires finding all paths from excitation to measured voltages using the general procedures for solving signal flow graph transmission factors. Indeed, the flow graphs in Figures 11 and 12 are not sufficient for solution to the general problem since we have not included all mutual coupling between probe array elements, such as, for example, between probe array elements two and three.

In like manner, we illustrate in a signal flow graph the contributions to the measured voltage when one of the probe array elements with large load impedances is excited. Figure 13 shows this signal flow graph when element two is excited. Figure 14 shows the two dominant contributions to the measured voltage when the load impedances are large. That is, we consider only those path that traverse once a branch with large load impedance (or near zero branch transmission).

Figure 14 shows the individual contributions to the measured voltage. To the left in red is the direct path from the voltage at element two, E_2, to the current at that terminal, I_2, and finally to the measurement probe via the mutual impedance, $\widetilde{Z}_{m,2}$. To the right, in blue, is the path via elements two and one. The current at element two excites a contribution to the voltage at probe array element 1. This voltage contributes a component of the current at probe array element one via the variable load impedance, $\widetilde{Z}_{1,1} + Z_1^{Th}$. This current in turn contributes to the measured voltage via the mutual impedance, $\widetilde{Z}_{m,2}$. Note that these are the only paths from excitation voltage to measured voltage that traverse a branch with large load impedance only once.

Approved for public release; distribution is unlimited.

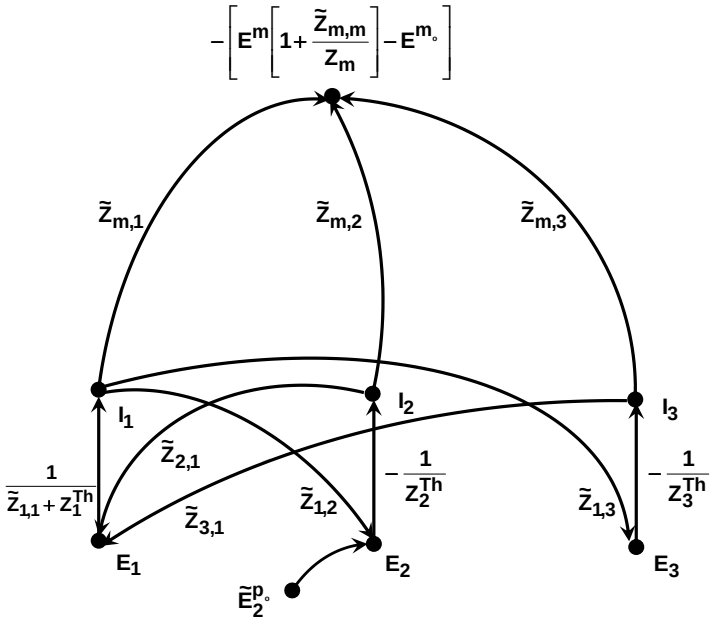

Figure 13: Signal Flow Graph Representation of the Dominant Contributions to the Measured Voltage When Probe Array Element Two Is Excited

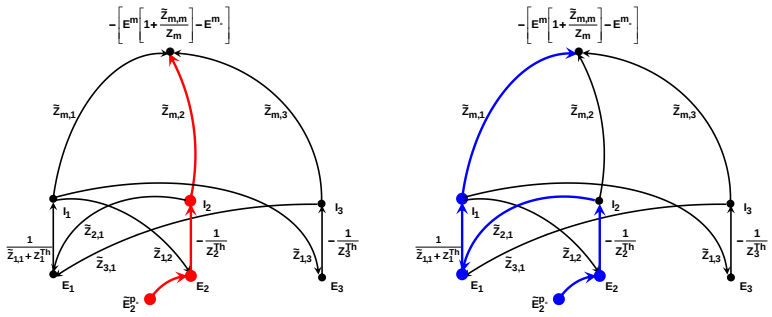

Figure 14: Signal Flow Graph Representation Showing Each Dominant Contribution to the Measured Voltage When Probe Array Element Two Is Excited

It is clear from Equations (28), (29) and (30), that if the Thévenin load impedances create open circuit conditions at the terminals of each probe array element, then the measured voltage, E^m, will be proportional to only the plane wave induced voltage at the terminal with the modulated impedance. This is the desired measurement condition corresponding, as we shall see in the next section, to a single isolated probe. However, when the load impedances fail to cancel the currents at the probe array element terminals, then errors in the measurements occur due to mutual coupling between array elements as described in the last paragraphs. The condition where the probe array currents are not completely cancelled occurs, for example, when the Thévenin load impedances are determined from the free space array mutual impedances rather than the in-situ impedances [29]. We shall examine in the next section the error introduced into the measured voltage by improper loading of the probe array terminals.

Approved for public release; distribution is unlimited.

3.3 Modulated Scatterer Performance

3.3.1 Single Probe Performance

We begin with a study of the performance of a single modulated scattering (MS) probe in the presence of the scattering body. This performance will serve as a baseline for comparison with the performance of the probe array. In addition, the study will reveal several considerations regarding the accuracy with which the magnitude and phase of the field at the modulated scattering probe can be made.

To begin, examine the mutual impedance representation of the configuration of the near field MS probe and the remote measurement probe when excited externally by a plane wave source. This representation is

$$\begin{aligned} E_i &= E_i^{p_o} + Z_{i,i} I_i + Z_{i,m} I_m \\ E_m &= E^{m_o} + Z_{m,i} I_i + Z_{m,m} I_m, \end{aligned} \tag{35}$$

where E_i and I_i are the voltage and current respectively at the terminals of the near field MS probe at position i and E_m and I_m are the voltage and current respectively at the terminals of the remote measurement probe. Also, $E_i^{p_o}$ and E^{m_o} represent the open circuit voltages induced at the terminals of the near field probe and measurement probe, respectively, by the external excitation.

At the terminals of the MS near field probe we introduce a passive load represented by the Thévenin equivalent impedance Z_i^{Th}. This impedance will serve as the modulation source for the modulated scatterer measurements. Then we can write

$$E_i = -Z_i^{Th} I_i.$$

Applying this to the first of Equations (35) gives

$$-Z_i^{Th} I_i = E_i^{p_o} + Z_{i,i} I_i + Z_{i,m} I_m,$$

or

$$E_i^{p_o} = -(Z_{i,i} + Z_i^{Th}) I_i,$$

under open circuit conditions at the measurement probe ($I_m = 0$). Then the open circuit voltage at the measurement probe from the second of Equations (35) is given by

$$E_m^{oc}(t) = E^{m_o} + Z_{m,i} I_i = E^{m_o} - \frac{Z_{m,i}}{Z_{i,i} + Z_i^{Th}(t)} E_i^{p_o} = E^{m_o} - \widetilde{H}_{m,i}(t) E_i^{p_o}.$$

This expression defines the time varying voltage transfer function

$$\widetilde{H}_{m,i}(t) = \frac{Z_{m,i}}{Z_{i,i} + Z_i^{Th}(t)}. \tag{36}$$

Here we included the modulated scatterer condition showing that the open circuit measured votage varies with time when the equivalent near field probe impedance, $Z_i^{Th}(t)$, varies with time.

Recalling that the objective of the modulated scatterer technique is the accurate measurement of the amplitude and phase of the voltage induced in the MS near field probe, $E_i^{p_o}$. However, it is clear that, in general, changes in the modulating impedance, $Z_i^{Th}(t)$, will change the magnitude and phase of the voltage transfer function which in turn modifies the voltage and phase of the measured voltage $E_m^{oc}(t)$. Accurate measurement of the magnitude and phase of the MS near field probe voltage will then require calibration of the measurement system and its transfer function, $\widetilde{H}_{m,i}(t)$.

Approved for public release; distribution is unlimited.

Recall that the impedances $Z_{m,i}$ and $Z_{i,i}$ in the measurement voltage transfer function depend on (1) the relative locations of the MS near field probe and the measurement probe and (2) the surrounding environmental conditions, specifically the presence or absence of the scattering body to be measured. Thus the measurement transfer function and the voltage at the measurement probe depend on whether the scattering body is present or absent. We conclude that calibration of the measurement system and its transfer function must be made when the target is present unless we are able to accept the errors that occur when the measurement system is calibrated is free space, with the target absent.

To assess these errors, we analyze numerically a sample problem considered in previous work [29]. In this report, we considered a target that interacts strongly with the probe array. The model is shown in Figure 15. It consists of a flat plate of dimensions 2λ by $\lambda/2$ at a distance of 2λ from a 5 element probe array. Here λ denotes the wavelength of the plane wave excitation. As indicated, the measurement array consists of 5 dipoles which are 0.48λ in length with $\lambda/2$ inter-element spacing located on the y axis. The plate and plane wave excitation are oriented so the the probe array is in the far field specular scattering direction from the plate, although the probe array itself is in the near field of the plate scattering. The elements of the probe array are numbered 1 through 5 with element 1 closest to the plate (Figure 15).

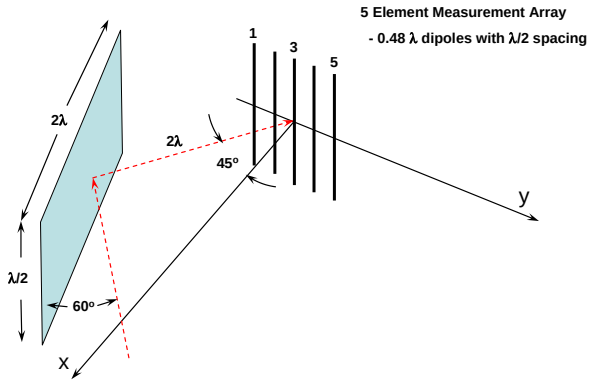

Figure 15: Flat Plate and Measurement Array

For purposes of numerical analysis with NEC4, the surrogate flat plate is synthesized with a collection 41 parallel, half wavelength dipoles oriented in the z direction and packed such that the inter-dipole spacing is 0.05λ. All dipoles have a radius of $8 \cdot 10^{-4}\lambda$. The plane wave excitation for the plate-array configuration consists of a z directed electric field with E=1 v/m.

To extend this model to represent the conventional modulated scattering scheme, a single modulated scattering probe is placed initially at each position occupied by the probe array elements. Further, a measurement probe with open circuit terminals is placed 30λ from the center location of the probe array and at an angle of 60° with respect to the array axis. This configuration is shown in Figure 16.

NEC4 is used to obtain the self and mutual impedances between the modulated scatterer probe and the measurement probe with and without the presence of the surrogate flat plate. These impedances are used to evaluate the measurement voltage transfer function (Equation (36)) and the errors that occur when free space calibration is used to determine the in-situ probe voltage.

Figure 17 shows the magnitude of the relative in-situ measurement voltage transfer function as a function of admittance of the Thévenin load, $Y^{Th} = G + jB = 1/Z^{Th}$. Here G is the conductance of the load and B is the load susceptance. In this Figure, the magnitude of the relative in-situ transfer function is given by

$$\left| \frac{\widetilde{H}_{m,i}}{Z_{m,i}/Z_{i,i}} \right|$$

Approved for public release; distribution is unlimited.

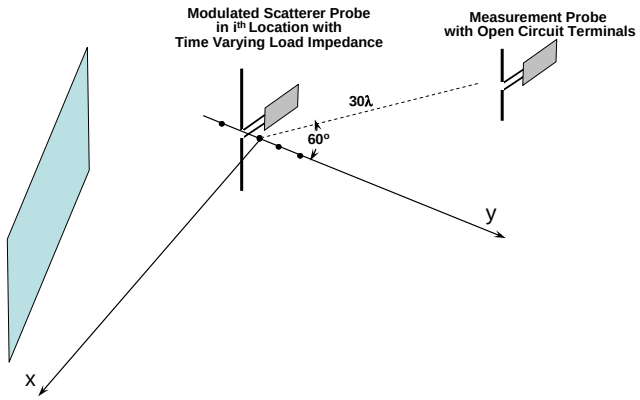

Figure 16: Single Modulated Scatterer Probe in the Presence of a Flat Plate and the Measurement Probe

where the denominator normalization represents the magnitude of the transfer function when the Thévenin load impedance is zero. Figure 18 shows the phase of the voltage transfer function. Figures17 and 18 apply for the modulated scatterer probe located in the array element position 1 closest to the flat plate target (See Figure 15).

Recall that to implement the modulated scatterer technique, the Thévenin load at the probe terminals will be changed to modulate the voltage at the measurement probe. It is clear from Figures 17 and 18 that the voltage at the measurement probe is most sensitive to changes in the load admittance when the admittance is near zero. This corresponds to near open circuit conditions at the probe terminals, a condition which minimizes the interaction between the probe and the scatterer. Under this condition, the in-situ measurement voltage transfer function can be approximated as

$$\widetilde{H}_{m,i}(t) \simeq Z_{m,i} Y_i^{Th}(t),$$

and

$$E_m^{oc}(t) = E^{m_o} - \frac{Z_{m,i}}{Z_{i,i} + {}^1\!/_{Y_i^{Th}(t)}} E_i^{p_o} \simeq E^{m_o} - Z_{m,i} Y_i^{Th}(t) E_i^{p_o}.$$

That is, the time variation of the open circuit voltage at the measurement probe is proportional to the modulating admittance, $Y_i^{Th}(t)$, and the in-situ mutual impedance between the modulated scatterer probe and the measurement probe, $Z_{m,i}$.

Two observations are important here. First, changes in the modulating load admittance change both the amplitude and phase of the open circuit voltage at the the measurement probe as we have observed in Figures 17 and 18. Thus, to recover the amplitude and phase of $E_i^{p_o}$, the voltage induced by the incident plane wave and target scattering at the modulating probe adjacent to the scattering body, we need to calibrate the measurement system with a known field such as might be induced by the plane wave without target present. A second observation follows. If the measurement system is calibrated in free space, then the mutual impedance $Z_{m,i}$ (and self impedance $Z_{i,i}$) in the calibration will be the free space parameters and thus errors will be introduced into the calibration process to the extent that these impedances differ from their corresponding in-situ values. We study the significance of these errors in the following.

Figures 19, 20, and 21 show the errors in relative magnitude and phase of the measurement voltage transfer function for a single probe located in probe array position one (nearest the flat plate target), three (probe

Approved for public release; distribution is unlimited.

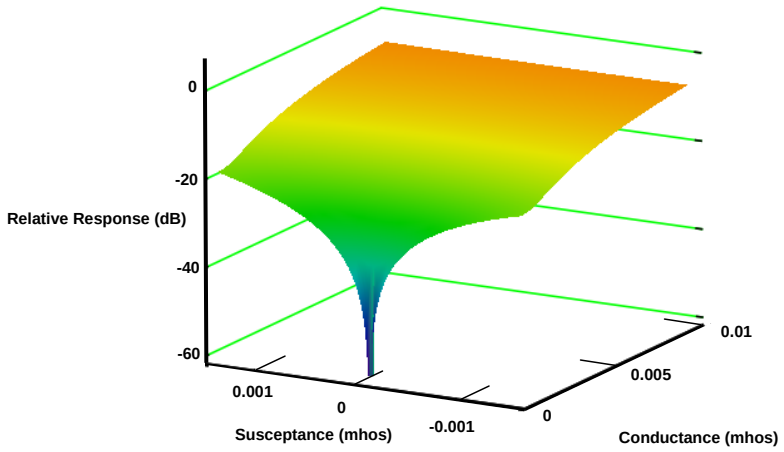

Figure 17: Magnitude of the Relative In-Situ Measurement Voltage Transfer Function as a Function of the Load Admittance at the Modulated Scatterer Probe

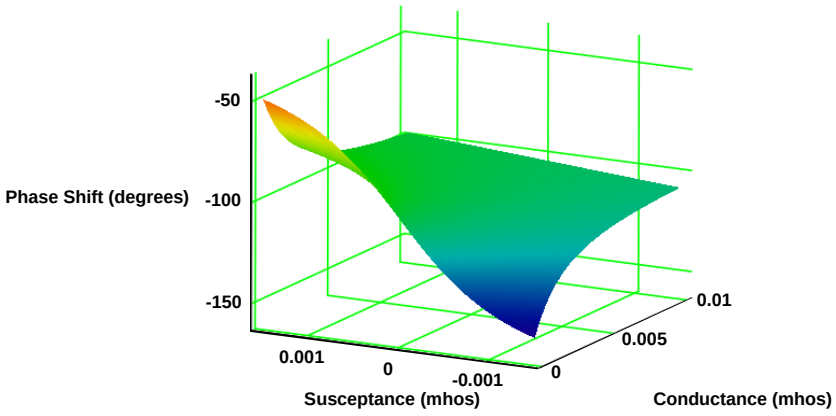

Figure 18: Phase of the Relative In-Situ Measurement Voltage Transfer Function as a Function of the Load Admittance at the Modulated Scatterer Probe

Approved for public release; distribution is unlimited.

array center element) and five (farthest from the flat plate target), respectively. The errors are shown as a function of the conductance and susceptance of the Thévenin admittance at the modulated probe. In these Figures the relative magnitude error is given by

$$\mathscr{E} = \left| \frac{\widetilde{H}^{is}_{m,i}(Y^{Th}) - \widetilde{H}^{fs}_{m,i}(Y^{Th})}{\widetilde{H}^{is}_{m,i}(Y^{Th})} \right|,$$

and the phase error is given by

$$arg(\widetilde{H}^{is}_{m,i}(Y^{Th})) - arg(\widetilde{H}^{fs}_{m,i}(Y^{Th})).$$

In these expressions, $\widetilde{H}^{is}_{m,i}(Y^{Th})$ and $\widetilde{H}^{fs}_{m,i}(Y^{Th})$ are the measurement voltage transfer functions between element position i, $i = 1, 3, 5$ and the measurement probe as a function of the Thévenin admittance at the modulated probe for in-situ (is) and free space (fs) conditions respectively. For these conditions, the self and mutual impedances with the target present and absent are used in the expression for the voltage transfer functions. Here $arg(\cdot)$ denotes the phase angle of its complex valued argument.

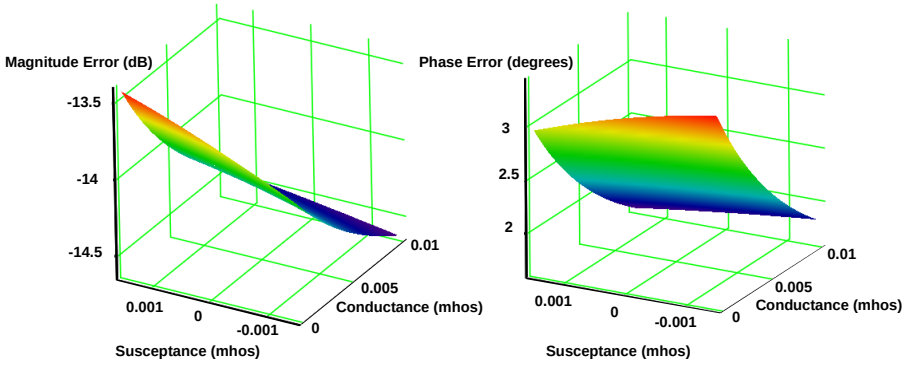

Figure 19: Errors in Relative Magnitude and Phase of the Measurement Voltage Transfer Function for a Single Probe Located in Probe Array Position One

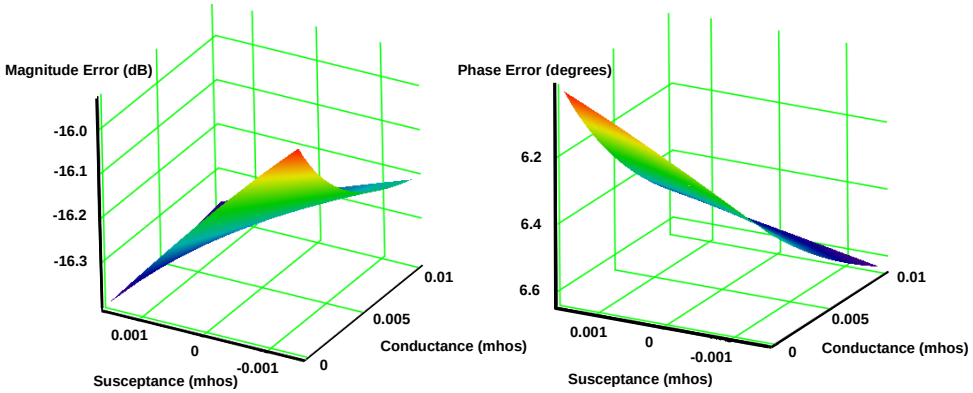

Figure 20: Errors in Relative Magnitude and Phase of the Measurement Voltage Transfer Function for a Single Probe Located in Probe Array Position Three

Approved for public release; distribution is unlimited.

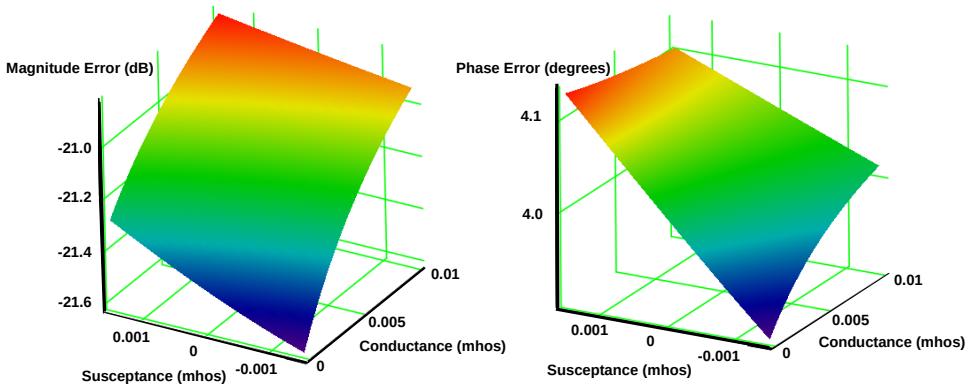

Figure 21: Errors in Relative Magnitude and Phase of the Measurement Voltage Transfer Function for a Single Probe Located in Probe Array Position Five

Careful examination of Figures 19, 20, and 21 indicates that less than -13.5 dB error in magnitude and only a few degrees of phase error occur in the voltage transfer function when using the free space calibration of the transfer function to obtain the magnitude and phase of the induced voltage in the modulated scattering probe. The worst case of error magnitude occurs for the probe element nearest the flat plate and the error decreases to less than -20 dB for the probe at a position farthest from the plate. Depending on requirements for measurement system accuracy and demands for probe location with respect to the scattering body, it appears that free space calibration of the measurement system can be considered, especially since its relative simplicity in implementation will accelerate the overall measurement process. Should these errors be unacceptable, the alternative is to measure the in-situ self and mutual impedances between the modulated and measurement probes. This process would involve an independent source at either of the probe locations to be used for measurement of the impedances when no external plane wave excitation exists.

3.3.2 Probe Array Performance

Now we turn to evaluating the performance of the probe array using the analysis developed in Section 3.2 of this report. We continue with a NEC4 numerical analysis of the five element probe array in the presence of the surrogate flat place as illustrated in Figures 15 and 16. The impedance modulated measurement probe is located as described in Figure 16.

We have seen in previous sections that calibration of the measurement system is necessary to account for (1) the unknown mutual coupling between the elements of the probe array and the measurement dipole which changes as the probe array is displaced, and (2) the modulating load impedance at the terminal of the relevant probe array element. This calibration is important to achieve accurate measurements of both the amplitude and phase of the excitation field at each element of the probe array. In principle, there are two approaches to probe array calibration.

In-situ calibration is the preferred approach since it accounts for the effects of target interaction in the probe array mutual impedances. However this calibration approach is difficult since it requires that we excite in turn each probe array element with a known voltage while creating open circuit conditions at the other, non-excited elements of the array. This follows from comparison of the analyses in Sections 3.2 and 3.3.1. The calibration voltage and open circuit load conditions must be applied as an integral part of the probe array source and feed manifold. This creates a larger probe array structure in the presence of the scattering body with the potential for more significant perturbation of the current distribution on the body.

An alternate calibration approach employs the probe array in free space without the target present and with a known plane wave excitation. Here the plane wave fields create a known excitation voltage at each probe array element. As follows from the analysis in Section 3.2, a modulating load impedance is created sequentially at each element of the probe array while open circuit conditions are created at the other elements. The voltage observed at the measurement dipole accounts for (1) the mutual impedance between the measurement dipole and the modulated probe array element, (2) the variation of the modulating impedance and (3) plane wave excitation amplitude and phase at the spatial location of the modulated probe array element. Of course, this calibration must be performed (1) for each probe array element separately, (2) each spatial position of the probe array, (3) each frequency of the plane wave excitation and (4) each plane wave orientation to be employed in the measurements. Errors are introduced by this calibration process due to the fact that the calibration intrinsically employs the free space mutual impedances of the probe array. In this section we analyze the errors that are intrinsic in this free space calibration process. These errors are quantified for the five element probe array and surrogate flat plate described in Figures 15 and 16 using numerical analysis of this structure with NEC4.

For the free space calibration process, we consider the active impedance characterization of the probe array in free space given by Equation (22) for free space conditions:

$$\begin{bmatrix} E_1 \\ E_2 \\ E_3 \\ E_m \end{bmatrix} = \begin{bmatrix} E_1^{pw} \\ E_2^{pw} \\ E_3^{pw} \\ E_m^{pw} \end{bmatrix} + \begin{bmatrix} \widetilde{Z}_{1,1}^{fs} & \widetilde{Z}_{1,2}^{fs} & \widetilde{Z}_{1,3}^{fs} & \widetilde{Z}_{1,m}^{fs} \\ \widetilde{Z}_{2,1}^{fs} & \widetilde{Z}_{2,2}^{fs} & \widetilde{Z}_{2,3}^{fs} & \widetilde{Z}_{2,m}^{fs} \\ \widetilde{Z}_{3,1}^{fs} & \widetilde{Z}_{3,2}^{fs} & \widetilde{Z}_{3,3}^{fs} & \widetilde{Z}_{3,m}^{fs} \\ \widetilde{Z}_{m,1}^{fs} & \widetilde{Z}_{m,2}^{fs} & \widetilde{Z}_{m,3}^{fs} & \widetilde{Z}_{m,m}^{fs} \end{bmatrix} \begin{bmatrix} I_1 \\ I_2 \\ I_3 \\ I_m \end{bmatrix}.$$

Here $\widetilde{Z}_{i,j}^{fs}$, $i = 1, 2, 3, m$ and $j = 1, 2, 3, m$ denotes the self and mutual impedances between array elements and between an array element and the measurement dipole when the array and measurement dipole are located in free space with the target absent. Also, E_i^{pw}, $i = 1, 2, 3, m$ is the open circuit voltage induced at each terminal due to the plane wave excitation of the array and measurement dipole. Each terminal of the probe array is loaded with a Thévenin equivalent source as discussed in connection with Equations (23) through (24) giving, from Equation (24)

$$E_m(1+\frac{\widetilde{Z}_{m,m}^{fs}}{Z_m}) = E_m^{pw}+\begin{bmatrix} \widetilde{Z}_{m,1}^{fs} & \widetilde{Z}_{m,2}^{fs} & \widetilde{Z}_{m,3}^{fs} \end{bmatrix} \begin{bmatrix} \widetilde{Z}_{1,1}^{fs}+Z_1^{Th} & \widetilde{Z}_{1,2}^{fs} & \widetilde{Z}_{1,3}^{fs} \\ \widetilde{Z}_{2,1}^{fs} & \widetilde{Z}_{2,2}^{fs}+Z_2^{Th} & \widetilde{Z}_{2,3}^{fs} \\ \widetilde{Z}_{3,1}^{fs} & \widetilde{Z}_{3,2}^{fs} & \widetilde{Z}_{3,3}^{fs}+Z_3^{Th} \end{bmatrix}^{-1} \begin{bmatrix} E_1^{Th}-E_1^{pw} \\ E_2^{Th}-E_2^{pw} \\ E_3^{Th}-E_3^{pw} \end{bmatrix}.$$

There are two possibilities to achieving the open circuit conditions necessary to calibrate the array. One possibility to calibrate probe array element i is to set $E_i^{Th} = 0$ and require that $E_j^{Th} = E_j^{pw}$, $j \neq i$ to create open circuit conditions at the other probe array elements. Alternately, the open circuit conditions at these element can be achieved by requiring that the Thévenin impedance at these terminals be large. We follow the second approach here.

We have seen earlier in Section 3.2 that it is important that all of the probe array terminals except the one with a modulating impedance be loaded to obtain open circuit conditions. Failure to obtain the open circuit conditions results in errors in both the calibration of the array and the measurement of the required probe array open circuit voltages at each probe array terminal. Thus, we study the errors in calibration and measurement that occur when the experimental conditions fail to provide for full cancellation of the probe array terminal currents.

Initially we describe the loading conditions that create small but non-zero current conditions at each terminal. Throughout this work we have assumed that the Thévenin equivalent loads for the probe array are such that each terminal voltage depends only on that terminal load impedance and terminal current. It is not dependent on the currents at other terminals through mutual impedance characterization of the

Approved for public release; distribution is unlimited.

probe array loads. This assumption is equivalent to requiring that the Thévenin equivalent load matrix be diagonal as included implicitly in Equation (23) and the analysis that follows this equation in Section 3. That is we now write

$$\bar{E}^{Th} = \bar{E}^{pw} + (\bar{\bar{Z}} + \bar{\bar{Z}}^{Th})\bar{I},$$

where $\bar{E}^{Th}$ denotes a column matrix of Thévenin equivalent voltage sources at the probe array terminals, $\bar{E}^{pw}$ is a column matrix of open circuit voltages induced by exterior radiation at the probe array terminals, $\bar{I}$ is a column matrix of probe array terminal currents, and $\bar{\bar{Z}}$ is either the free space or in-situ self and mutual impedance matrix describing the relationships between terminal voltages and currents. Finally, $\bar{\bar{Z}}^{Th}$is the diagonal matrix that describes the impedance loading of the probe array terminals.

The probe array short circuit currents are found with $\bar{E}^{Th} = \bar{0}$ and $\bar{\bar{Z}}^{Th} = \bar{\bar{0}}$ and are then given by

$$\bar{0} = \bar{E}^{pw} + \bar{\bar{Z}}\bar{I}_{sc},$$

or

$$\bar{I}_{sc} = -\bar{\bar{Z}}^{-1}\bar{E}^{pw}.$$

These short circuit currents are the base line by which we compare the residual currents at the impedance loaded terminals of the probe array.

Now, under passive loading conditions (all Thévenin equivalent voltage sources are zero) the probe array loaded currents, $\bar{I}_{load}$, are given by the solution to

$$\bar{0} = \bar{E}^{pw} + (\bar{\bar{Z}} + \bar{\bar{Z}}^{Th})\bar{I}_{load}.$$

We now require that the currents under loading conditions be a fraction of the short circuit currents or

$$\bar{I}_{load} = \bar{\bar{\gamma}}\bar{I}_{sc},$$

where $\bar{\bar{\gamma}}$ is a diagonal matrix expressing the decrease in terminal currents from short circuit conditions due to terminal loading. Then we can write

$$\bar{0} = \bar{E}^{pw} + (\bar{\bar{Z}} + \bar{\bar{Z}}^{Th})\bar{\bar{\gamma}}\bar{I}_{sc},$$

or

$$\bar{\bar{Z}}^{Th}\bar{\bar{\gamma}}\bar{I}_{sc} = -\bar{E}^{pw} - \bar{\bar{Z}}\bar{\bar{\gamma}}\bar{I}_{sc}, \tag{37}$$

Now we wish to solve for the elements of the diagonal Thévenin load impedance, $\bar{\bar{Z}}^{Th}$. We rewrite the left side of Equation (37) as

$$\bar{\bar{Z}}^{Th}\bar{\bar{\gamma}}\bar{I}_{sc} = \bar{\bar{I}}_{atten}\bar{Z}^{Th},$$

where the NxN diagonal matrix of attenuated currents is given by

$$\bar{\bar{I}}_{atten} = diag(I_{sc_i}\gamma_i,\ i = 1, 2, ..., N),$$

and N denotes the number of elements in the probe array. Also, the column vector of Thévenin load impedances is given by

$$\bar{Z}^{Th} = col(Z^{Th}_{i,i},\ i = 1, 2, ..., N).$$

It follows that the required load impedance at each terminal is given by

$$\bar{Z}^{Th} = -\bar{\bar{I}}^{-1}_{atten}(\bar{E}^{pw} + \bar{\bar{Z}}\bar{\bar{\gamma}}\bar{I}_{sc}). \tag{38}$$

We note parenthetically that while the load impedances $\bar{Z}^{Th}$ determined from Equation (38) are useful for the following analysis, there is no implicit requirement from this development that the loads be realizable with passive impedances.

Approved for public release; distribution is unlimited.

With these loading condition we examine several errors in the calibration and measurement process as a function of the parameters involved in the matrix, $\bar{\bar{\gamma}}$, and the modulating impedance or admittance. Specifically we consider the following errors:

$$\mathscr{E}^{oc\,load}_{fs\,calibration} = \left| \frac{\widetilde{H}^{is}_{m,i}\Big|_{\substack{Z^{Th}_j=\infty \\ j\neq i}} \quad -\widetilde{H}^{fs}_{m,i}\Big|_{\substack{Z^{Th}_j=\infty \\ j\neq i}}}{\widetilde{H}^{is}_{m,i}\Big|_{\substack{Z^{Th}_j=\infty \\ j\neq i}}} \right| \text{ Open Circuit Loading; Free Space Calibration,}$$

$$\mathscr{E}^{Z\,load}_{fs\,calibration} = \left| \frac{\widetilde{H}^{is}_{m,i}\Big|_{\substack{Z^{Th}_j=\infty \\ j\neq i}} \quad -\widetilde{H}^{fs}_{m,i}\Big|_{\substack{Z^{Th}_j=Z^{Th}_j(\bar{\bar{\gamma}}) \\ j\neq i}}}{\widetilde{H}^{is}_{m,i}\Big|_{\substack{Z^{Th}_j=\infty \\ j\neq i}}} \right| \text{ Impedance Loading; Free Space Calibration,}$$

$$\mathscr{E}^{Z\,load}_{is\,calibration} = \left| \frac{\widetilde{H}^{is}_{m,i}\Big|_{\substack{Z^{Th}_j=\infty \\ j\neq i}} \quad -\widetilde{H}^{is}_{m,i}\Big|_{\substack{Z^{Th}_j=Z^{Th}_j(\bar{\bar{\gamma}}) \\ j\neq i}}}{\widetilde{H}^{is}_{m,i}\Big|_{\substack{Z^{Th}_j=\infty \\ j\neq i}}} \right| \text{ Impedance Loading; In-Situ Calibration.}$$

The first error, $\mathscr{E}^{oc\,load}_{fs\,calibration}$, represents the magnitude of the relative error when calibration of the probe array takes place in free space with perfect, open circuit loading of the probe array terminals not involved in the calibration. This error and its associated phase error will be considered as a function of the modulating load impedance or admittance at the terminal being calibrated. In a similar manner, the second error, $\mathscr{E}^{Z\,load}_{fs\,calibration}$, is the magnitude of the relative error when calibration of the probe array takes place in free space. However, here the loading of the array terminals not involved in calibration are imperfectly loaded such that the Thévenin load impedances are determined using Equation (38) under free space conditions. Again, this error and its associated phase error will be considered as a function of both the modulating load impedance or admittance and the current cancellation parameters, $\bar{\bar{\gamma}}$. Finally, the third error, $\mathscr{E}^{Z\,load}_{is\,calibration}$, represents the magnitude of the relative error when measurements are made with imperfect loading of the non-measurement probe array terminals. Again, these loads are determined by Equation (38) under in-situ conditions and the error and its associated phase error will be considered as a function of both the load impedance or admittance and the current cancellation parameters.

Figures 22, 23 and 24 illustrate the magnitude and phase associated with error, $\mathscr{E}^{oc\,load}_{fs\,calibration}$, when (1) a modulating impedance is placed at probe array elements one (nearest to the surrogate plate), three and five (farthest from plate), respectively, (2) the calibration of the probe array takes place in free space, and (3) open circuit loading is placed at the non-modulated array elements. The errors are given as a function of the conductance and suseceptance of the modulating load admittance (inverse load impedance). In these Figures, the phase errors here are given by

$$arg\left[\widetilde{H}^{is}_{m,i}\Big|_{\substack{Z^{Th}_j=\infty \\ j\neq i}}\right] - arg\left[\widetilde{H}^{fs}_{m,i}\Big|_{\substack{Z^{Th}_j=\infty \\ j\neq i}}\right],$$

where $arg\,[\cdot]$ denotes the phase angle of the complex valued argument.

Approved for public release; distribution is unlimited.

The magnitude of the error varies from -13.5 dB for the element closest to the plate to -20.5 dB for the element farthest from the plate. The errors depend on (1) the coupling between the array element and the target, a surrogate flat plate and (2) the mutual coupling between array elements. Obviously, the error due to element-target coupling cannot be minimized using free space calibration as is assumed here. Errors due to mutual coupling can be minimized to the extent that in-situ mutual impedances can be adequately characterized by the free space impedance measurements used in these Figures. We hypothesize that this explains the differences between the errors found at element one (nearest the flat plate) and five (farthest from the plate). At element one, the coupling to the plate is most significant and accurate, in-situ characterization of the self impedance of this probe array element and the mutual impedance to the measurement probe is most importance. Element five is farthest from the plate with reduced coupling to the flat plate. In this case, the self impedance of the element and mutual coupling to the measurement probe found from free space calibration more accurately approximates the in-situ impedances required for accurate calibration. We investigate this hypothesis in further study described in the following.

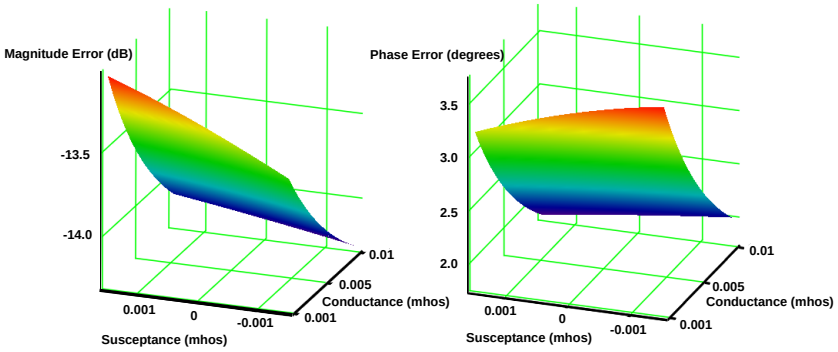

Figure 22: Magnitude and Phase Error of Calibration of Probe Array Element One (Nearest to Plate) with Open Circuit Loading at Other Elements ($\mathscr{E}^{oc\,load}_{fs\,calibration}$)

Approved for public release; distribution is unlimited.

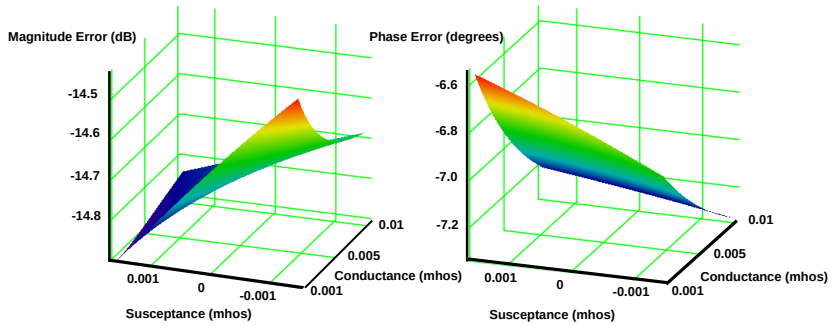

Figure 23: Magnitude and Phase Error of Calibration of Probe Array Element Three with Open Circuit Loading at Other Elements ($\mathscr{E}_{fs\ calibration}^{oc\ load}$)

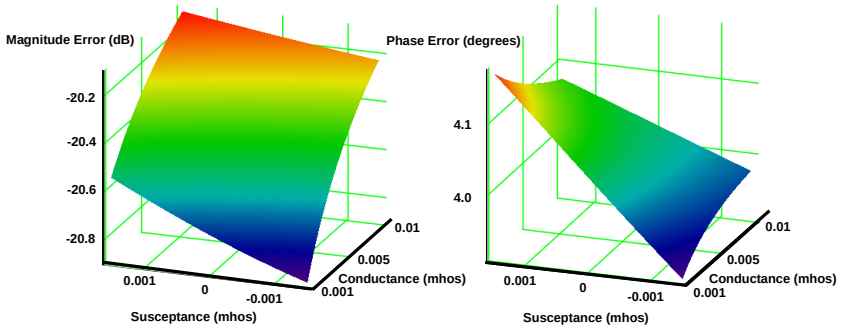

Figure 24: Magnitude and Phase Error of Calibration of Probe Array Element Five (Farthest from Plate) with Open Circuit Loading at Other Elements ($\mathscr{E}_{fs\ calibration}^{oc\ load}$)

The results in Figures 22, 23 and 24 assume that the currents are perfectly cancelled at the terminals of the probe array elements that are not loaded by the modulating impedance. Of course perfect current cancellation is difficult to achieve experimentally since this condition requires wideband, open circuit conditions at the probe array terminals. Figures 25, 26 and 27 illustrate the magnitude and phase error of probe array elements one, three and five respectively when the currents at the non-modulated element are partially cancelled. Specifically, in each Figure, currents are cancelled from their short circuit values when plane wave excited in free space by 0 dB (top), -10 dB (middle) and -20 dB (bottom). The impedance loads are found from Equation (38) employing the free space impedance parameters of the probe array.

Careful examination of these Figures indicates that probe array element one closest to the surrogate flat plate target is least sensitive to current cancellation at the other probe array elements. As illustrated in Figure 25, the error decreases from approximately -8.5 dB with short circuit current conditions to approximately -13.5 dB when the current is decreased by -10 dB. A further decrease in the currents to -20

Approved for public release; distribution is unlimited.

dB has negligible effect on the magnitude of the error at the terminal to probe array element one. Contrast this with the calibration error given in Figure 27 for the element farthest from the surrogate flat plate. Here decreasing the load currents by -20 dB reduces the magnitude of the calibration error to approximately the open circuit conditions shown in Figure 24. A summary of the results in Figures 22, 23, 24, 25, 26 and 27 is given in Table 1.

Table 1: Summary of the Magnitude of Calibration Error with Impedance Loading for Free Space Calibration

Current Attenuation	Element 1	Element 3	Element 5
0 dB	-8	-6	-11
-10 dB	-13.5	-10	-19
-20 dB	-13.5	-13	-20
Open Circuit	-13.5	-14.6	-20.5

Approved for public release; distribution is unlimited.

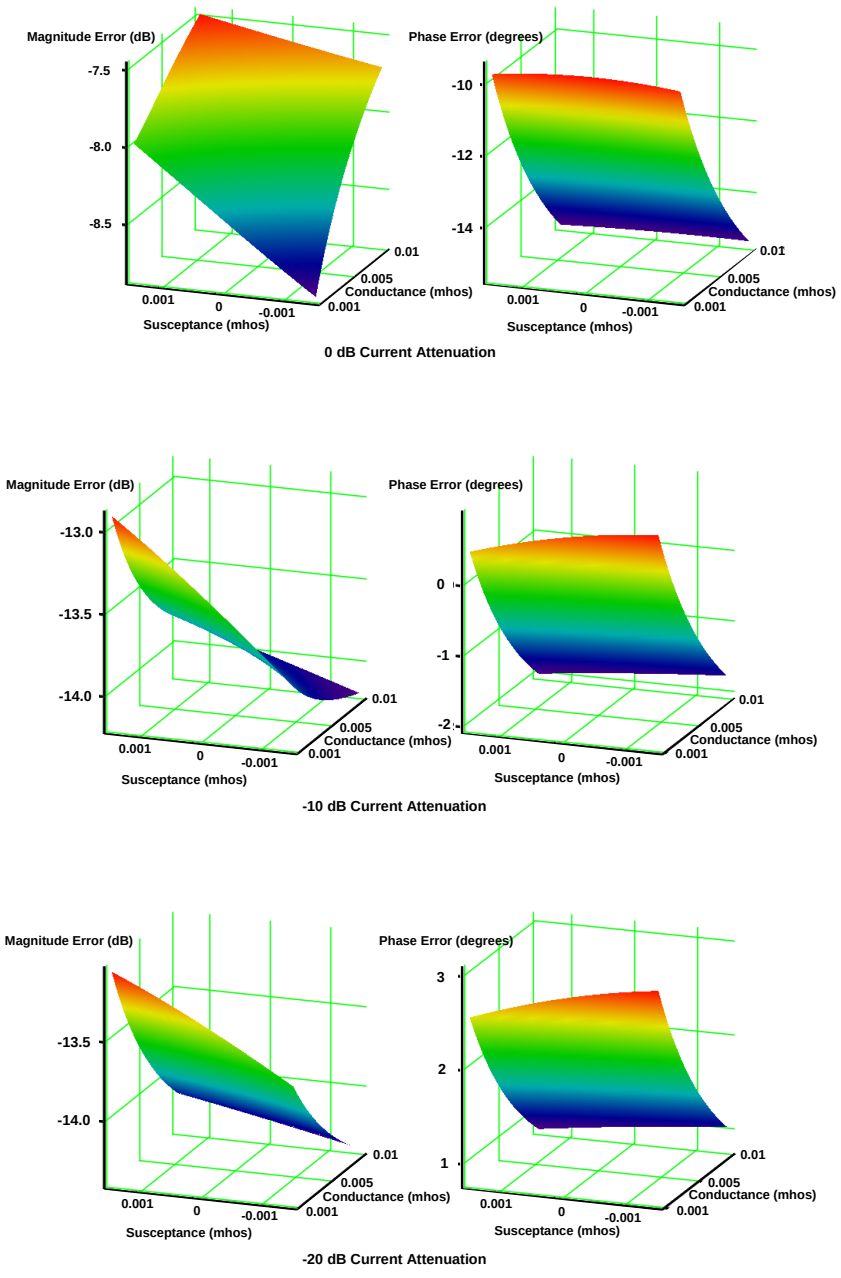

Figure 25: Magnitude and Phase Error of Calibration of Probe Array Element One (Nearest to Plate) with Impedance Loading at Other Elements ($\mathscr{E}_{fs\ calibration}^{Z\ load}$)

Approved for public release; distribution is unlimited.

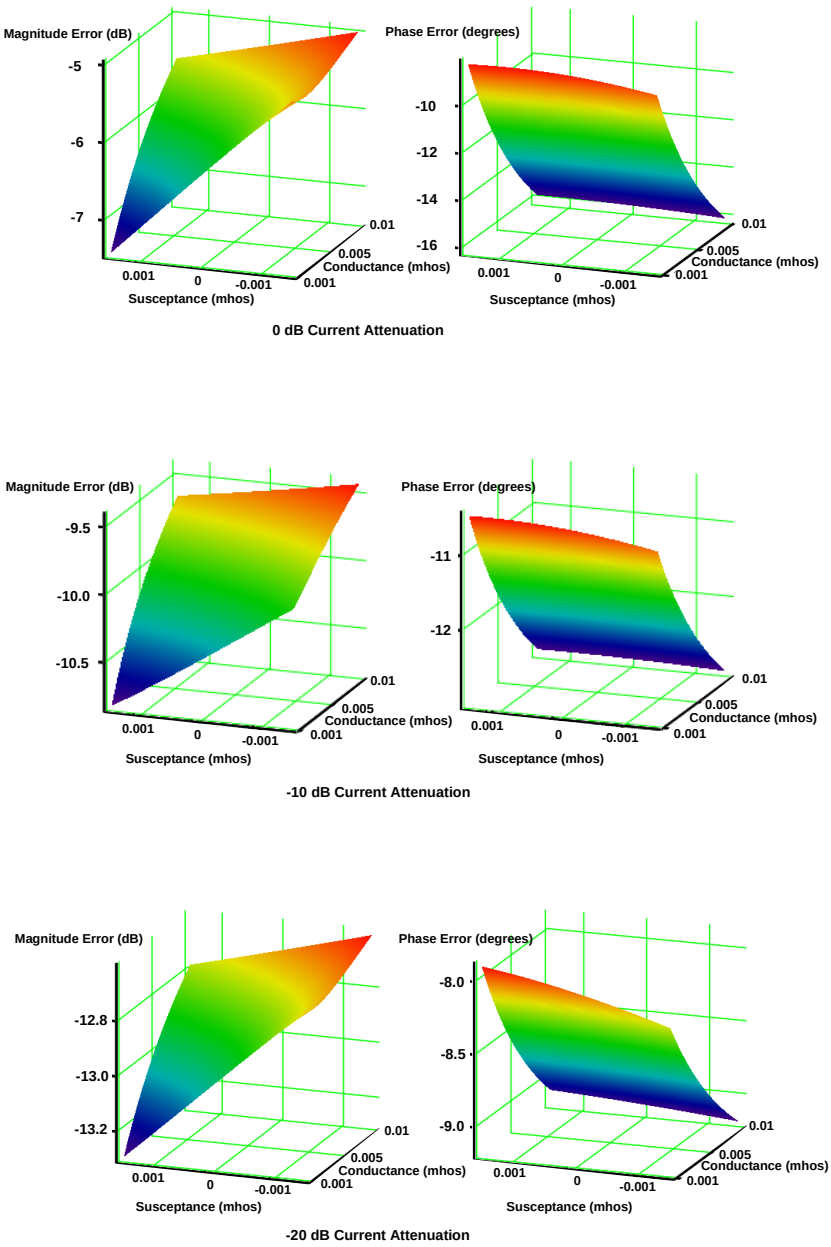

Figure 26: Magnitude and Phase Error of Calibration of Probe Array Element Three with Impedance Loading at Other Elements ($\mathscr{E}^{Z\,load}_{fs\,calibration}$)

Approved for public release; distribution is unlimited.

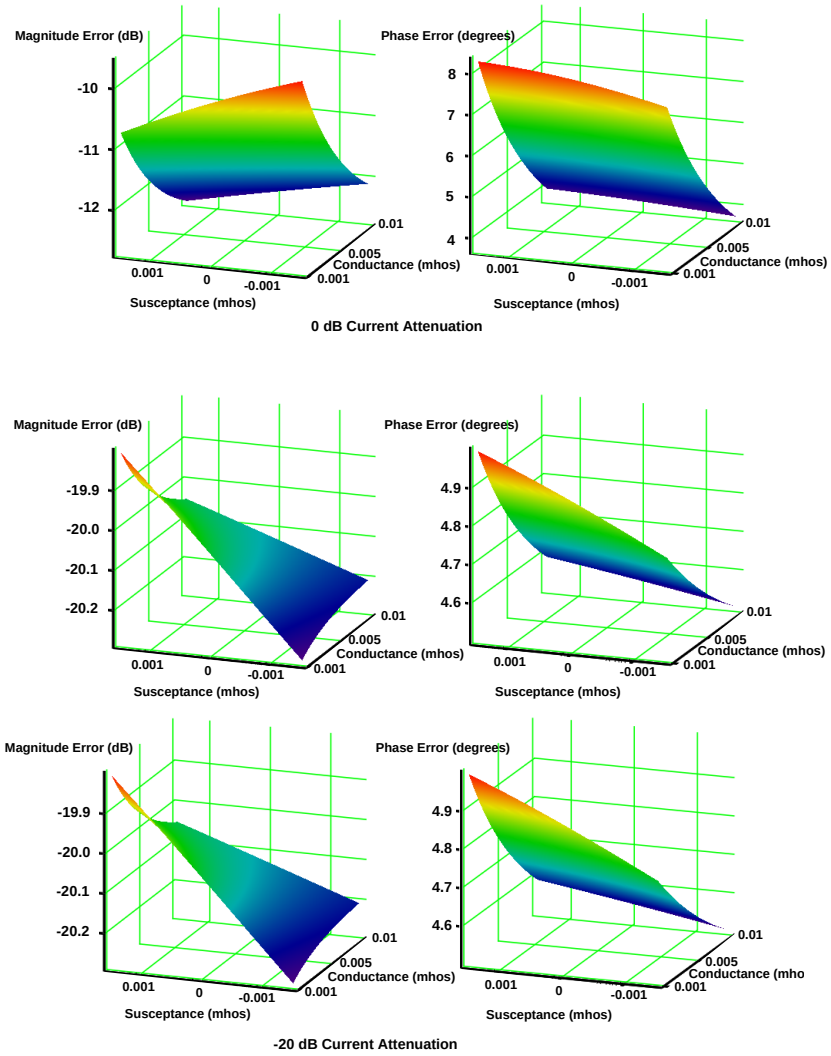

Figure 27: Magnitude and Phase Error of Calibration of Probe Array Element Five (Farthest from Plate) with Impedance Loading at Other Elements ($\mathscr{E}^{Z\ load}_{fs\ calibration}$)

Approved for public release; distribution is unlimited.

We compare these results with the case when the probe array is calibrated with the target present. Figures 28, 29 and 30 show the magnitude of the calibration error, $\mathscr{E}^{Z\,load}_{is\,calibration}$, for probe array elements one (nearest to the plate), three and five (farthest from plate) respectively as a function of the element load susceptance and conductance. Here the probe array self and mutual impedances as well as the mutual impedances between probe array elements and the measurement probe are determined with the target present. Each section of the Figures illustrates the dependence when the impedances employed at the other elements attenuates the element currents by 0 dB, -10 dB, -20 dB,, -40 dB and -60 dB. These load impedances are found from Equation (38) using the in-situ impedances determined by calibration with the target present.

It is important to observe in these Figures that the magnitude of the error decreases monotonically with attenuation in other element currents. This is shown clearly in Table 2 where these results from Figures 18, 19 and 20 are summarized. Comparison of the results in Table 2 for in-situ calibration with those in Table 1 with free space calibration emphasizes an important conclusion. The use of free space calibration limits the minimum calibration error due to differences between in-situ and free space impedances used in the calibration process, even with open circuit load conditions in the probe array elements without the modulating impedance. In-situ calibration provides a minimum calibration error limited only by the quality of current attenuation at the probe array elements without the modulating impedance. Comparison of the magnitude of the calibration error between elements one, three and five for open circuit loading shown in Table 1 seems to indicate that the use of in-situ calibration is of increased importance when the probe array elements are close to the target.

We make a final observation of importance. As noted previously, the load impedances found from Equation (38) to attenuate the currents at the elements without a modulating impedance are not constrained to be realizable as passive loads. In fact, one load required in the in-situ calibration process would have to be an active load. This may be an important consideration in the practical implementation of the modulated scatterer approach with a probe array since the use of an active load implies additional hardware at the position of the probe array and consequently increased interaction between the array and the target or antenna under test.

Table 2: Summary of the Magnitude of Calibration Error with Impedance Loading for In-Situ Calibration

Current Attenuation	Element 1	Element 3	Element 5
0 dB	-12	-7	-11
-10 dB	-18	-18	-20
-20dB	-29	-26	-30
-40 dB	-49	-46	-50
-60 dB	-69	-66	-70

Approved for public release; distribution is unlimited.

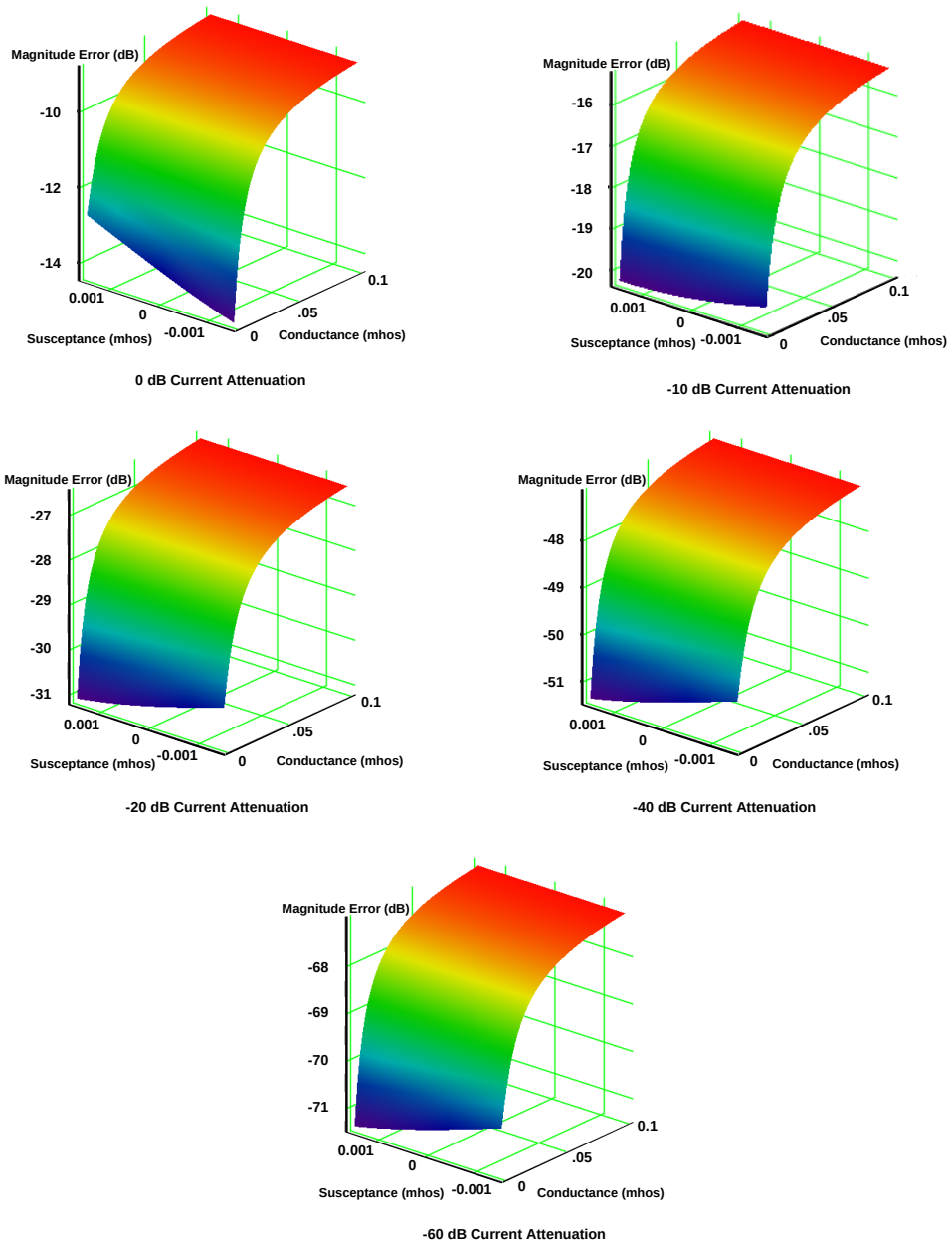

Figure 28: Magnitude of the Calibration Error of Probe Array Element One (Nearest to Plate) with Impedance Loading at Other Elements ($\mathscr{E}_{is\ calibration}^{Z\ load}$)

Approved for public release; distribution is unlimited.

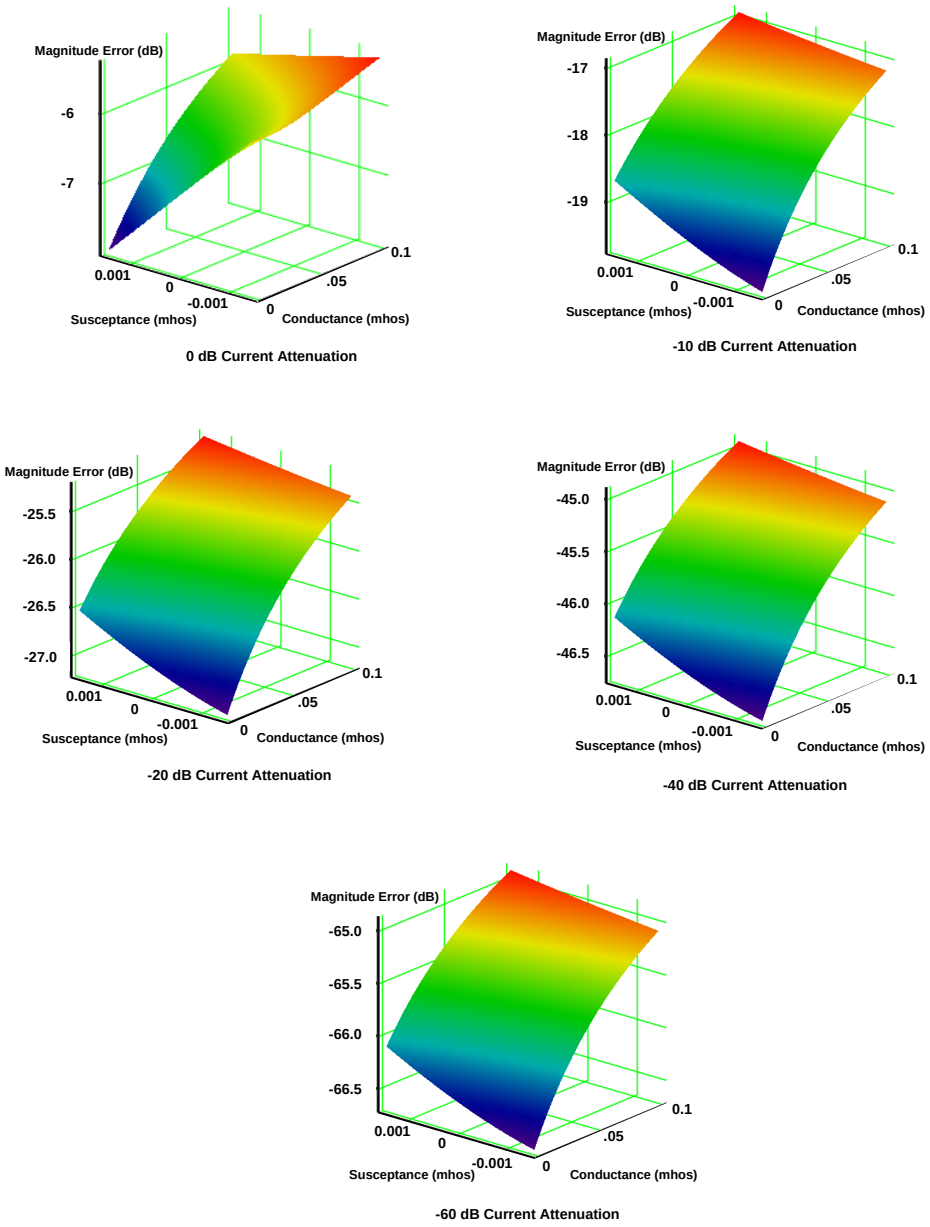

Figure 29: Magnitude of the Calibration Error of Probe Array Element Three with Impedance Loading at Other Elements ($\mathscr{E}_{is\ calibration}^{Z\ load}$)

Approved for public release; distribution is unlimited.

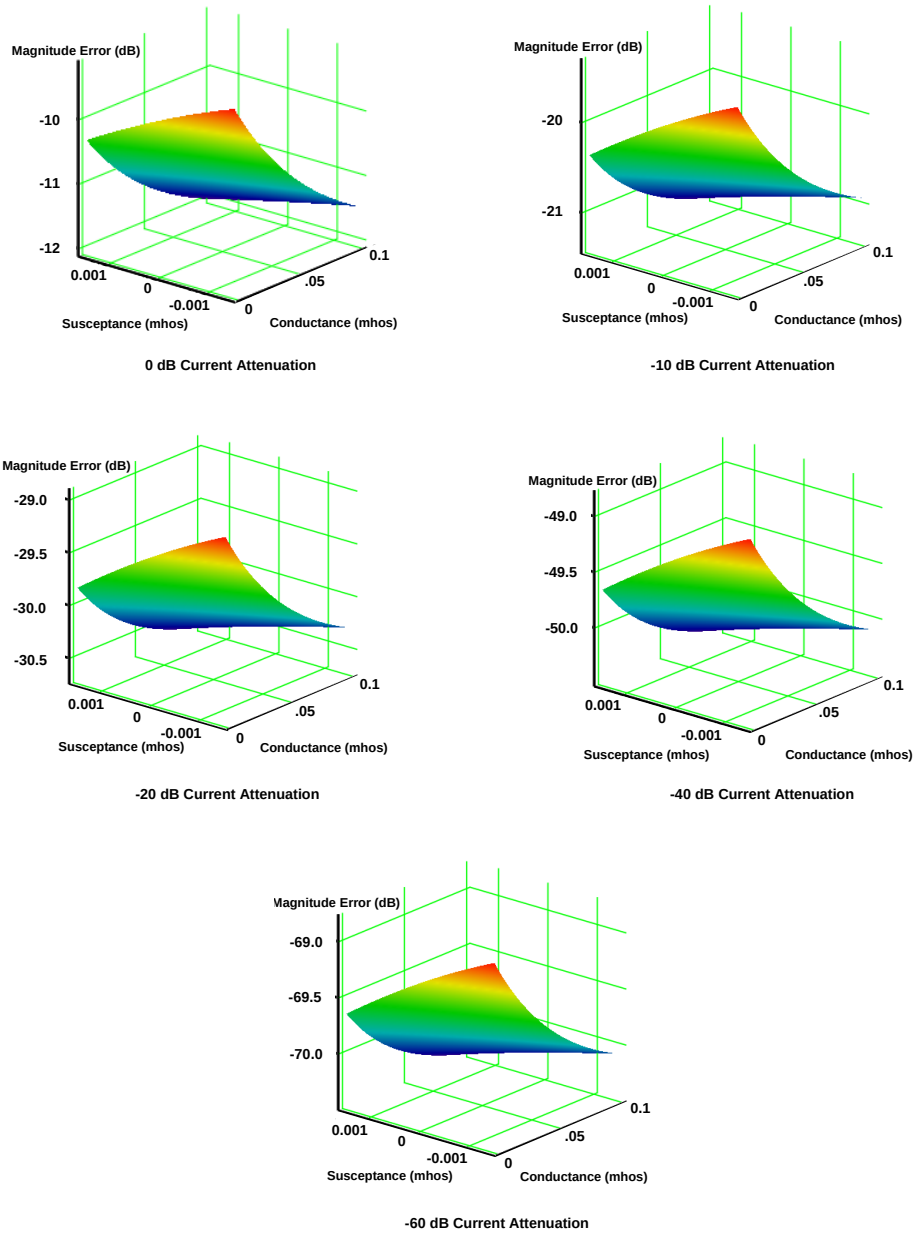

Figure 30: Magnitude of the Calibration Error of Probe Array Element Five (Farthest from the Plate) with Impedance Loading at Other Elements ($\mathscr{E}^{Z\ load}_{is\ calibration}$)

Approved for public release; distribution is unlimited.

3.4 Summary and Conclusions

In this work we modeled the performance of an array of near field probes employing a time varying load impedance at one element of the array. The objective of using the modulated scattering array is to improve the efficiency of obtaining precise measurements of the amplitude and phase of the field scattered by a nearby target when illuminated by a uniform plane wave. The time varying field scattered by the probe array itself is observed at a remote measurement probe such that, with proper calibration, the time varying open circuit voltage at the remote probe is proportional to the required complex valued scattered field at the location of the impedance modulated element. The idea of using the modulated scattering from the probe array is founded on the need to minimize complex measurement circuitry at the probe array, thereby reducing the size of the probe array and minimizing probe array-target interactions which can introduce significant errors in the near field measurements of the scattered field.

Accurate measurements require characterization of the interaction between (1) probe array elements, (2) array elements and the target being measured, and (3) array elements and the remote measurement probe. We characterize these interactions in terms of the self and mutual impedances between array elements and the measurement probe. In general, these impedances depend on the location and orientation of the probe array and measurement probe with respect to the scattering target being measured. These in-situ impedances are key to accurate calibration of the modulated scattering measurment system. The impedance characterization is appropriate since in previous work [29] we related the probe array terminal voltages in this impedance characterization to the fields at the locations of the probe elements using the Lorentz reciprocity theorem.

However, the required use of in-situ impedances implies that the impedances be measured for each location and orientation of the modulated scattering probe array with respect to the scattering target. These impedance measurements slow the near field measurement process and potentially increase errors in the measurements due to the increased size of the probe array which includes now impedance measurement circuitry.

In this work we examined the errors in calibration and measurement that occur when free space impedances are used in lieu of the required in-situ impedances. Using free space impedances improves the efficiency of the near field measurement process since the mutual impedances of the probe array must be measured only once in free space with the target absent. The errors in calibration and measurement were developed from the in-situ or free space, active source impedance characterization of the probe array/measurement probe configuration. This characterization, developed previously [5], augments the conventional passive impedance relationships between probe array terminal voltages and currents by including active, open circuit sources at each terminal to characterize the voltage induced by the external plane wave source and target scattering. The linear impedance equations were solved to provide expressions for the open circuit voltage at the remote measurement probe in terms of the plane wave/target induced voltages and the impedance loads at each probe array elements. This expression was simplified to give the measurement probe voltage when the probe array terminals are loaded with large impedances, providing near open circuit conditions at these terminals. This is an important condition since near open circuit conditions minimize the interaction between the probe array and the target [5] [29] and thus improve the accuracy of the near field measurments. Further, the simplified expression shows that the measured voltage is the linear superposition of the plane wave/target induced voltages at the array terminals and thus errors are introduced in the measurement voltage of a single probe array voltage due to coupling with the other elements of the probe array.

The simplified expressions for the measurement probe voltage were examined physically using a signal flow graph representation for the voltage. The flow graph shows how the mutual impedances between probe array elements introduce errors in the measurement voltage and demonstrates that open circuit conditions at the terminals eliminates the errors.

Approved for public release; distribution is unlimited.

The variation in measurement probe voltage with changes in load impedance at one probe array terminal and with open circuit conditions at the remaining array terminals is most sensitive to load changes when the variable load is near open circuit. This is an important result since (1) the near open circuit condition at all probe array terminals minimizes the interaction between the array and the target and enhances the accuracy of the field measurements and (2) enhanced sensitivity in the measurement voltage to impedance changes increases the accuracy of the measurements. Errors in the measurement probe voltage amplitude and phase were examined when the probe array is calibrated with free space impedances and with in-situ impedances. The baseline for comparison in the error expressions is the measurement probe voltage induced by the scattering from a single, in-situ probe at the location of each of the probe array elements with a variable load impedance to modulate the measured voltage. The errors were found using electromagnetic field computations using NEC4 for the case of a five element dipole probe array in the presence of a flat plate target [5][29]. The array was located in the specular scattering direction of the plate but in the near field of the plate. A remote measurement probe was locate 30 wavelengths from the probe array. The computations revealed the importance of in-situ calibration of probe array elements near the scattering target. With in-situ calibration, the measurement error decreases monotonically with decrease in the probe array terminal currents. The conditions for cancellation of these currents is based on the measurement of in-situ mutual impedances of the probe array. For comparison, the accuracy of the measurements is limited significantly when the free space impedances of the array are used in the calibration, no matter how small the currents at the other terminals of the probe are constrained. We conclude from this example that it will be important for the experimentalist to determine the limits in measurement accuracy associated with the use of free space probe array mutual impedances, especially for probe array elements that are near the target. Should this limiting accuracy be unsatisfactory, the experimental designer must consider the feasibility of in-situ impedance measurements and in-situ calibration of the modulated scattering probe array.

Approved for public release; distribution is unlimited.

4 Preliminary Investigation of Using a Circular Arc Array for Bistatic Near-Field RCS Measurements

4.1 Introduction

The near-field bistatic radar cross section (RCS) measurements discussed in [3] use a parabolic reflector to illuminate the target with a plane wave, measure the scattered near-field of the target, and then compute the corresponding scattered far-field. Two limitations of this approach are:

(1) measuring the field with a single probe is very time consuming, and

(2) the probe cannot be located near the back-scattering directions, i.e. between the illuminator and the target, without creating unacceptable field perturbations.

Our objective here is to explore an alternative approach, where an array of antenna elements is used to illuminate the target and simultaneously measure the scattered near-field. The parallel use of a set of elements would drastically reduce the measurement time and the simultaneous transmit/receive functions would allow measurements of the scattered field with reduced perturbations.

In general, the transmit and receive arrays require different sizes. The transmit array needs only to extend over an arc large enough to provide the plane wave illumination. The receive array usually needs to surround most or all of the target in order to capture enough of the scattered near-field for the subsequent far-field computation.

4.2 Basic Assumptions for the Model

In our approach, for simplicity, we make the following assumptions:

(1) the array and the scatterer lie in the same plane, i.e. we consider a quasi 2-dimensional scattering case,

(2) fields are scalar, corresponding to a single linear polarization,

(3) the array elements can simultaneously transmit and receive,

(4) the array elements are single mode elements.

4.3 Generating the Plane Wave Illumination

The basic measurement set-up is shown in Figure 31, where the array is assumed to extend over a circular arc and the array excitation is such as to generate a plane wave illumination over the target zone, a 2-dimensional circle in the plane of the arc array.

In principle, to generate a plane wave illumination over a 3-dimensional target region requires a transmit array distributed over a 2-dimensional transmit surface. To reproduce this with a linear array would require sequentially positioning the array in locations which cover this transmit surface, and for each location measure the reflected field over the entire recording surface. Thus a 3-dimensional target would require the use of separate linear transmit and receive arrays.

However, in this preliminary study we only consider a single circular arc array, which serves both as transmit and receive array. We choose a circular arc rather than straight line array since near-zone ranges often use circular cylindrical measurement surfaces. The extension to the 3-dimensional case and to other linear arrays is straightforward.

Approved for public release; distribution is unlimited.

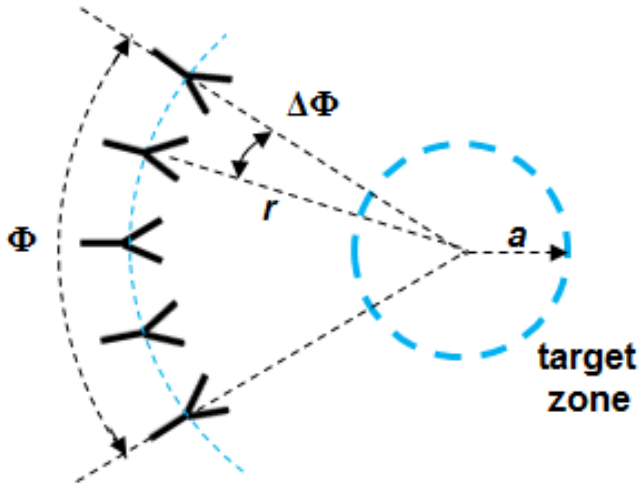

Figure 31: Near-Field Bistatic RCS Measurement Setup where the Circular Arc Array Generates a Plane Wave Illumination over the Target Zone on Transmit and Records the Scattered Near-Field on Receive

It is clear that with the proper array arc Φ, element spacing $\Delta\Phi$, array excitation $\{A_n\}$, and distance r to the target zone, a high quality uniform plane wave can be generated over the target zone. This constitutes a synthesis problem somewhat similar to the well-known antenna pattern synthesis problem.

The appropriate element spacing is most easily estimated by analyzing the array in the receive mode. For our 2-dim. case we consider a cylindrical target of diameter d, in a circular cylindrical target zone of radius $a = d/2$, which we assume large in terms of wavelength $\lambda, a >> \lambda$. Locally the boundary $s = 2\pi a$ of the target zone can be considered essentially planar and thus the radiated field can vary as fast as in free space and must be sampled at free space rate, i.e. 2 samples per wavelength. (Fields with faster variation along a planar surface would be cut-of; along a cylindrical surface they become gradually more evanescent; for a strict mathematical analysis see [35, pp23-29]. This leads to a total number of samples $N_c \approx 2s/\lambda = 4\pi a/\lambda$ and a corresponding angular sample spacing

$$\Delta\Phi_c = 2\pi/N_c \approx \lambda/2a \tag{39}$$

This angular spacing $\Delta\Phi_c$ is the proper element spacing for a circular receive array. We use this spacing also for an array on an arc of angle Φ which thus will have a number of elements $N \approx \Phi/\Delta\Phi_c$. The angular frequency content of the outgoing cylindrical wave does not change with radial distance and therefore the field may be sampled with the same number of points at any radius. In applications the number of sampling points is sometimes chosen slightly larger than $\Phi/\Delta\Phi_c$, since the transition from propagating to evanescent waves is gradual.

The above discussed sampling of the scattered field from the target, i.e. the array in the receive mode. Due to reciprocity the same angular array element spacing applies also for the transmit mode, where the array illuminates the target. Choosing a tighter element spacing than $\Delta\Phi_c = \lambda/2a$ is tantamount to generating angular frequency components on the cylinder surface which vary faster than the free space wavelength. This is similar to superdirectivity in the planar case and is associated with array excitations with extremely high amplitude, as shown in the example below.

The field E radiated by the array is

$$E_m = \sum_{n=1}^{N} A_n \frac{e^{-jkr_{mn}}}{kr_{mn}} \tag{40}$$

Approved for public release; distribution is unlimited.

Table 3: Target Illumination Error vs. Element Density in the Illuminating Array

array radius r(λ)	**array arc angle Φ (deg.)**	element spacing (deg.)	number of elements N	max. excitation coeff. $\|A_n\|$	rms illumination error
800	**--**	--	1	$5.0\ 10^3$	0.103
800	**30**	3.0	11	$5.0\ 10^3$	0.010
800	**30**	1.5	21	$7.5\ 10^4$	0.003
800	**30**	0.75	41	$1.8\ 10^{12}$	0.003

where A_n denotes the complex excitation of element n, k the wave number, and r_{mn} the distance from element n to the field point m. A simple approach to determine an appropriate array excitation is to assume a fixed array geometry and equate the radiated field E to the desired plane wave values E_{dm} at a large number of sample points over the target zone, i.e.

$$E_{dm} = \sum_{n=1}^{N} A_n \frac{e^{-jkr_{mn}}}{kr_{mn}}, \qquad m = 1,\ ...,\ N > N \tag{41}$$

This leads to an over determined system of equations from which an array excitation $\{A_n\}$ that provides the best least-mean-square approximation can be conveniently solved. Since we want to generate an incident plane wave of amplitude E_0 over the target region we set $|E_{dm}| = E_0$ and the phase of E_{dm} equal to the desired plane wave phase at the sampling point m. A corresponding computer code has been implemented and a few numerical examples are given below and in Section 4.5 and Appendix E.

The examples considered in this section illustrate the effects of element spacings less than $\lambda/2a$. We choose a target zone of $2a = 20\lambda$, with a corresponding element spacing $\Delta\Phi_c = \lambda/2a \approx 3^o$. In our first example we use a uniformly spaced array with 11 elements which thus spans an arc $\Phi_a = 30^o$. We then populate the same arc with 21 elements, which have a spacing $1/2\Delta\Phi_c$, and finally we populate it with 41 elements spaced at $1/4\Delta\Phi_c$.

The computed maximum values $|A_n|_{max}$ of the excitation coefficients for the three different cases are shown in Table 3, along with the synthesized field rms error ϵ_{rms} over the target zone. This error is defined as

$$\epsilon_{rms} = \frac{1}{M}\sqrt{\sum_m |\frac{E_m - E_{dm}}{E_0}|^2}, m = 1, ..., M \gg N \tag{42}$$

where E_m is given by (40). The single element 'array' is included as a reference in the Table. The range was set $r = 2d^2/\lambda = 800\lambda$, which is the normal RCS far field measurement distance, and the target zone was sampled with $\lambda/2$ spacing in the x- and y-directions, which leads to a system of about $\pi(21 \times 21/4)$ equations for the array excitation coefficients A_n.

The array excitation becomes excessive when the angular spacing is $1/2\Delta\Phi_c$ and it increases by an absurd factor 10^7 when it becomes $1/4\Delta\Phi_c$, since we are using evanescent spatial components. We also note that the larger number of array elements does not significantly reduce the already small illumination error.

A plot of the relative illumination error

$$\epsilon_{rel} = \frac{|E - E_{planewave}|}{|E_{planewave|}} \times sign(|E| - |E_{planewave}|) \tag{43}$$

Approved for public release; distribution is unlimited.

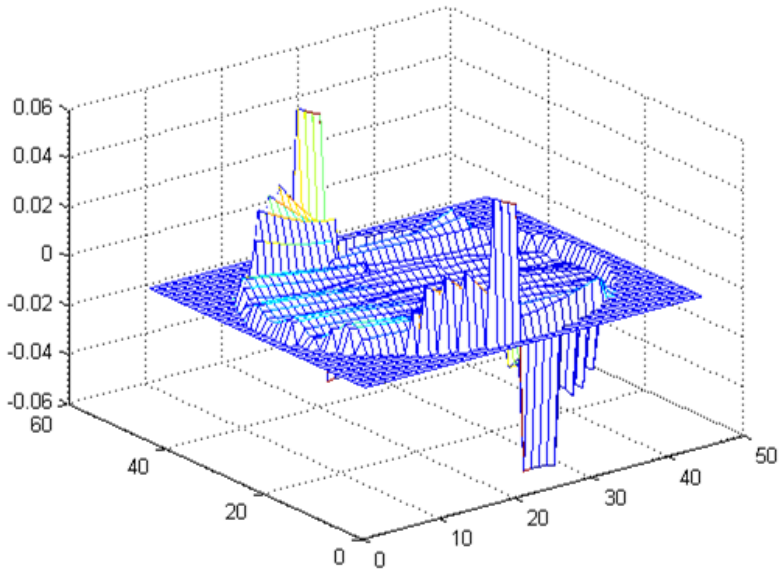

Figure 32: The Relative Illumination Error over a Target Zone of $d = 20\lambda$, When Illuminated by an 11-Element Array from a Distance $r = 800\lambda$

over the target region for the 11 element array is shown in Figure 32. Further examples are given in Section 4.5. They show that a certain minimum array-target distance is required to achieve an adequate plane wave illumination. Extending the angular extent of the array is not effective, since eventually the illumination comes from the wrong directions. In this respect the arc array is inherently different from a straight linear array, which with proper size can generate a perfect plane wave at very close range.
In the above approach the mean square error was minimized over the target zone. There are more sophisticated pattern synthesis methods, e.g. 'alternating projections' [30], which can provide local control over the approximation error, and might be worthwhile applying to our case in the future.

A complication in synthesizing the proper array excitation is that the array element patterns are affected by mutual coupling, which was ignored above. However, as shown in Appendix A, the mutual coupling effects can be accounted for and compensated by an appropriate complex matrix pre-multiplication of the array excitation.

4.4 Measuring the Scattered Near Field

The array elements, which illuminate the RCS target, can simultaneously be used in the receive mode to sample the scattered near-field from the target. A complication is that these probe elements in turn scatter some of the field incident on them, which perturbs the field received by neighboring array elements and sets up a standing wave between the array and the target.

In the following we derive an approach to evaluate and correct for this mutual coupling in the array and the array-target interaction.

Our N-element array, either in the presence or the absence of a target, can be represented by an N-port network. In view of the linearity of the network the voltages V_n and currents I_n at the ports can be related

by an impedance matrix $\mathbf{Z}$ as

$$\begin{pmatrix} V_1 \\ \vdots \\ V_N \end{pmatrix} = \begin{pmatrix} . & . & . \\ . & Z_{mn} & . \\ . & . & . \end{pmatrix} \begin{pmatrix} I_1 \\ \vdots \\ I_N \end{pmatrix} \tag{44}$$

or, in vector form

$$\mathbf{v} = \mathbf{Zi} \tag{45}$$

The impedance Z_{mn} is defined as the open-circuit voltage V_n induced on element n by the current I_m at port m, while the currents at all other ports are equal to zero,

$$Z_{mn} = \frac{V_n}{I_m}, \qquad \{I_\mu\}_{\mu=1}^{N} = 0,\ \mu \neq m \tag{46}$$

An expression for $V_{nm} = Z_{nm} I_m$ applicable for a line element of length l is given in [32, p.414]

$$V_{nm} = \frac{-1}{I_n(0)} \int_{-l/2}^{l/2} E_{nm}(z) I(z) dz \tag{47}$$

where E_{nm} is the E-field component radiated by element m, which is parallel to n, and $I_n(z)$ is the current distribution along element n. In the induced emf method, which we will use, this current distribution is assumed known. We note that when the field can be considered constant over the element, $E_{nm}(z) \approx E_{nm}$, then

$$V_{nm} \approx E_{nm} \left[\frac{-1}{I_n(0)} \int_{-l/2}^{l/2} I_n(z) dz \right] \tag{48}$$

i.e. V_{nm} is directly proportional to the E-field at element n. The term in the bracket is the so called effective length of the antenna.

By definition the open-circuit voltage V_{nm} represents the incident E-field at element n due solely to the current I_m at port m, while all other currents $I_n = 0, n \neq m$. For the case of an array and a RCS target, physically this means that all the other elements are absent (since we assume single-mode elements) and thus there is no interaction between the array elements or between the array and the RCS target. As a consequence, the voltages $\mathbf{v} = \mathbf{Zi}$ represent the E-field that would be received at the array, due to the currents $\mathbf{i}$, in the absence of any array mutual coupling or array-target interaction, and thus v represents our desired sampled near-field. The key thus is the determination of the impedance matrix $\mathbf{Z}$.

When a target is present there are two contributions to the field E_{nm} at element n. One contribution E^a_{nm} is the direct radiation from array element m, the other contribution E^t_{nm} is the target reflection, see Figure 33. Thus we have

$$E_{nm} = E^a_{nm} + E^t_{nm} \tag{49}$$

which leads to

$$Z^{a+t}_{nm} = Z^a_{nm} + Z^t_{nm} = -\frac{1}{I_n(0) I_n(0)} \int_{-l/2}^{l/2} E^a_{nm} I_n(z) dz - \frac{1}{I_n(0) I_n(0)} \int_{-l/2}^{l/2} E^t_{nm} I_n(z) dz \tag{50}$$

Explicit expressions for the impedances Z^a_{nm} and Z^t_{nm} are derived in Appendices B and C. In the following we need to consider the two alternative impedance matrices

$$\mathbf{Z^a} \qquad \text{for the single array in free space,} \tag{51}$$

$$\mathbf{Z}^{a+t} \quad = Za + Zt \quad \text{when the target is present.} \tag{52}$$

The mutual impedance matrix $\mathbf{Z}$ is complicated to measure directly, since it assumes null currents on the elements. However, it can be derived from the scattering matrix, which can be measured.

Approved for public release; distribution is unlimited.

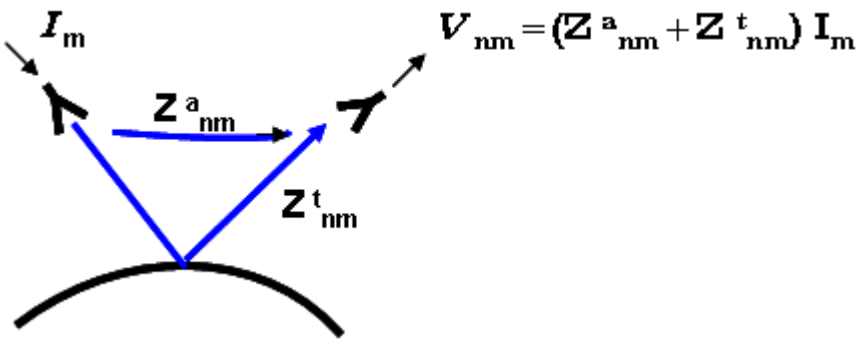

Figure 33: The Current I_m at Element m Induces an Open-Circuit Voltage V_{nm} at Element n

In practical arrays the elements are fed by transmission lines, and we measure the scattering matrix S which relates the incident and reflected waves on these lines. (There will now be induced currents on the elements, since they are not open-circuited, and these currents reradiate and cause undesired perturbations). Denoting the line impedance by Z_0, the incident voltages and currents by V_n^i and I_n^i, and the reflected voltages and currents by V_n^r and I_n^r, we have

$$\mathbf{v}^r = \mathbf{S}\mathbf{v}^i \tag{53}$$

Furthermore, we have

$$\begin{aligned} \mathbf{v}^i &= Z_0\mathbf{i}^i \\ \mathbf{v}^r &= Z_0\mathbf{i}^r \\ \mathbf{v} &= \mathbf{v}^i + \mathbf{v}^r \\ \mathbf{i} &= \mathbf{i}^i - \mathbf{i}^r \end{aligned} \tag{54}$$

which, when substituted in (53), leads to the usual relation between the scattering and impedance matrices

$$\mathbf{S} = (\mathbf{Z} + Z_0\mathbf{I})^{-1}(\mathbf{Z} - Z_0\mathbf{I}) \tag{55}$$

or

$$\mathbf{Z} = Z_0(\mathbf{I} + \mathbf{S})(\mathbf{I} - \mathbf{S})^{-1} \tag{56}$$

where $\mathbf{I}$ denotes the identity matrix. Using the relations (53) and (56) eventually lets us determine the desired mutual impedance matrix $\mathbf{Z}^t$, as shown below.

The matrix $\mathbf{S}$ cannot be directly solved from (53) since, for an N-element array, (53) represents only N linear equations, whereas $\mathbf{S}$ contains on the order of N^2 unknowns. However, by making measurements of $\mathbf{v}^r$ with N linearly independent array excitations $\mathbf{v}^i$ we can obtain N^2 equations from which the matrix coefficients in $\mathbf{S}$ can be solved. We form the matrices

$$\mathbf{V}^i = (\mathbf{v}_1^i,\ ...,\ \mathbf{v}_N^i) \tag{57}$$

$$\mathbf{V}^r = (\mathbf{v}_1^r,\ ...,\ \mathbf{v}_N^r) \tag{58}$$

Approved for public release; distribution is unlimited.

where $\mathbf{v}_n^r$ denotes the response to the excitation $\mathbf{v}_n^i$, substitute $\mathbf{V}^i$ and $\mathbf{V}^r$ for $\mathbf{v}^i$ and $\mathbf{v}^r$ in (53) and so obtain the desired scattering matrix

$$\mathbf{S} = \mathbf{V}^r(\mathbf{V}^i)^{-1} \tag{59}$$

Two sets of measurements are required: one for the scattering matrix $\mathbf{S}^a$ corresponding to the array only, and one for the scattering matrix $\mathbf{S}^{a+t}$ corresponding to the array + target, from which we determine the impedance matrices $\mathbf{Z}^a$ and $\mathbf{Z}^{a+t}$. Since

$$\mathbf{Z}^{a+t} = \mathbf{Z}^a + \mathbf{Z}^t \tag{60}$$

we obtain

$$\mathbf{Z}^t = \mathbf{Z}^{a+t} - \mathbf{Z}^a = Z_o\left[(\mathbf{I}+\mathbf{S}^{a+t})(\mathbf{I}-\mathbf{S}^{a+t})^{-1} - (\mathbf{I}+\mathbf{S}^a)(\mathbf{I}-\mathbf{S}^a)^{-1}\right] \tag{61}$$

which reduces to

$$\mathbf{Z}^t = 2Z_o\left[(\mathbf{I}-\mathbf{S}^{a+t})^{-1} - (\mathbf{I}-\mathbf{S}^a)^{-1}\right] \tag{62}$$

The desired samples of the E-field reflected from the target are thus obtained as

$$\mathbf{v}^t = \mathbf{Z}^t\,\mathbf{i}^i_{planewave} \tag{63}$$

where $\mathbf{i}^i_{plane\ wave}$ is the array excitation $\{A_n\}$ determined in Section 4.3, corresponding to a plane wave illumination of the target zone, and an array with impedance matched elements and no mutual coupling, and $\mathbf{Z}^t$ is given by (62). The matrix $\mathbf{S}^a$ (and $\mathbf{Z}^a$) is fixed for a given array and for each RCS target therefore only one new measurement of the scattering matrix $\mathbf{S}^{a+t}$ is required.

An alternative approach is outlined by Schindler [5] who considers a receive array with an incident plane wave. It leads to a convenient expression for the desired scattered field when the array/target interaction can be ignored.

The voltages at the array terminals are

$$\mathbf{v}_{terminal} = \mathbf{v}_{induced} + \mathbf{Z}\,\mathbf{i} \tag{64}$$

where $\mathbf{v}_{terminal}$ denotes the open-circuit voltages induced by the incident field, $\mathbf{Z}$ the array mutual impedance matrix and $\mathbf{i}$ the currents on the elements. (Note the currents here are those induced by the incident field, not the total currents used earlier in this section). Furthermore,

$$\mathbf{v}_{terminal} = -Z_0\mathbf{i} = -\mathbf{v}_{measured} \tag{65}$$

since we assume matched impedance loads Z_0 at each terminal, and the negative sign accounts for the current flowing out from the element. This leads to

$$\mathbf{v}_{induced} = -Z_0\mathbf{i} - \mathbf{Z}\mathbf{i} = -\left(\mathbf{I} + \frac{1}{Z_0}\mathbf{Z}\right)\mathbf{v}_{measured} \tag{66}$$

Applying (66) to our case of scattering from the RCS target we have

$$\mathbf{v}^{a+t}_{induced} = -\left(\mathbf{I} + \frac{1}{Z_0}\mathbf{Z}^{a+t}\right)\mathbf{v}^{a+t}_{measured} \tag{67}$$

where $\mathbf{v}^{a+t}_{induced}$ are the voltages induced by the total field, which is composed of the direct field from the transmit array and the backscattered field from the target. Expressing $\mathbf{v}^{a+t}_{induced}$ in terms of the corresponding components

$$\mathbf{v}^{a+t}_{induced} = \mathbf{v}^{a}_{induced} + \mathbf{v}^{t}_{induced} \tag{68}$$

and performing a second measurement in the absence of the target finally leads to

$$\mathbf{v}^{t}_{induced} = \mathbf{v}^{a+t}_{induced} - \mathbf{v}^{a}_{induced} = -\left(\mathbf{I} + \frac{1}{Z_0}\mathbf{Z}^{a+t}\right)\mathbf{v}^{a+t}_{measured} + \left(\mathbf{I} + \frac{1}{Z_0}\mathbf{Z}^{a}\right)\mathbf{v}^{a}_{measured} \tag{69}$$

The vector $\mathbf{v}^t_{induced}$ represents the desired open-circuit voltages, which are corrected for array/target interaction and are proportional to the field scattered from the target. We note that even with this approach both $\mathbf{Z}^a$ and $\mathbf{Z}^{a+t}$ are required and thus an RCS measurement involves measuring the $N \times N$ matrix $\mathbf{Z}^{a+t}$ (since $\mathbf{Z}^a$ and $\mathbf{v}^a_{measured}$ are constants independent of the target).

Approved for public release; distribution is unlimited.

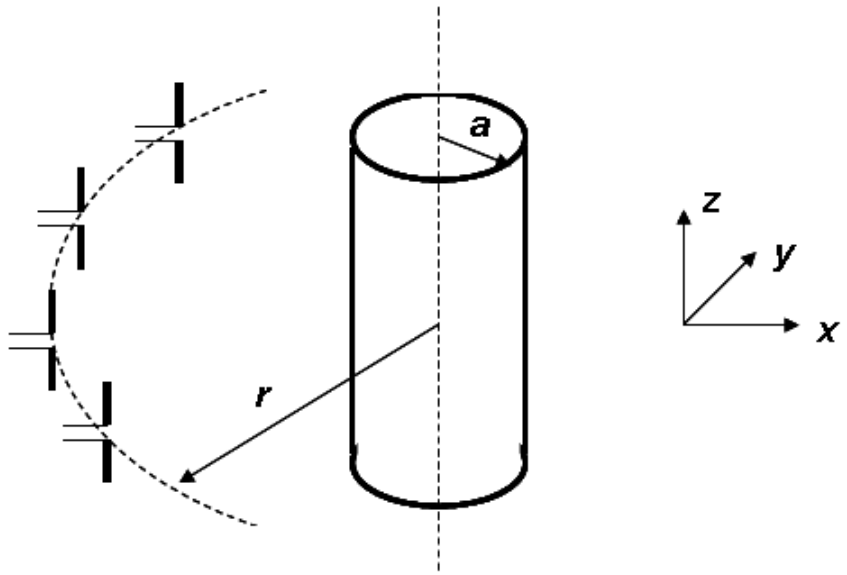

Figure 34: Circular Arc Array with Dipole Elements and RCS Target, an Infinite Circular Cylinder

When the array/target interaction can be ignored we obtain

$$\mathbf{Z}^{a+t} = \mathbf{Z}^{a} \tag{70}$$

and

$$\mathbf{v}^{t}_{induced} = -\left(\mathbf{I} + \frac{1}{Z_0}\mathbf{Z}^{a}\right)\left(\mathbf{v}^{a+t}_{measured} - \mathbf{v}^{a}_{induced}\right) \tag{71}$$

Thus in this case we only need to measure the N-dimensional vector $\mathbf{v}^{a+t}_{measured}$ for each new RCS case, rather than the $N \times N$ scattering matrix $\mathbf{S}^{a+t}$.

4.5 An Example: Circular Probe Array and Cylinder Target

In this section we consider a circular arc array of vertical dipole elements and a target represented by an infinite conducting circular cylinder, which is perpendicular to the plane of the arc array, see Figure 34. We analyze the incident and scattered fields only in the plane of the array, i.e. the xy-plane, and our 'target region' corresponds to a 2-dimensional circle in this plane. The dipoles are assumed to have length $\lambda/2$ and to be matched to the feed line.

On transmit this will demonstrate how well we can realize uniform plane wave incidence over the target region and show the difference in target illumination with and without correction of the array excitation perturbations caused by array mutual coupling.

On receive we demonstrate the effect of the coupling in the probe array and between the array and the target by comparing coupling-perturbed and coupling-corrected samples of the scattered field with the ideal single probe sample that would be received with an ideal plane wave illumination of the target.

4.5.1 Array Pattern Synthesis for Plane Wave Target Illumination

We consider an array along a circular arc of radius r and determine an array excitation which generates a plane wave illumination over a concentric circular target zone of diameter $d = 20\lambda$, cf Figure 31. This

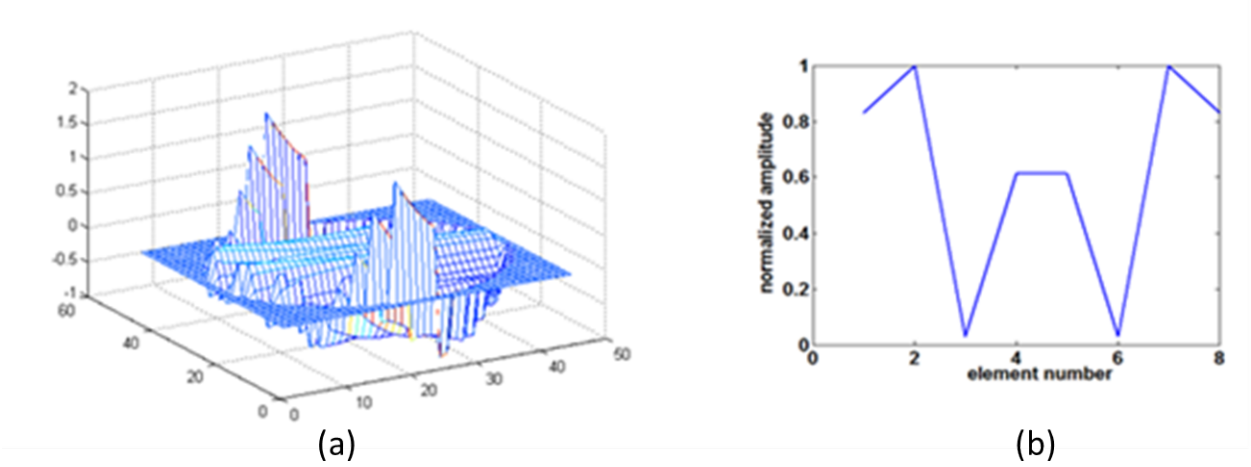

Figure 35: (a) Relative Illumination Error Over a 20λ Diameter Target Region by an Array with $N = 8$ Elements, Arc Angle $\Phi = 15^o$, Radius $r = 40\lambda$ (b) Normalized Array Excitation for the 8-Element Array

target region corresponds to an angular array element spacing $\Delta\Phi_c = \lambda/d \approx 3^o$, as given by (39). The array excitation is determined by matching, in a LMS sense, the desired plane wave illumination over the target zone, sampled at $\lambda/2$ intervals, i.e. ≈ 350 uniformly distributed sample points, as discussed in Section 4.4. In a first example we choose an arc array with angle $\Phi = 15^o$ and radius $r = 40\lambda$. Distributing N=8 elements uniformly over this arc leads to an inter-element spacing $\Delta = \Phi/(N-1) = 2.1^o$, i.e. an element spacing about 30% less than $\Delta\Phi_c = 3^o$.

The resulting illumination error over the target region is shown in Figure 35a, and the corresponding array excitation $\{A_n\}$ is shown in Figure 35b. The rms illumination error $\epsilon_{rms} = 0.37$ in this case, but we note that the relative error $\epsilon_{rel} = 1.8$ is considerably higher, since our approximation is in the LMS sense. The array excitation, which has been normalized to the maximum coefficient $|A_n|_{max} = 230$, varies wildly, possibly because we are slightly into the 'superdirective' region.

In a second example we increase the array arc to an angle $\Phi = 30^o$ and the element number $N = 15$, while keeping the angular spacing $\Delta\Phi = 2.1^o$ and the radius $r = 40\lambda$. The resultant relative target illumination error and synthesized array excitation $\{A_n\}$ are shown in Figure 36 (a) and (b). Both the rms error and the relative error of the illumination have decreased significantly, they are now $\epsilon_{rms} = 0.07$ and $\epsilon_{rel} = 0.15$, respectively. The array excitation, which has been normalized to the maximum coefficient $|A_n|_{max} = 690$, is more tapered, presumably because the far out elements contribute from increasingly wrong directions. Since the target zone is in the near field of the array it is not illuminated by a normal antenna main beam. Figure 36(c) shows the field magnitude over a $60\lambda \times 60\lambda$ square, which is centered on the 20λ diameter circular target zone. We note that there are distinct ridges of high field intensity on either side of the target, before the field decreases with distance from the array. Figure 36(d) illustrates the geometry of the array and the target zone relative to these ridges.

In a third example we increase the array arc to $\Phi = 60^o$, and the element number to $N = 29$, while again keeping the angular element spacing $\Delta\Phi = 2.1^o$ and the radius $r = 40\lambda$ unchanged. The resultant target region illumination and synthesized array excitation $\{A_n\}$ are shown in Figure 37. We note the target illumination errors $\epsilon_{rms} = 0.07$ and $\epsilon_{rel} = 0.14$ have not decreased, but are the same as the error obtained by the smaller array with half the size and half the number of elements. The array excitation, which has been normalized to the maximum coefficient $|A_n|_{max} = 220$, again fluctuates wildly. However, the amplitudes are reasonable and the phases of the excitation coefficients do not alternate by 180° as often occurs in superdirective arrays.

Approved for public release; distribution is unlimited.

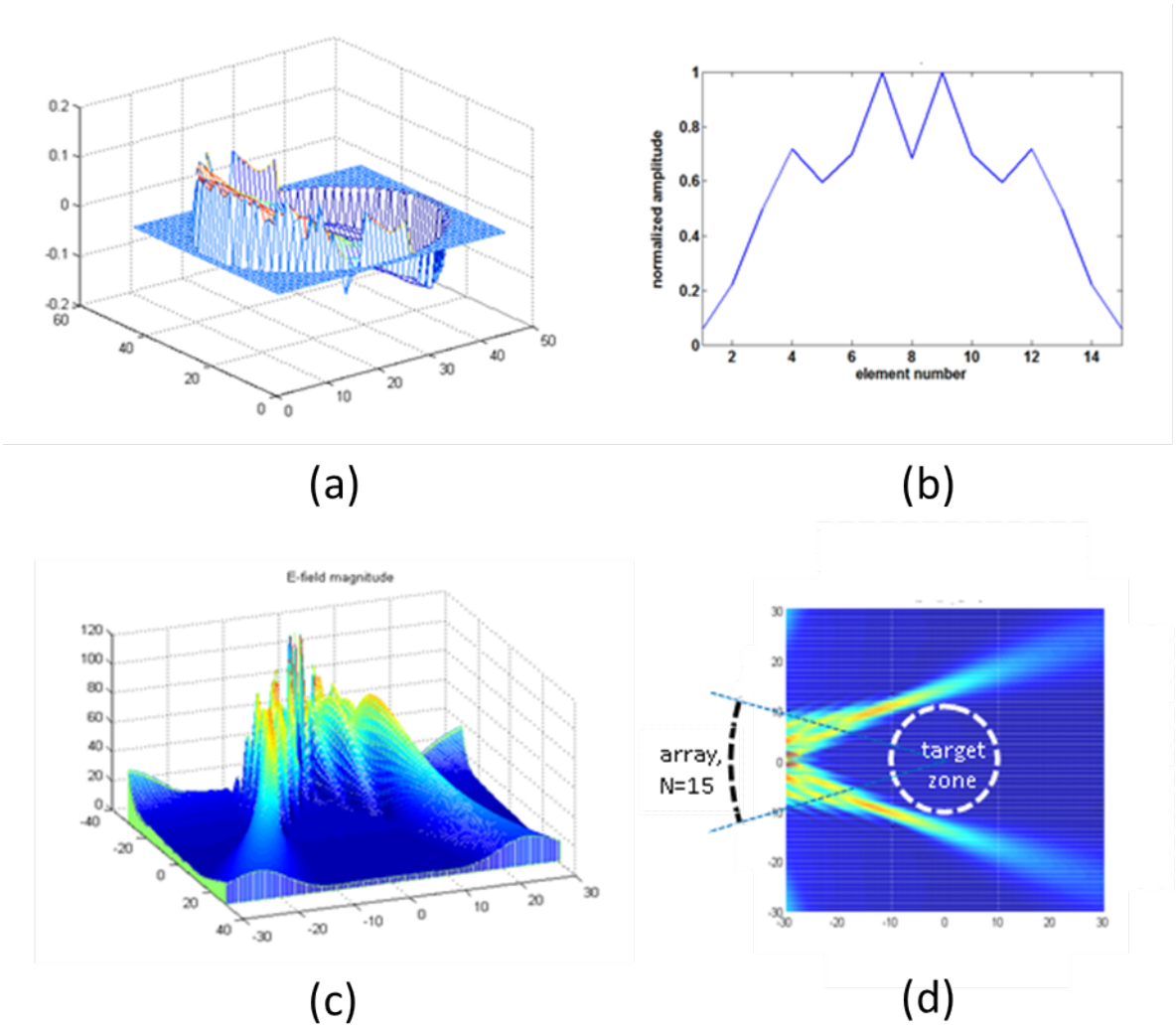

Figure 36: (a) Relative Illumination Error Over a 20λ Diameter Target Region by an Array with $N = 15$ Elements Arc Angle $\Phi = 30^o$, Radius $r = 40\lambda$ (b) Normalized Array Excitation for the 15-Element Array (c) Field Magnitude in the Vicinity of the 20λ Diameter Circular Target Zone (d) Location of the Target Zone Relative to the Two Ridges of High Radiation Intensity.

Approved for public release; distribution is unlimited.

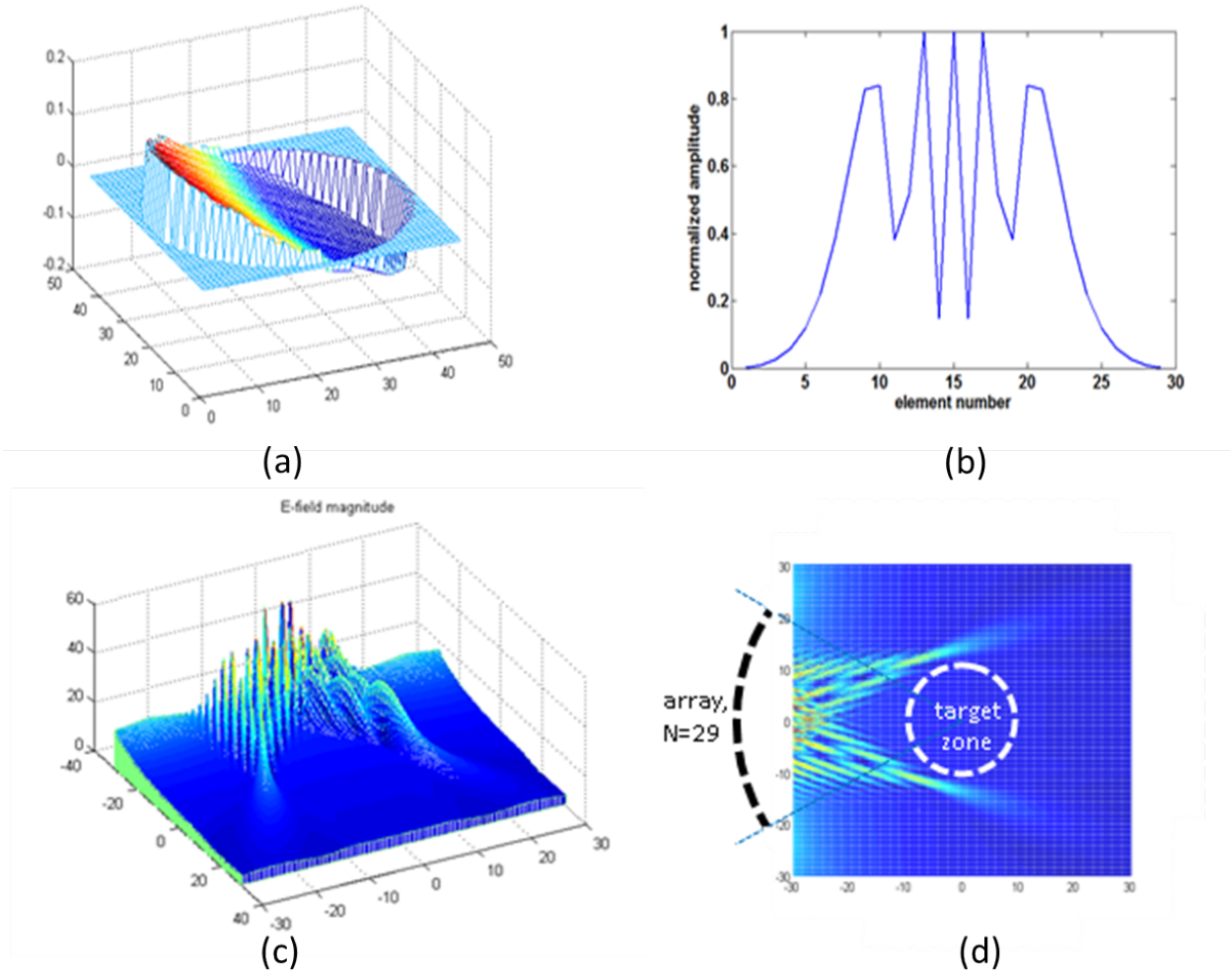

Figure 37: (a) Relative Illumination Error Over a 20λ Diameter Target Region by an Array with $N = 29$ Elements, Arc Angle $\Phi = 60^o$, Radius $r = 40\lambda$ (b) Normalized Array Excitation for the 29-Element Array (c) Field Magnitude in the Vicinity of the 20λ Diameter Circular Target Zone (d) Location of the Target Zone Relative to the Near-Zone Radiation Pattern of the Array

Approved for public release; distribution is unlimited.

Table 4: Maximum RMS Error in Plane Wave Illumination over a 20λ Target Zone for Various Array Geometries

Array Arc Φ (deg.)	Element Spacing $\Delta\Phi$ (deg.)	Number Elements N	Array Radius $r = 20\lambda$		Array Radius $r = 40\lambda$		Array Radius $r = 80\lambda$	
			rms. error	max $\|A_n\|$	rms error	max $\|A_n\|$	rms error	max $\|A_n\|$
15	3.0	6	0.78	29	0.49	91	0.29	250
15	2.1	8	0.77	37	0.37	130	0.07	240
15	1.5	11	0.72	$1.4\ 10^4$	0.11	$2.3\ 10^4$	0.03	3500
30	3.0	11	0.58	28	0.21	94	0.10	270
30	2.1	15	0.46	780	0.07	310	0.03	260
30	1.5	21	0.21	$5.1\ 10^6$	0.06	$8.5\ 10^4$	0.03	$5.6\ 10^4$
60	3.0	21	0.24	29	0.14	96	0.08	270
60	2.1	29	0.14	810	0.07	110	0.03	270
60	1.5	41	0.14	$1.6\ 10^9$	0.07	$9.1\ 10^8$	0.03	$6.8\ 10^8$

A summary of various array sizes Φ and distances r to the target region, and the resulting illumination rms errors is given in Table 4. The target zone, a circle of diameter 20λ was kept fixed. The largest distance (array radius $r = 80\lambda$) corresponds to $1/10$ the normal distance $2d^2/\lambda$ used for RCS far field measurements.

The array arcs Φ are multiples of the nominal element spacing $\Delta\Phi_c = 3^o$. For each arc we started with this element spacing, i.e. an element number $N = \Phi/\Delta\Phi_c + 1$, and then populated the arcs more densely with elements corresponding to the spacings $\Delta\Phi \approx 0.7\Delta\Phi_c = 2.1^o$ and $\Delta\Phi = 0.5\Delta\Phi_c = 1.5^o$.

The results show that for each array size Φ and array radius r, the illumination error converges toward a fixed value with decreasing element spacing $\Delta\Phi$, and it reaches this when $\Delta\Phi \approx 0.7\Delta\Phi_c$. This asymptotic error value depends strongly on the distance r to the target, and is reduced by roughly a factor 2 for each doubling of r. (The case $\Phi = 15^0,\ r = 20\lambda$ may be an exception because of the very small distance to the target). With element spacings $\Delta\Phi \approx \Delta\Phi_c/2$ the array clearly is 'superdirective', i.e. it employs fast-varying current components which radiate with extremely poor efficiency.

It is also noteworthy that extending the array arc has practically no effect on the asymptotic level of the error, presumably because the illumination eventually comes from the wrong directions. This is supported by Figure 37 which shows that for the 60° arc array the excitation is heavily tapered toward the ends.

On a normal far field RCS range with single element a measurement distance $r = 2d^2/\lambda$ is required to generate an approximately plane wave over the target diameter d, whereas on our circular near field range an angular element spacing $\Delta\Phi \approx \lambda/d$ is required, which to first order appears to be independent of r. However, the asymptotic error value for each array arc does depend on r, as Table 4 shows, and this relation remains to be explored.

Additional examples of target zone illuminations, some with constraints and achieved with various array geometries, are given in Appendix E.

Approved for public release; distribution is unlimited.

4.5.2 Array Excitation Perturbations due to Mutual Coupling

In the above computer model for the array illuminating the target region we used an ideal array excitation. In a physical array there is always mutual coupling between the elements, which will perturb the array excitation. However, as shown Appendix A, these effects can be compensated by a properly modified array excitation.

To demonstrate the magnitude of the mutual coupling perturbations, and thus the need of a coupling compensation, we compare a coupling perturbed array excitation with an ideal excitation and the resulting target illuminations.

From (54) the total current on the array is $\mathbf{i} = \mathbf{i}^i - \mathbf{i}^r$ or

$$\mathbf{i} = (\mathbf{I} - \mathbf{S})\mathbf{i}^i \tag{72}$$

and substituting for the scattering matrix $\mathbf{S}$ as expressed in (55) we find

$$\mathbf{i} = 2Z_0(\mathbf{Z}^a - Z_0\mathbf{I})^{-1}\mathbf{i}^i \tag{73}$$

where $\mathbf{i}^i$ denotes the incident ideal array excitation, $\mathbf{Z}^a$ the array mutual impedance matrix, and Z_0 the feed line impedance

For the impedance matched array with no coupling

$$Z^a_{mn} = \begin{cases} Z_0 & m = n \\ 0 & m \neq n \end{cases} \tag{74}$$

$$\mathbf{i} = \mathbf{i}^i$$

and for the impedance matched array with coupling where $Z^a_{mn} \neq 0$,

$$\mathbf{i} = 2\left(\frac{1}{Z_o}\mathbf{Z}^a - \mathbf{I}\right)^{-1}\mathbf{i}^i \tag{75}$$

As an example we consider the array case of Figure 36 above, with N=15 array elements, arc angle $\Phi = 30^0$, array radius $r = 40\lambda$, and compare the coupling-perturbed array excitation to the desired excitation in Figure 38a. The amplitude has decreased somewhat in the center of the array, but does not differ drastically in this particular case. However, the rms error of the illumination has increased from $\epsilon_{rms} = 0.07$ to $\epsilon_{rms} = 0.16$ and the relative error shown in Figure 38b has increased from a max. value $\epsilon_{rel} = 0.15$ to $\epsilon_{rel} = 0.37$. Coupling compensation of the array excitation therefore appears to be highly worthwhile.

4.5.3 The Array in the Receive Mode

In this section we consider the scattered field from the cylinder target illuminated by an arc array, as discussed above. (The relation between incident field E and induced voltage ν on the dipole, $\nu = (-2/k)E$, is derived in Appendix C).We sample the scattered near-field with our arc array, and again restrict the analysis to the plane of the array.

The signal received at each array element will be the sum of to the original scattered wave from the target and the perturbations from mutual coupling, i.e. scattering from neighboring array elements, and array-target coupling, i.e. multiple scattering between the array and the target, as discussed in Section 4.4. Therefore it will be of interest to compare the following array signals:

Approved for public release; distribution is unlimited.

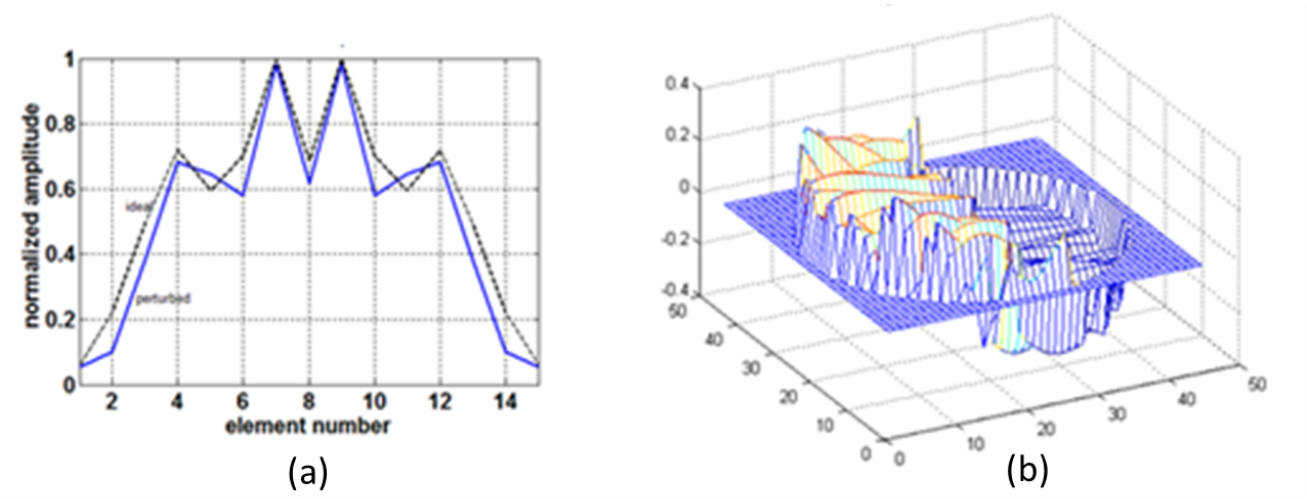

Figure 38: (a) Coupling-Perturbed Array Excitation (Full Line) and Ideal Array Excitation (Dashed Line) for an Array with N=15 Elements, Arc Angle $\Phi = 30^o$, Radius $r = 40\lambda$ (b) The Relative Illumination Error Over the 20λ Diameter Target Zone

- the received signals with the target present $\mathbf{v}^{a+t} = \mathbf{S}^{a+t}\mathbf{v}^i$ and with target absent $\mathbf{v}^a = \mathbf{S}^a\mathbf{v}^i$,
- the desired target signal $\mathbf{v}^t = \mathbf{Z}^t\mathbf{i}^i$, where $\mathbf{Z}^t$ represents the mutual impedances due to reflection in the cylinder,
- the geometrical optics signal $\mathbf{v}_{GO}$ corresponding to a plane wave reflected off the cylinder.

The mutual impedances $\mathbf{Z}^a_{nm}$ and $\mathbf{Z}^t_{nm}$ are derived in Appendices B and C. The GO signal is derived in Appendix D.

In our example we consider a target cylinder of radius $a = 10\lambda$, a receive array of radius $r = 40\lambda$, arc $\Phi = 60^o$ with $N = 29$ elements, and illuminate the cylinder with the same normalized excitation as shown in Figure 37.

The computed received signals $\mathbf{v}^{a+t}$ and $\mathbf{v}^a$ are shown in Figure 39 below. They are so close in value that they practically overlay in the graph. The reason is that the array mutual coupling strongly dominates, since the element spacing within the array only is about 1.3λ, whereas the distance to the cylinder is 30λ. The difference signal $\Delta\mathbf{v} = {}^{a+t} - \mathbf{v}^a$ is smaller by almost a factor 100, as shown in Figure 39b. To determine the target scattering, which only appears as a second order effect, thus requires high accuracy in the scattering matrices $\mathbf{S}^a$ and $\mathbf{S}^{a+t}$.

The desired target signal $\mathbf{v}^t = \mathbf{Z}^t\mathbf{i}^i$ is shown in Figure 40. It is of the same order of magnitude as the difference signal $\Delta\mathbf{v}$, and has a smooth angular variation as expected.

Finally we compare in Figure 41 the backscattered signal $\mathbf{v}^t$ obtained via the impedance matrix $\mathbf{Z}^t$ with the independently computed signal $\mathbf{v}_{GO}$ corresponding to plane wave scattering according to geometrical optics.

The array scattering represents 3-dim. scattering whereas the GO scattering model in Appendix D represents 2-dim. scattering, and therefore they are not strictly comparable. However, if we compare the angular dependence of the mutual impedance for the cylinder with an incident spherical wave, Appendix C,

Approved for public release; distribution is unlimited.

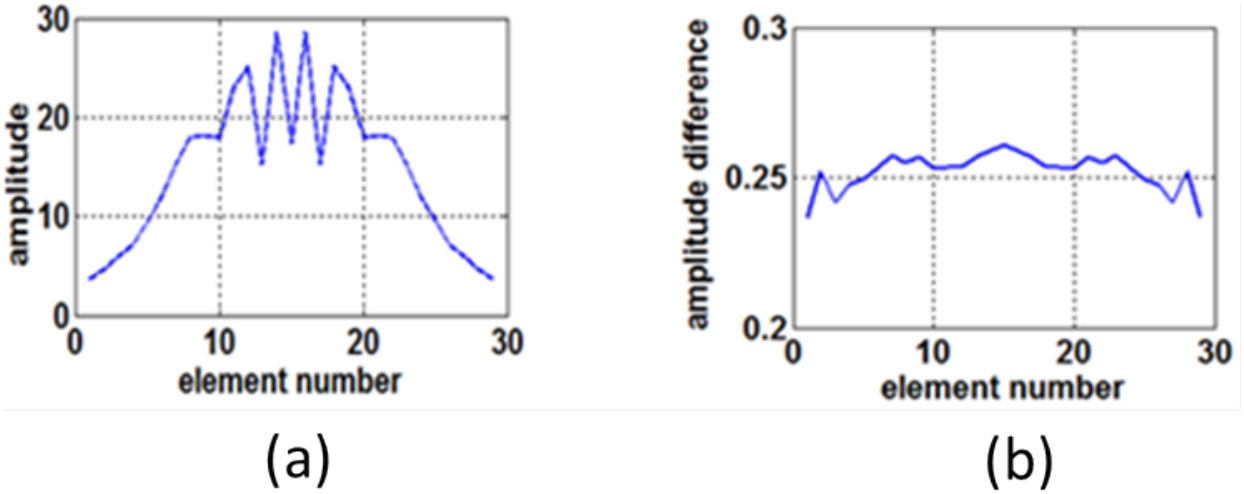

Figure 39: Scattering from a cylinder: (a) The Coupling-Perturbed Received Signal $\mathbf{v}^{a+t}$ with Target and the Received Signal $\mathbf{v}^{a}$ without Target – the Two Signals Practically Overlay (b) The Signal Difference Δv with and without Target

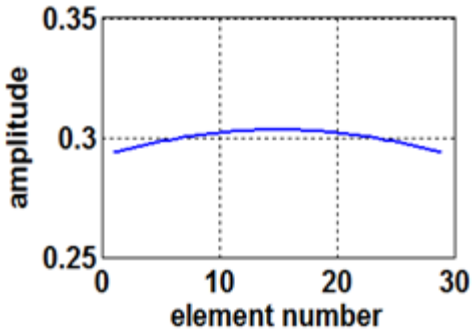

Figure 40: The Target Scattering Signal $\mathbf{v}^{t}$

Approved for public release; distribution is unlimited.

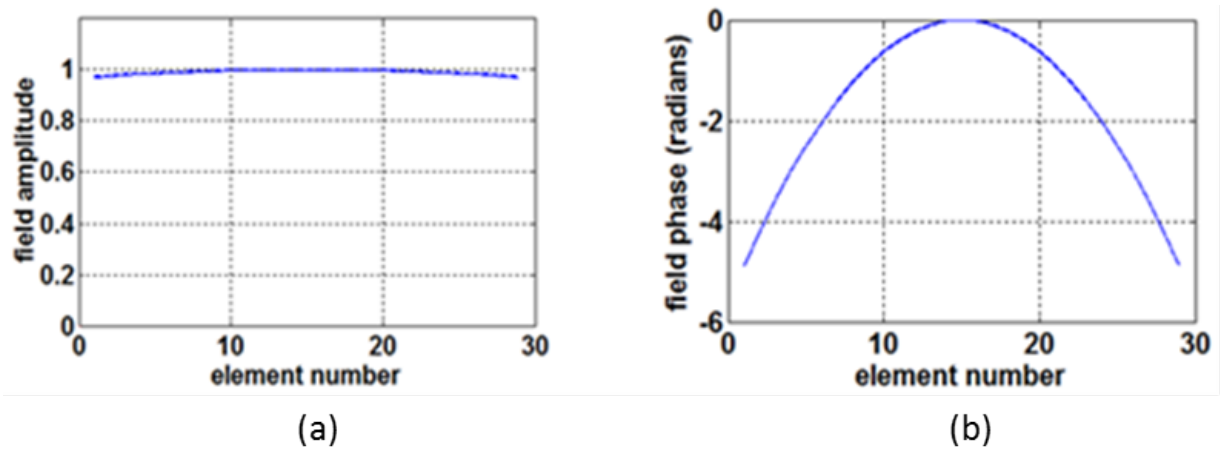

Figure 41: Comparison of the Scattered Field as Obtained by Array Measurement and the Scattered Field According to GO

and the angular dependence of the scattered field for an incident planar wave, Appendix D, we find that their ratio to be proportional to $\left[(2r" + a\cos\theta)/(r" + a\cos\theta)\right]^{1/2}$, i.e. it is practically constant for $r \gg a$. Therefore the scattered fields can be expected to be very close for the two cases, and this is confirmed in Figure 41a, where the two curves overlay. The amplitudes have been normalized to their maximum values, 0.303 and 0.378, respectively.

Also, we would expect the phases of the reflected fields to agree for the two cases, as is confirmed in Figure 41b, where once again the two curves overlay.

4.6 Conclusion

We have explored a novel scheme to use a circular arc array to simultaneously illuminate the RCS target and to measure the scattered near field. Assuming single-mode elements in the array, we analyzed the perturbations in the transmitted and in the received signals caused by the mutual coupling between the array elements and the array-target interaction, and developed techniques to correct these perturbations. The techniques are based on deriving the mutual impedance matrix from the measured scattering matrix of the array. In the receive mode our technique is related to the approach developed in [5], although our formulation differs somewhat from the active loading concept in [5].

As an example we considered an array of $\lambda/2$ dipoles and a RCS target in the form of a conducting infinite cylinder with 20λ diameter. For the transmit array we analyzed a set of different geometries and found that a certain minimum array-target distance is required in order to generated a reasonably plane incident wave. In this respect the arc array is different from a straight linear or planar array, which can generate a linear or planar phase front at very close range. However, a modest circular array can generate an approximately planar wave at a considerable closer distance than the normal far-field distance $2d^2/\lambda$. This could be a useful feature.

The example indicated that the array mutual coupling does significantly perturb the target illumination and therefore a corresponding correction is desirable. This can be affected by pre-multiplying the array excitation vector with the proper decoupling matrix.

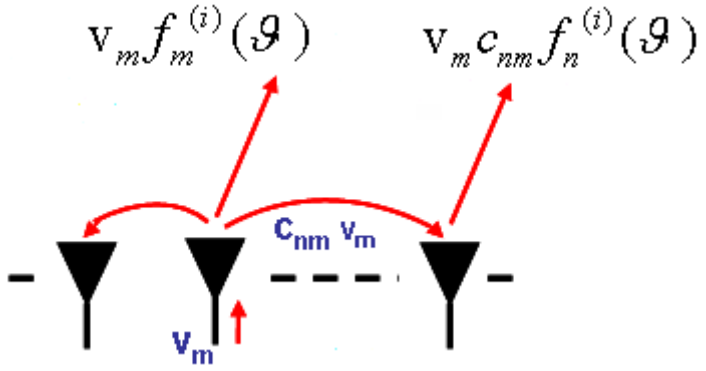

Figure 42: Direct and Parasitic Excitation Mechanisms Contributing to the Total Array Radiation

In the measurement mode (receive mode) our example showed that the array mutual coupling and the array-target interaction cause serious perturbations also in this mode. These can be corrected by measuring the scattering matrix $\mathbf{S}^a$ for the array in free space and the scattering matrix $\mathbf{S}^{a+t}$ for the array in the presence of the target, and computing the corresponding mutual impedance matrices $\mathbf{Z}^a$ and $\mathbf{Z}^{a+t}$ for the array. Finally, the desired unperturbed scattered field samples are obtained as $\mathbf{v}_d^r = (\mathbf{Z}^{a+t} - \mathbf{Z}^a)\mathbf{i}^i$, where $\mathbf{i}^i$ represents the input currents that generate the plane wave. Samples corrected in this fashion showed good agreement with independently computed samples using geometrical optics.

In the received signals the contributions from mutual coupling within the array strongly dominate over the desired target scattering and thus high measurement accuracy is required to correct for them.
Furthermore, our present analysis ignores higher order modes on the array elements and also the array feed and support structure. These should be considered in the future.

4.7 Appendix A: Mutual Coupling Compensation in Antenna Arrays

Consider an array of antenna elements as shown in Figure 42, and discussed in [34]. We excite only one element, m, but due to mutual coupling the other array elements will also be excited and contribute to the total radiation. Thus the array element pattern , i.e. the pattern of element m in the array environment, can be expressed as a superposition of all the individual element patterns , i.e. the patterns of each element in free space,

$$f_m(\theta) = \sum_n c_{nm} f_n^{(i)}(\theta) \tag{76}$$

The total field radiated by the array thus is

$$E(\theta) = \sum_m V_m f_m(\theta) = \sum_m \left[\sum_n c_{nm} f_n^{(i)}(\theta)\right] = \sum_n f_n^{(i)}(\theta) \left[\sum_m c_{nm} V_m\right] = (\mathbf{f}^{(i)})^t \mathbf{C}\,\mathbf{v} \tag{77}$$

where $\mathbf{f}^{(i)}$ and $\mathbf{v}$ are column vectors $f_n^{(i)}$ with and V_m as components, the coupling matrix $\mathbf{C}$ contains the coefficients c_{nm}, and t denotes transpose, and a factor e^{-jkr}/r has been suppressed. Thus if we feed the array with a 'transformed' excitation $\mathbf{v}' = \mathbf{C}^{-1}\mathbf{v}$ the array will radiate the 'decoupled' field $E = (\mathbf{f}^{(i)})^t\mathbf{v}$.

On receive, as illustrated in Figure 43, an incident field $E_o(\theta_i)$ at element m generates an output signal

$$v_m(\theta_i) = E_o f_m(\theta_i) = E_o \sum_n c_{mn} f_n^{(i)}(\theta_i) \tag{78}$$

Approved for public release; distribution is unlimited.

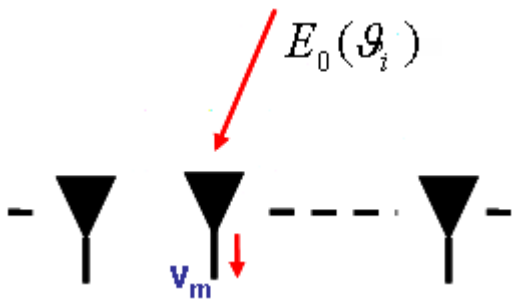

Figure 43: Illustrating the Receive Array

Letting the received element signals be the components of a column vector $\mathbf{v}(\theta_i)$ we obtain

$$\mathbf{v}(\theta_i) = E_0 \mathbf{C} \mathbf{f}^{(i)}(\theta_i) \tag{79}$$

Again, transforming v by the decoupling matrix $\mathbf{C}^{-1}$ we obtain

$$\mathbf{v}^{(i)}(\theta) = \mathbf{C}^{-1}\mathbf{v}(\theta_i) = E_0 \mathbf{f}^{(i)}(\theta_i) \tag{80}$$

which represents the desired ideal element signals in the absence of mutual coupling.

We note that

(1) this decoupling approach is independent of the direction of incidence and thus is valid for any spectrum of incident waves

(2) the approach applies to any array configuration, since we have not made any assumptions about the array shape, element spacings or orientation

(3) the same decoupling matrix applies for the transmit and receive mode, as a consequence of reciprocity

(4) the elements must be so called single mode elements. Otherwise the mutual coupling could excite a higher mode with a radiation pattern $\neq f^{(i)}(\theta)$, so that (76) would not apply.

(5) structural scattering, i.e. power which is scattered off a structural component and radiates with a pattern different from $f^{(i)}(\theta)$ can not be compensated, in analogy to (79).

(6) The coefficients s_{mn} in the scattering matrix $\mathbf{S}$ in (53) and the coefficients c_{mn} in the coupling matrix $\mathbf{C}$ in (76) are related, since our impedance matched dipoles are so called minimum-scattering antennas, which scatter and absorb equal amounts of power [15] [36]. The relation is $|s_{mn}|^2/Z_{load} = |c_{mn}|^2/Z_{free\ space}$, where Z_{load} denotes the dipole load and $Z_{free\ space}$ the free space impedance, and the element patterns are normalized so that $\int_{4\pi} f_n^{(i)}(\Omega) d\Omega = 1$.

Probably the simplest realization which satisfies these requirements is a waveguide array composed of single mode waveguide apertures in a ground plane. The ground plane must be large enough to avoid any edge diffraction, since this can not be included in the mutual coupling compensation. An array of dipoles would be another realization. However, again it is important that scattering off the support structure is negligible since it can not be compensated.

The key to the approach is the coupling matrix $\mathbf{C}$. For a real array probably the most practical technique to determine this matrix is by utilizing (79). Assuming that the individual element patterns $f_n^{(i)}$ are known we measure the received signal vector $\mathbf{v}(\theta_i)$ for a sufficiently large number of incidence angles and construct the linear system of equations (79) from which then $\mathbf{C}$ is solved. This approach was successfully demonstrated in [31].

Approved for public release; distribution is unlimited.

4.8 Appendix B: The Mutual Impedance Z^a_{nm} for Two Side-by-Side Dipoles

In our array model we use dipole elements with length $l = \lambda/2$ and an assumed current distribution [32, p. 151],

$$I(z) = I_o \sin k\left(\frac{l}{2} - |z|\right) \tag{81}$$

The radiation pattern in spherical coordinates has a single component

$$E_\theta = \frac{j\eta k}{2\pi} I_o \frac{e^{-jkr}}{r} \frac{\cos(\pi/2\cos\theta)}{\sin\theta} \tag{82}$$

and in our analyses we only consider the x, y-plane where the dipole field has only the z-component

$$E = E_z = -E_\theta(\pi/2) = -\frac{j\eta k}{2\pi} I_o \frac{e^{-jkr}}{kr} \tag{83}$$

The self and mutual impedances $Z^a = R^a + X^a$ were computed according to the following formulas given in [32, p. 417]:

$$\begin{aligned} R^a &= \frac{\eta}{4\pi}\left[2C_i(u_o) - C_i(u_i) - C_i(u_2)\right] \\ X^a &= -\frac{\eta}{4\pi}\left[2S_i(u_o) - S_i(u_i) - S_i(u_2)\right] \\ u_o &= kd \end{aligned} \tag{84}$$

$$\begin{aligned} u_1 &= k\left(\sqrt{d^2 + l^2} + l\right) \\ u_2 &= k\left(\sqrt{d^2 + l^2} - l\right) \end{aligned} \tag{85}$$

where d is the spacing between the dipoles, and C_i and S_i denote cosine and sine integrals. These expressions apply in a strict sense only for mutual impedances, i.e. spacings $d > 0$, but the self-impedance can be obtained by using a sufficiently small value for d.

4.9 Appendix C: The Mutual Impedance Z^t_{nm} due to Reflection in a Circular Cylinder

We will use the approximate expression (48) for the field E^t_{nm} and the mutual impedance Z^t_{nm}, where E^t_{nm} is the field at element n due to radiation from element m after reflection in the target cylinder. E^t_{nm} will be computed based on geometrical optics. This should be a fairly good approximation since the ray path is long in terms of wavelength.

For the electric field $E(s)$ at a point s along the ray we have [33]

$$E(s) = E(s_o)\sqrt{\frac{K(s)}{K(s_o)}} e^{-jk(s-s_o)} \tag{86}$$

where $E(s_0)$ is the complex field amplitude at an earlier point s_0, and $s - s_0$ is the path length along the ray. The amplitude variation is determined by the ray tube cross section, i.e. the gaussian curvature

$$K(s) = \frac{1}{\rho_1 \rho_2} \tag{87}$$

where ρ_1 and ρ_2 are the two principal radii of curvature of the wave front at s.

Approved for public release; distribution is unlimited.

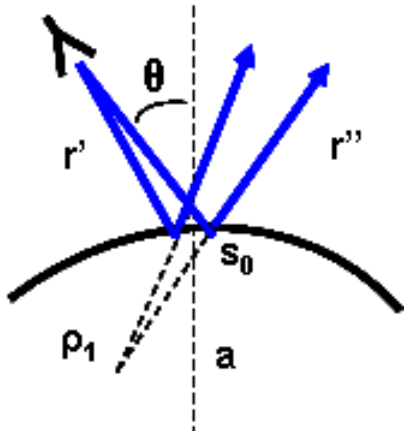

Figure 44: Reflection of Ray Tube at the Target Cylinder.

Our ray tube is reflected at s_0, see Figure 44. At the reflection point the ray tube cross section does not change, but the electric field experiences a sign change. Thus after reflection it is

$$E(s) = -E(s_0)\sqrt{\frac{K(s)}{K(s_0)}}e^{-jk(s-s_0)} = -E(s_0)\sqrt{\frac{\rho_1(s_0)\rho_2(s_0)}{\rho_1(s)\rho_2(s)}}e^{-jk(s-s_o)} \tag{88}$$

The element radiates a spherical wave so at the reflection point the incident ray has $\rho_1 = \rho_2 = r^{'}$, where $r^{'}$ denotes the distance from the element to the reflection point.

In the plane transverse to the cylinder the principal radius ρ after reflection is found with the aid of Figure 45. The ray tube cross section is equal immediately before and after the reflection, i.e.

$$dA_1 = dA_2. \tag{89}$$

and furthermore,

$$\begin{aligned} dA_1 &= r'\epsilon & (90)\\ dA_2 &= \rho(\epsilon + 2\delta) & (91)\\ a\delta\cos\theta &= dA_1 & (92) \end{aligned}$$

where ρ is the radius of curvature in a plane transverse to the cylinder, immediately after reflection, see Figure 45. This leads to

$$\rho = \frac{r^{'}a\cos(\theta)}{2r' + a\cos(\theta)} \tag{93}$$

Thus after reflection the two principal radii $\rho_1(r^{''})$, $\rho_2(r^{''})$ at a distance $r^{''}$ from s_0 , are

$$\begin{aligned} \rho_1(r^{''}) &= r^{''} + \rho\\ \rho_2(r^{''}) &= r^{''} + r^{'} \end{aligned} \tag{94}$$

where θ denotes the incidence angle at s_0, and a the cylinder radius. The radius ρ_2 is obtained from ρ_1 by letting a tend to infinity (the curvature is equal to zero in the plane tangent to the cylinder at s_0.). Thus

$$\frac{K(s)}{K(s_0)}) = \frac{\rho_1(s_0)\rho_2(s_0)}{\rho_1(s)\rho_2(s)} = \frac{\rho_1(r^{''}=0)\rho_2(r^{''}=0)}{\rho_1(r^{''})\rho_2(r^{''})} = \frac{\rho r^{'}}{(\rho + r^{''})(r' + r^{''})} \tag{95}$$

Approved for public release; distribution is unlimited.

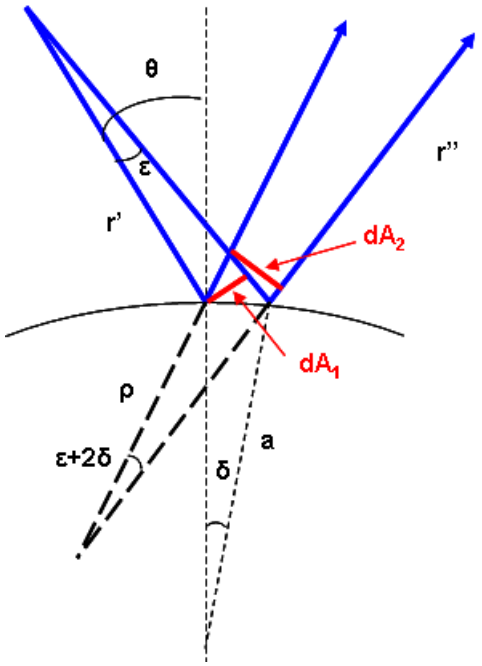

Figure 45: Illustrating the Derivation of the Curvature Radius ρ.

The incident field at s_0 is

$$E(s_0) = -\frac{j\eta k I}{2\pi} e^{-jkr'} kr' \tag{96}$$

and thus from (88)

$$E_n(r'') = \frac{j\eta k I_m}{2\pi} \frac{e^{-jkr'}}{r'} \sqrt{\frac{\rho r'}{(\rho + r'')(r' + r'')}} e^{-jkr''} \tag{97}$$

where $\rho = \rho_{nm},\ r' = r'_{nm},\ r'' = r''_{nm},\ \theta = \theta_{nm}$. From (48) we obtain

$$V_{nm} = E_{nm} \left[\frac{-1}{I_n} \int_{-l/2}^{l/2} I_n(z) dz \right] = E_{nm} \left(-\frac{2}{k} \right) \tag{98}$$

where we have carried out the integration in the square bracket, using the current distribution given in (81). Finally, the desired mutual impedance for the cylinder target

$$Z^t_{nm} = \frac{V_{nm}}{I_m} = -\frac{j\eta}{\pi k r'} \sqrt{\frac{\rho r'}{(\rho + r'')(r' + r'')}} e^{jk(r' + r'')} \tag{99}$$

The incidence angle θ in (93) is found to be

$$\theta_{nm} = \text{arctg} \frac{r \sin \varphi_{nm}}{r \cos \varphi_{nm} - a} \tag{100}$$

where r denotes the array radius and φ_{nm} the half-angle between elements m and n, as shown in Figure 46, and $r'_{nm} = r''_n m = [a^2 + r^2 - 2ar \cos \varphi_{nm}]^{1/2}$.

4.10 Appendix D: GO Reflection in a Circular Cylinder

Approved for public release; distribution is unlimited.

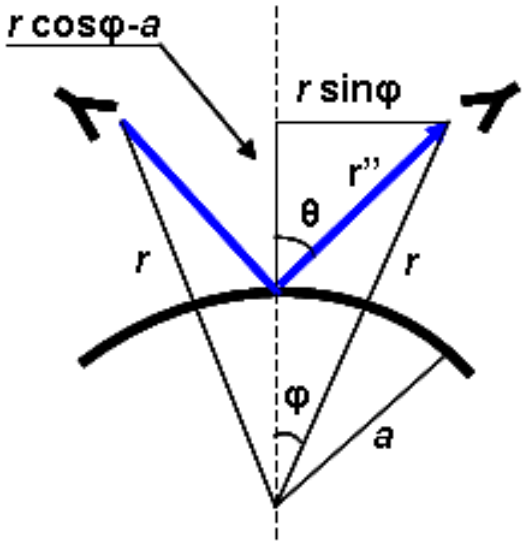

Figure 46: Illustrating the Derivation of the Incidence Angle θ

We consider a plane wave incident on a circular cylinder and derive the scattered E-field. First we derive the incidence angle θ for a ray reflected to a given probe location (r, ϕ), where r denotes the radius to the field point and ϕ the angle between r and the plane wave direction, as illustrated in Figure 47. As seen in the figure, there are two right angle triangles, one with the hypotenuse a and another with the hypotenuse r, which have one side in common. This leads to the transcendental equation

$$a \sin\theta = r \sin(2\theta - \phi) \tag{101}$$

for θ. An approximate solution θ can be obtained by assuming $\theta \ll 1, 2(\theta - \phi) < 1$, and doing a series expansion, which yields

$$\theta = \theta_0 = \frac{1}{2 - a/r}\phi \tag{102}$$

Setting

$$\theta = \theta_0 + \epsilon \tag{103}$$

in (101) and performing a new series expansion for $\epsilon \ll 1$ leads to

$$\epsilon = \frac{r \sin(2\theta_0 - \phi) - a \sin\theta}{-2r \cos(2\theta_0 - \phi) + a \cos\theta_0} \tag{104}$$

Thus our approximate solution is

$$\theta \approx \frac{1}{2 - a/r}\phi + \epsilon \tag{105}$$

where ϵ is given by (104). With this solution the difference between the left and the right side of (101) is <0.003 for $0 < \phi/2\pi$ and $r = 2a$. For larger r the approximation gets better.

For the electric field $E(s)$ at a point s along the ray we have as in Appendix C, (88)

$$E(s) = -E(s_0)\sqrt{\frac{\rho_1(s_0)\rho_2(s_0)}{\rho_1(s)\rho_2(s)}}e^{-jk(s-s_0)} = -E(s_0)\sqrt{\frac{\rho r'}{(\rho + r'')(r' + r'')}}e^{-jkr''} \tag{106}$$

where $E(s_0)$ is the complex field amplitude incident at the reflection point s_0, and r'' the path length along the ray from s_0.

Approved for public release; distribution is unlimited.

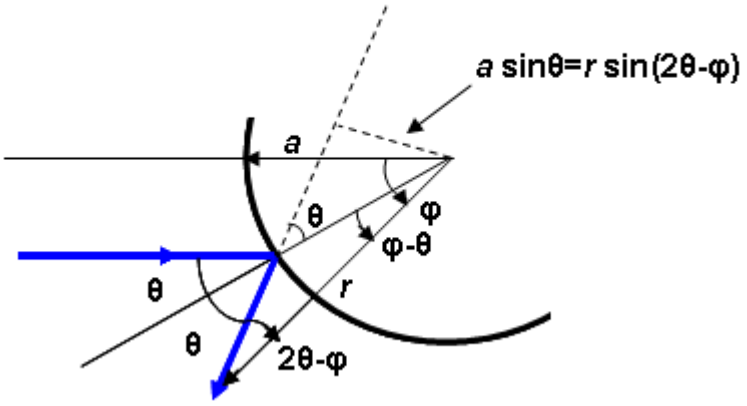

Figure 47: Illustrating the Incidence Angle θ Which Corresponds to a Ray Reflected to a Given Point (r, φ).

Letting $r' \to \infty$ in (93) we obtain

$$\rho = \frac{a\cos\theta}{2} \tag{107}$$

and the scattered E-field

$$E(s) = -E_0\sqrt{\frac{a\cos\theta}{2'' + a\cos\theta}}e^{-jk(r''-s_0)} \tag{108}$$

where

$$\begin{aligned} E_0 &= \text{the amplitude of the incident plane wave,} \\ s_o &= a\cos\theta, \text{if we reference the phase to the cylinder center,} \\ r'' &= \sqrt{a^2 + r^2 - 2ar\cos(\phi - \theta)} \end{aligned} \tag{109}$$

and θ is given by (104) and (105) above.

4.11 Appendix E: Analysis of a Tentative Bistatic Near-Field RCS Measurement Geometry

In the main text of this section we synthesized a plane wave over a target zone without restricting its behavior outside this zone. In near-field bistatic applications, the probe needs to be positioned outside the target zone to collect the scattered field. Thus, it is desirable that the plane-wave generator provides a minimum power level outside the target zone where the probe is located; ideally the power level would be uniform within the target zone and zero outside. Although this situation is not physically possible, it is of interest to explore to what extent it can be approximated.

In this appendix, therefore, we analyze a similar measurement set-up as in the main text– an array, which illuminates a circular target zone – but now the measurement probe is assumed separate from the array and it scans the scattered field over all azimuth angles. The array and the probe are located on the same circle of radius r, and the target zone has radius a, cf. Figure 48. Presumably it is not feasible to achieve much reduced power levels over all azimuth angles and, therefore, we will try to reduce the power level only over two symmetric sectors, one of which is shown as a 'null sector' of angular width $3\pi/4 - \Phi/2 - \delta$ in Figure 48. The angle δ represents a minimum distance to the array edge element, where the power level goes to infinity. In the computations to follow we choose $r = 7.5m$, $a = 1.8m$, $\delta = \pi/20$, and we explore the frequency band 0.5 – 10 GHz.

Approved for public release; distribution is unlimited.

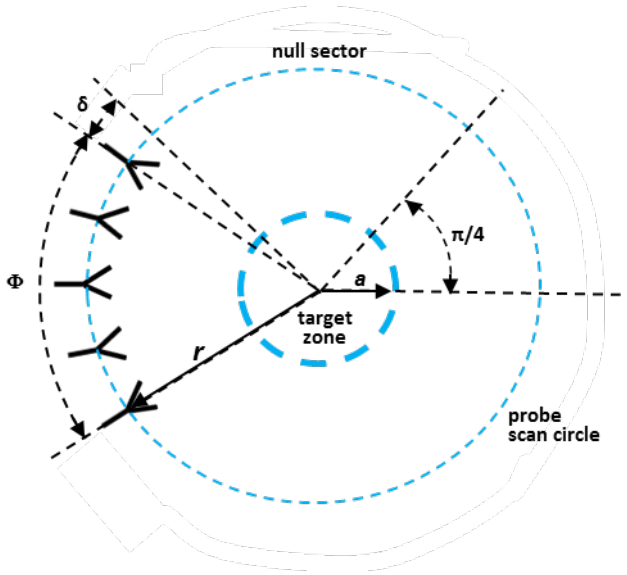

Figure 48: Near-Field Bistatic RCS Measurement Setup with $r = 7.5m$ and $a = 1.8m$

The array synthesis procedure outlined in Section 4.4 easily includes the requirement for a reduced power level in the null sector. This is done by extending the set of M desired plane wave values E_{dm} over the target zone with an additional set of N_{null} desired field values $E_{dm} = 0$ over the null sector, which results in a similar equation system as (40), but now with $M + N_{null}$ equations. As an additional feature we include a weighting function $\mathbf{W}$ such that we can control the trade-off between satisfying the plane wave requirement of the target zone and the low level requirement of the null sector. This leads to the equation system

$$\mathbf{W}\mathbf{E}_d = \mathbf{W}\,\mathbf{R}\,\mathbf{A} \tag{110}$$

where

(-) $\mathbf{E}_d = (E_{d,1},\ \ldots\ , E_{d,M+N_{null}})$ is a column vector, which represents the desired field values over the target zone and the null sector. The first M components E_{dm} have uniform amplitudes E_0 and phases corresponding to a plane wave illumination over the target zone. The last N_{null} components $E_{dm} = 0$, corresponding to the desired field values over the null sector.

(-) $\mathbf{A} = (A_1,\ \ldots,\ A_N)$ is a column vector, which represents the array element excitation,

(-) $\mathbf{R}$ is a $(M + N_{null}) \times N$ matrix with coefficients $e^{-jkr_{mn}}/kr_{mn}$, which represent the relation between the array excitation A_n and the E-field at point m, with k and r_{mn} denoting the wave number and distance, respectively.

(-) $\mathbf{W}$ is a diagonal $(M + N_{null}) \times (M + N_{null})$ matrix with coefficients w_{ii}. When $M + N_{null} = N$ an exact solution for the excitation $\{A_n\}$ can be obtained and the matrix $\mathbf{W}$ has no effect. When $M + N_{null} > N$ the matrix $\mathbf{W}$ assigns the relative weight w_{ii} to each equation, when the $\{A_n\}$ are solved from the overdetermined system of equations (110) in a LMS sense.

The realized field generated by $\mathbf{A}$ is

$$\mathbf{E} = \mathbf{R}\,\mathbf{A} \tag{111}$$

Approved for public release; distribution is unlimited.

Table 5: Results at f = 0.5 GHz for Three Arrays of Arcs Φ of 15°, 30°, and 60°, with N=2, N=3 and N=6 Elements, Respectively.

	Φ=15°, N=2			Φ=30°, N=3			Φ=60°, N=6		
	w=0	w=1	w=10	w=0	w=1	w=10	w=0	w=1	w=10
A_{max}	25	7.4	0.11	36	21	0.78	28	20	0.69
ε_{rel}	1.2	1.1	1.0	1.5	1.1	1.0	1.1	1.1	1.0
ε_{rms}	0.70	0.86	1.0	0.52	0.67	0.99	0.55	0.61	0.98
$\varepsilon_{null,rel}$	3.7	1.1	0.016	3.0	1.2	0.028	0.98	0.76	0.028
$\varepsilon_{null,rms}$	1.3	0.37	0.005	1.1	0.44	0.014	0.72	0.48	0.016

We will use the following three different weight alternatives:

$$w_{ii} = \begin{cases} 1 & i = 1,\ ...,\ M \\ 0 & i = M+1,\ ...,\ M+N_{null} \end{cases},$$

which imposes zero field suppression on the null sector;

$$w_{ii} = \begin{cases} 1 & i = 1,\ ...,\ M \\ 1 & i = M+1,\ ...,\ M+N_{null} \end{cases},$$

which gives equal weight to the desired field in the target zone and the null sector; and

$$w_{ii} = \begin{cases} 1 & i = 1,\ ...,\ M \\ 10 & i = M+1,\ ...,\ M+N_{null} \end{cases},$$

which gives 10 times more weight to the desired field over the null sector than in the target zone. In all cases the number M is determined by sampling the target zone with $\lambda/2$ spacing, and the number N_{null} is similarly determined by sampling the null sector with $\lambda/2$ spacing.

We analyze the measurement set-up shown in Figure 48 for three different array configurations, i.e. array arcs Φ of 15°, 30°, and 60°, at the frequencies 0.5 GHz, 2.0 GHz and 10.0 GHz. The number of array elements N is determined by (39) for each case. The results are shown in the Tables 5 through 7 below, where

- w denotes the weight over the null sector (over the target zone the weight =1 in all cases)
- A_{max} denotes the maximum array coefficient
- ϵ_{rel} denotes the resultant maximum relative amplitude over the target zone
- ϵ_{rms} denotes the rms error over the target zone,
- $\epsilon_{null,rel}$ denotes the max amplitude error over the null sector, normalized to the desired target field amplitude E_0, and
- $\epsilon_{null,rms}$ denotes the rms error over the null sector, normalized to E_0.

We note that with increasing weight over the null sector the rms errors decrease over this sector, while they increase over the target zone, as expected. Similarly, for fixed frequency and weight, these errors decrease with increasing elements numbers. For the relative errors this decrease is not consistent, since more elements allow for faster local pattern ripple.

Approved for public release; distribution is unlimited.

Table 6: Results at f = 2.0 GHz for Three Arrays of Arcs Φ of 15°, 30°, and 60°, with N=6, N=12 and N=24 Elements, Respectively.

	Φ=15°, N=6			Φ=30°, N=12			Φ=60°, N=24		
	w=0	w=1	w=10	w=0	w=1	w=10	w=0	w=1	w=10
A_{max}	17	17	1.8	17	14	1.1	17	15	1.9
ε_{rel}	1.6	1.4	1.0	0.95	0.98	1.0	0.94	0.94	1.0
ε_{rms}	0.51	0.54	0.95	0.28	0.41	0.96	0.24	0.28	0.92
$\varepsilon_{null,rel}$	2.7	1.5	0.11	3.9	2.1	0.078	1.8	1.4	0.14
$\varepsilon_{null,rms}$	0.85	0.61	0.048	1.4	0.86	0.044	0.90	0.73	0.065

Table 7: Results at f = 10.0 GHz for Three Arrays of Arcs Φ of 15°, 30°, and 60°, with N=30, N=60 and N=120 Elements, Respectively.

	Φ=15°, N=30			Φ=30°, N=60			Φ=60°, N=120		
	w=0	w=1	w=10	w=0	w=1	w=10	w=0	w=1	w=10
A_{max}	6.8	6.7	1.3	7.0	6.8	3.0	7.0	6.8	2.7
ε_{rel}	1.4	1.3	1.1	1.2	1.2	1.1	1.2	1.2	1.1
ε_{rms}	0.57	0.58	0.93	0.17	0.19	0.77	0.16	0.16	0.70
$\varepsilon_{null,rel}$	4.8	3.5	0.23	3.2	2.6	0.44	1.7	1.6	0.38
$\varepsilon_{null,rms}$	1.5	1.2	0.12	1.2	1.0	0.20	0.88	0.84	0.23

Approved for public release; distribution is unlimited.

Unfortunately, these results show that acceptable illumination levels are not easily obtained simultaneously in the target zone and the null sector. The only cases where the rms illumination over the null sector is below the desired -20 dB is with weight values $w = 10$ where, however, the target zone rms illumination error is approximately 1.

An example of the field error vs. weighting over the target zone and null sector is shown in Figure 49. It corresponds to the case in Table 6, right column, $\Phi = 60^o$arc array with $N = 24$ elements. We note that in the target zone all the large errors are located at the edge. This suggests that one possible design approach would be to over-dimension the target zone and then use a slightly reduced zone for the actual measurements. A general feature appears to be that the illumination is not concentrated to a single narrow beam, as seen also earlier in Figures 36 and 37. Thus, not only is it difficult to suppress the illumination over the null sector, but the whole measurement range will be illuminated over a very wide sector, which may lead to disturbing stray radiation. This problem needs further attention.

The number N of array elements was determined from (39) which represents an upper limit to avoid highly reactive array excitations. However, this limit applies strictly only for the synthesis of circular array excitations. With the inclusion of additional constraints in the synthesis problem, such as the radiation suppression over the null sector, presumably the number N can be increased without leading to reactive arrays. This is because additional degrees of freedom, as represented by the increased number of elements, will be devoted to satisfying the additional constraints rather than the target illumination. Therefore, we have run the cases in Tables 5 through 7 also with double the number of elements N. However, the improvement in the results was not significant.

Approved for public release; distribution is unlimited.

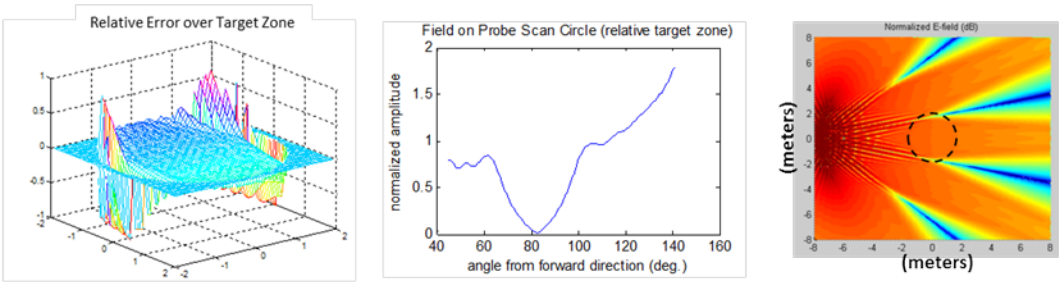

$w = 0$

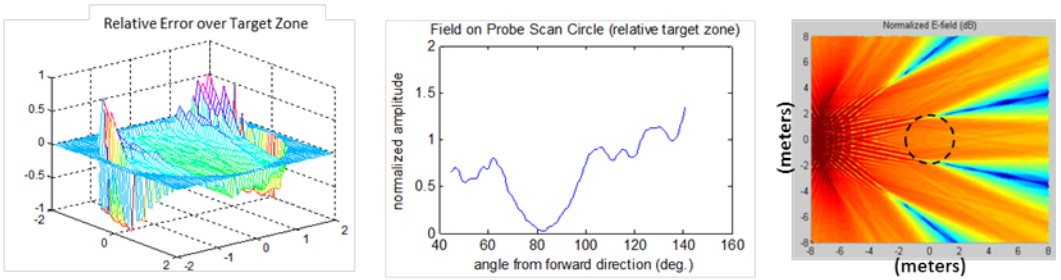

$w = 1$

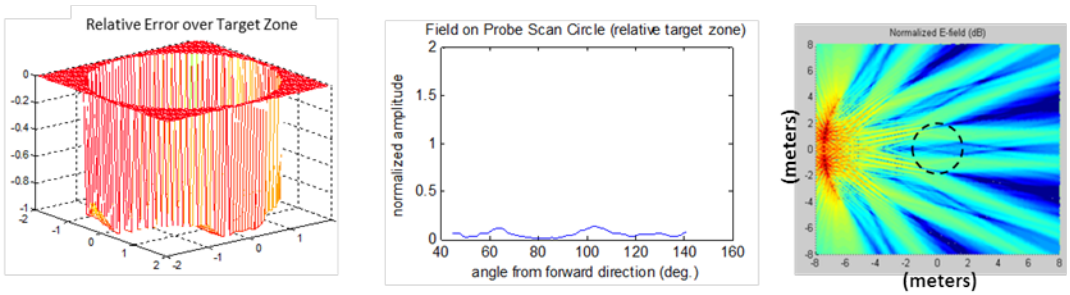

(a) (b) (c)

$w = 10$

Figure 49: Illumination Error Resulting from Different Weighting of the Target Zone Vs. the Null Sector: a) Relative Error Over Target Zone, b) Error Over Null Sector, c) Radiation Intensity in the Plane of the Array and the Target Zone

Approved for public release; distribution is unlimited.

5 References

[1] A. D. Yaghjian, "An Overview of near-field antenna measurements," *IEEE Trans Antennas Prop*, Vol. 34, No. 12, 435-445, July, 1986.

[2] J.E. Hansen, Ed. *Spherical Near-field Antenna Measurements*, Peter Peregrinus, London, 1988.

[3] R.A. Marr, U.H.W. Lammers, T.B. Hansen, T.J. Tanigawa, and R.V. McGahan, "Bistatic RCS calculations from cylindrical near-field measurements–Part II: Experiments," *IEEE Trans Antenna Prop*, Vol. 54, No. 12, 3857-3864, Dec, 2006.

[4] B.J. Cown and C.E. Ryan, Jr., "Near-field scattering measurements for determining complex target RCS," *IEEE Trans Antenna Prop*, Vol. 37, No. 5, 576-585, May, 1989.

[5] J.K. Schindler, "An Approach to Minimizing Probe Array/Target Interactions for Near-Field Scattering Measurements", AFRL Technical Report, AFRL-RY-HS-TR-2011-00781, 13 May, 2011.

[6] J. Estrada, SATIMO, USA, Inc., Private Communication, February, 2011.

[7] R.F. Harrington, "Theory of Loaded Scatterers," Proceedings of IEEE, Vol 111, No. 4 April, 1964.

[8] B.A. Kramer and K.T. Kim, "Design of Low-Backscatter Open-End Waveguides and Dipole Arrays," Unpublished Technical Report, 2012.

[9] B. Peterson and S. Strom, "T Matrix for Electromagnetic Scattering from an Arbitrary Number of Scatterers and Representation of E(3), " *Physical Review D*, Vol. 8, No, 10, 3661-3678, 1973.

[10] M. Lax, "Multiple scattering of waves," *Rev. Modern Phys.*, Vol. 23, pp. 287-310, 1951.

[11] P.C. Waterman, "Symmetry, unitarity and geometry in electromagnetic scattering," *Phys. Rev. D.*, Vol. 3, No., 4, pp. 825-849, 1971.

[12] K.T. Kim and B.A. Kramer, "Direct determination of the T matrix from an impedance matrix computed with the Rao-Wilton-Glisson basis function," *IEEE Trans Antennas Prop*, Vol. 61, No. 19, 5324-5327, October, 2013.

[13] S.M. Rao, D. R. Wilton, and A. W. Glisson, "Electromagnetic scattering by surfaces of arbitrary shape," *IEEE Trans Antennas Prop*, Vol. 30, No. 3, 409-418, May, 1982.

[14] K.T. Kim, "Direct determination of the T matrix from an impedance matrix computed with the thin-wire reduced-kernel and the roof-top basis function," Unpublished notes, 2011.

[15] R.H. Dicke, C.G. Montgomery and E.M. Purcell, *Principles of microwave circuits,* Dover Publication, New York, 1965.

[16] J. B. Andersen and A. Frandsen, "Absorption Efficiency of Antennas," *IEEE Transactions on Antennas and Propagation*, AP- 53, 9, pp. 2843-2849, September, 2005.

[17] H. Steyskal, "On the Power Absorbed and Scattered by an Antenna," *IEEE Antennas and Propagation Magazine*, pp. 41-45, Vol. 52, No.6, December 2010

[18] J.C. Bolomey, F.E. Gardiol, *Engineering Applications of the Modulated Scatterer Technique,* Artech House, Boston, MA, 2001.

[19] A. D. Yaghjian, "Near-field antenna measurements on a cylindrical surface: A source scattering-matrix formulation," Nat. Bur. Stds, *Tech Notes*, 696, Boulder, CO, 1977.

[20] K.T. Kim, "The T matrix of a loaded dipole," Unpublished technical notes.

[21] G.J. Burke, "Numerical Electromagnetic Code: NEC-4," Lawrence Livermore National Laboratory, Livermore, CA, 1992.

[22] K.T. Kim, "Theory of Near-Field Scanning Using a Probe Array," Laboratory Research Initial Request (LRIR) Proposal, 2011.

[23] K.T. Kim, "The translation formula for vector multipole fields and the recurrence relations of the translation coefficients of scalar and vector multipole fields," *IEEE Trans. Antennas Prop.,* Vol. 44, No. 11, pp. 1482-1487, 1996.

[24] K.T. Kim, "Efficient recursive generation of the scalar spherical multipole translation matrix," *IEEE Trans. Antennas Prop.*, Vol. 55, No. 12, pp. 3484-3494, 2007.

[25] K.T. Kim, "Symmetry relations of the translation coefficients of the scalar and vector spherical vector multipole fields," *Progress in Electromagnetic Research*, Vol. 48, Chapter 3, pp. 45-66, 2004.

[26] K.T. Kim, "A memory-reduction scheme for the FFT T-matrix method," *IEEE Antenna Wireless Propag. Lett.* Vol. 3, No 10, pp-193-196, 2004.

[27] K.T. Kim, "Comparison and improvement of the computational efficiencies of two FFT-based iterative solution methods for scalar multiple scattering equation," *Communications in Computational Physics*, Vol. 5, No. 1, pp. 108-125, January, 2009.

[28] J. Rubio, M.A. Gonzalez, and J, Zapata, "Generalized-scattering matrix analysis of a class of finite arrays of coupled antennas by using 3-D FEM and spherical mode expansion," *IEEE Trans. Antennas Prop.,* Vol. 53, No. 3, pp. 1133-1144, 2005.

[29] Schindler, John K., "Probe Array Correction with Strong Target Interaction," AFRL Technical Report AFRL-RY-WP-TR-2012-0257, August 2012.

[30] O. Bucci, G. Franceschetti, G. Mazzarella, G. Panariello, "Intersection Approach to Array Pattern Synthesis," *IEEE Proc.* Vol. 137, Pt. H, No. 6, Dec. 1990.

[31] L. Pettersson, M. Danestig, U. Sjostrom, "An Experimental Digital Beamforming", *Proc. IEEE Inernational Symp. on Phased Array Systems and Technology*, Boston, MA, Oct. 1996.

[32] C. Balanis, *Antenna Theory.* 2nd Ed., John Wiley & Sons, Inc., NY 1997.

[33] S. Holt, "Wave Fronts, Rays, and Focal Surfaces," in R. Collin, F. Zucker (ed.): *Antenna Theory*, Pt. 2, McGraw-Hill Inc., 1969

[34] H. Steyskal, J. Herd, " Mutual Coupling Compensation in Small Array Antennas." *IEEE Trans. AP*, Dec. 1990.

[35] L. Josefsson, P. Persson, *Conformal Array Antenna Theory and Design*, IEEE Press 2006.

[36] R. Collin: The Receiving Antenna, in R. Collin, F. Zucker (ed): *Antenna Theory*, Pt.1, McGraw-Hill Inc., 1969

List of Acronyms, Abbreviations, and Symbols

ACRONYM	DESCRIPTION
AFRL	Air Force Research Laboratory
DUT	device under test
FF	far field
GO	geometrical optics
LMS	least mean square
MC	mutual coupling
MS	multiple scattering
MS	modulated scattering
NEC	Numerical Electromagnetic Code
NF	near field
RAM	radar absorbing material
RCS	radar cross section
RMS	root mean square
SNR	signal to noise ratio
TM	translation matrix
TSM	total scattering matrix
TVSMF	transverse vector spherical multipole field
λ	wavelength

Approved for public release; distribution is unlimited.